# CRASHWORTHINESS ANALYSIS OF A COMPOSITE LIGHT FIXED-WING AIRCRAFT INCLUDING OCCUPANTS USING NUMERICAL MODELLING

**WADE ROBERT EVANS**

SUBMITTED IN FULFILMENT OF THE REQUIREMENTS OF THE DEGREE OF DOCTOR OF ENGINEERING: MECHANICAL IN THE FACULTY OF ENGINEERING, SCIENCE AND THE BUILT ENVIRONMENT AT THE DURBAN UNIVERSITY OF TECHNOLOGY

[redacted]

SUPERVISOR
PROFESSOR DAVID JONSON

28/10/16
DATE

[redacted]

CO-SUPERVISOR
PROFESSOR MARK WALKER

30/10/16
DATE

DURBAN, SOUTH AFRICA
OCTOBER 2016

## DECLARATION

I declare that this thesis is my own unaided work except where due acknowledgement is made to others. This thesis is being submitted for the Degree of Doctor of Engineering to the Durban University of Technology and has not been previously submitted for any other degree or examination.

Wade Robert Evans

22/10/2016

Date

## ACKNOWLEDGEMENTS

I wish to thank the Durban University of Technology and ARMSCOR for providing financial assistance to conduct this research. I would like to give special thanks to Professor David Jonson and Professor Mark Walker for the opportunity to undertake this research project, for the encouragement to achieve my objectives, and for their wisdom and guidance without which this thesis would not have been possible. I would like to thank Douglas Marriott (technical consultant for MSC Software) for his much valued assistance and finally, I would like to thank my parents, friends, and especially Jamie-Lee Fisher for their encouragement and support.

## ABSTRACT

The development and validation of reliable numerical modelling approaches is important for higher levels of aircraft crashworthiness performance to meet the increasing demand for occupant safety. With the use of finite element analysis (FEA), development costs and certification tests may be reduced, whilst satisfying aircraft safety requirements. The primary aim of this study was the development and implementation of an explicit nonlinear dynamic finite element based methodology for investigating the crashworthiness of a small lightweight fibre reinforced composite aircraft with occupants. The aircraft was analysed as it crashed into soft soil and the FEA software MSC Dytran was selected for this purpose. The aircraft considered for the purposes of this study was based on a typical four-seater single engine fibre-reinforced plastic composite aircraft.

The definition of a survivable accident is given by Coltman [1] as: “an accident in which the forces transmitted to the occupant through his seat and restraint system do not exceed the limits of human tolerance to abrupt accelerations and in which the structure in the occupant’s immediate environment remains substantially intact to the extent that a liveable volume is provided for the occupants throughout the crash sequence”. From this definition, it was determined that the FEA models must primarily provide an assessment on the crashworthiness of the aircraft in terms of the structural integrity of the airframe to ensure a minimum safe occupant volume and the tolerance of humans to abrupt (de)accelerations. An assessment of other crashworthiness factors have been ignored in this study, such as post-crash hazards (e.g. fire) and safe egress for the occupants.

Stockwell [2] performed a dynamic crash analysis of an all-composite Lear Fan aircraft impacting into concrete with the explicit nonlinear dynamic finite element code MSC Dytran. The structural response of components was

qualitatively verified by comparison to experimental data such as video and still camera images. The composite fuselage materials were represented with the use of simplified isotropic elastic-plastic material models, and therefore did not account for the anisotropic properties of composite materials and the associated failure mechanisms. The occupants were represented as lumped masses; therefore occupant response could not be investigated.

Malis and Splichal [3] performed a dynamic crash analysis of a composite glider impacting into a rigid surface with MSC Dytran; however further model verification was required. The 50$^{th}$ percentile adult male (occupant of average height and mass) Hybrid III anthropomorphic test device (ATD), also referred to as a crash test dummy, was represented in the analyses with the Articulated Total Body (ATB) model integrated within MSC Dytran. Various injury criteria of the ATB model were evaluated to determine the crashworthiness of the glider.

Bossak and Kaczkowski [4] performed global dynamic crash analyses of a composite light aircraft crash landing. Representative wet soil, concrete and rigid impact terrains were modelled using Lagrangian-based finite element techniques and only the vertical velocity component of the aircraft was considered to simplify analyses. It was assumed that the previous use of only a downward vertical velocity component was a result of possible numerical instabilities which commonly occur with the use of Lagrangian solvers when considering problems with large deformations, which is a characteristic of crash analyses (i.e. the addition of a horizontal velocity component may result in severe element deformation of the soft soil terrain, resulting in premature analysis termination). Analyses of the occupant were performed in separate local models, using accelerations derived from the global analyses results. The real-time interactions between the occupant and aircraft therefore could not be investigated, which is considered a major disadvantage.

Impact analyses of helicopters into water were performed by Clarke and Shen [5], and Wittlin et al. [6]. Both these papers showed promising results with the use of Eulerian-based finite element techniques to model the water. Additionally, combined horizontal and forward velocity components were assigned to the fuselages with success. It must be noted that the fuselages were modelled as rigid bodies; therefore the effect of structural failure on analyses could not be investigated. Fasanella et al. [7] performed drop tests of a composite energy absorbing fuselage section into water using Eulerian, Arbitrary Lagrange Eulerian (ALE) and Smooth Particle Hydrodynamics (SPH) meshless Lagrangian-based finite element techniques to represent water. Successful correlation between experimental and numerical data was achieved; however, structural failure could not be modelled with the Eulerian-based finite element technique due to analysis code limitations at the time.

A “building block” approach was used in this study to develop accurate numerical modelling techniques prior to the implementation of the full-scale crash analyses. Once the blocks produced satisfactory results in themselves, they were then integrated in order to achieve the abovementioned primary aim of this study. The sub-components (or blocks) were the occupant (viz, FEA of the human bodies’ response to impact), (FEA of) soft soil impact and (FEA of) fibre-reinforced plastic composite structures. This approach is intuitive and provides key understanding of how each sub-component contributes to the full-scale crash analyses. Published literature was reviewed, where possible, as a basis for the development and validation of the techniques employed for each sub-component.

The technique required to examine the dynamic response of an occupant with MSC Dytran, integrated with the ATB model, was demonstrated through the analysis of a sled test. The numerical results were found to be comparable to experimental results found in the literature. An Eulerian-based finite element technique was implemented for soft soil impact analyses, and its effectiveness was determined through correlation of experimental

penetrometer drop test results found in the literature. An investigation into the performance of the Tsai-Wu failure criterion to capture the onset and progression of failure through the layers of fibre reinforced composite laminates was conducted for an impulsively loaded unidirectional laminate strip model. Based on the results obtained, the techniques implemented for each sub-component were deemed valid for crashworthiness applications (viz. to achieve the project aim).

Full-scale crash analyses of impacts into rigid and soft soil terrains with varying aircraft impact and pitch angles were investigated. Typical limitations encountered in previously published works were overcome with the techniques presented in this study. The aircrafts' laminate layup schedule was explicitly defined in MSC Dytran, thereby eliminating the inherent inaccuracies of using isotropic models to approximate laminated composite materials. The aircraft was assigned both horizontal and vertical velocity components instead of only a vertical component, which increased the model accuracy. Numerical instabilities, due to element distortion of the terrain when using a Lagrangian approach, were eliminated with the use of an Eulerian soft soil model (Eulerian techniques are typically used to model fluids where large deformations occur, which is a characteristic of crash analyses). Structural failure was successfully implemented by coupling Lagrangian and Eulerian solvers. The ATB model allowed for the real-time interactions between the occupant and aircraft to be investigated, unlike previously where analyses of the occupant were performed in separate local models using accelerations derived from the global analyses results.

The results obtained from the crash analyses provide an indication of the forces transmitted to the occupant through the seat and restraint system, and the aircraft's ability to provide a survivable volume throughout the crash event. The explicit nonlinear dynamic finite element based methodology was successfully implemented for investigating the crashworthiness of small lightweight composite aircraft, satisfying the primary aim of this study.

Chapter 1 provides a review of fibre reinforced composite materials, the finite element method (FEM), ATDs and associated analysis codes, human tolerance limits to abrupt (de)accelerations, and crash dynamics and environment. The review of the FEM initially focuses on the fundamentals of FEA and then on the features specific to MSC Dytran as it is used throughout this study. Chapter 2 discusses the development of suitable numerical modelling techniques at the sub-component level and the implementation of these techniques within the full-scale crash analyses. Chapter 3 presents and discusses the full-scale crash analyses results for three impacts into rigid terrain and three impacts into soft soil terrain with varying aircraft pitch and impact angles. The results obtained from the crash analyses provide an indication of the forces transmitted to the occupant through the seat and restraint system, and the aircraft's ability to provide a survivable volume throughout the crash event. Chapter 4 provides a conclusion of the work performed in this study and highlights various areas for future work.

## LIST OF FIGURES

## LIST OF TABLES

# TABLE OF CONTENTS

# CHAPTER 1: LITERATURE REVIEW

## 1.1 Fibre reinforced composite materials

### 1.1.1 Introduction

In the context of this study, a composite material consists of a macroscopic combination of two or more distinct constituent materials or phases which are essentially insoluble in one another, having a recognisable interface between each constituent material as shown in Figure 1. An additional phase (interphase) may include coatings applied to the fibres. Composite materials are therefore considered to be heterogeneous. The constituent materials typically consist of reinforcing fibres embedded in a continuous matrix, where the combination of constituent materials results in superior structural properties when compared to the constituent materials alone. The fibres may be in different forms as shown in Figure 2; however the focus of this study is on continuous fibre reinforced composites as used in unidirectional lamina due to its typical application in the aerospace industry.

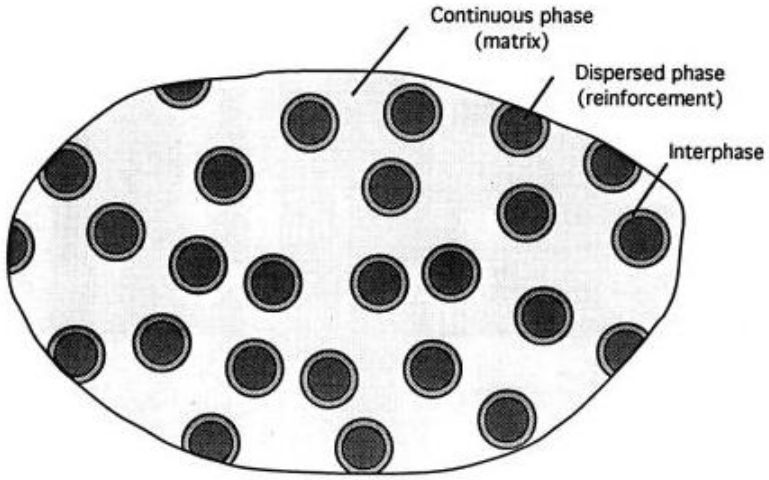


**Figure 1: Phases of fibrous composite materials [8]**

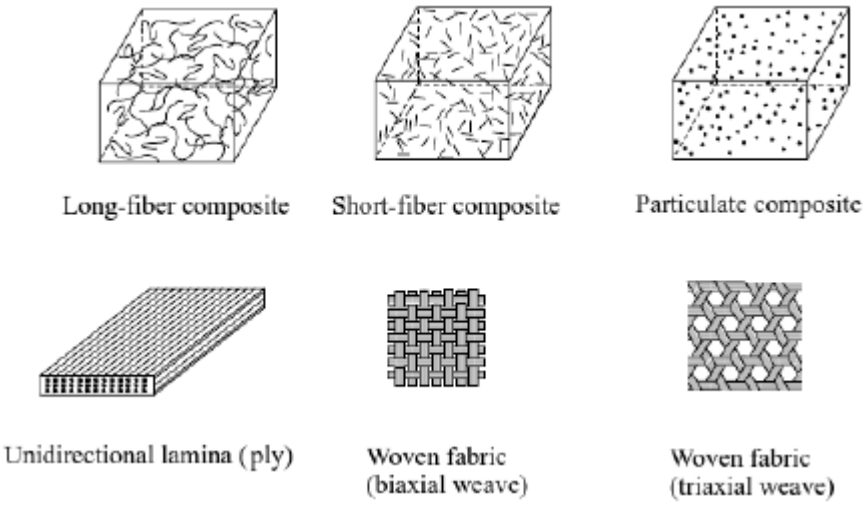


**Figure 2: Composite material systems [9]**

The application of composite materials in the aerospace industry is continuously growing, as they offer many advantages over traditional engineering materials such as aluminium. Some of the primary advantages composite materials have to offer include superior specific stiffness and strength, fatigue resistance, and design tailorability. Other advantages may be dimensional stability, corrosion resistance from moisture and various chemicals, and conductivity. High specific stiffness and strength materials make it possible to design structures with significant weight savings, thereby making aircraft increasingly efficient. Design tailorability refers to the many design variables for composite materials, which can be engineered to suit different applications. Design variables include the selection of constituent materials, volume fraction of constituent materials, fibre orientations, lamina thickness, and stacking sequence, amongst others. Dimensional stability may refer to the strains associated with temperature changes, and how suitable constituent materials may be selected to reduce or eliminate these strains within specified environmental operating conditions. Conductivity may refer to electrically conductivity or thermal conductivity. For example, composite materials can be tailored to be electrically non-conducting to prevent electrocution, and may also be tailored to have high thermal conductivity to maintain low temperatures.

### 1.1.2 Reinforcing fibres

A wide selection of fibres with different morphology, origin, size, and shape are available for use in composite materials. For convenience, a brief discussion of two common types of fibres used in the aerospace industry is given, namely glass fibres and carbon or graphite fibres. The performance of these fibres is graphically represented in Figure 3 and is discussed below. In addition, the performance of aramid fibres, a well-known fibre having high impact damage tolerance levels, is also shown in Figure 3 for comparative purposes only, and is not discussed. The fibres are supplied in the form of strands or tows, where each strand or tow consists of many untwisted individual continuous fibre filaments. The term strand is usually associated with glass fibres, whereas the term tow is usually associated with carbon or graphite fibres.

The two most common forms of glass fibres for structural applications are E-glass (electrical) and S-2 glass (high strength). E-glass is typically used where specific strength and high electrical resistivity are required. S-2 glass is typically used where high specific strength, specific stiffness, and stability under extreme temperature and corrosive environments are required. Figure 3 indicates that although glass fibres may have relatively low moduli when compared to alternative fibres, they are desirable due to their relatively low cost. Some commercial and military uses for glass fibres include thermal and electrical insulation, structural automotive products, pressure vessels, helicopter rotor blades, circuitry, and radomes.

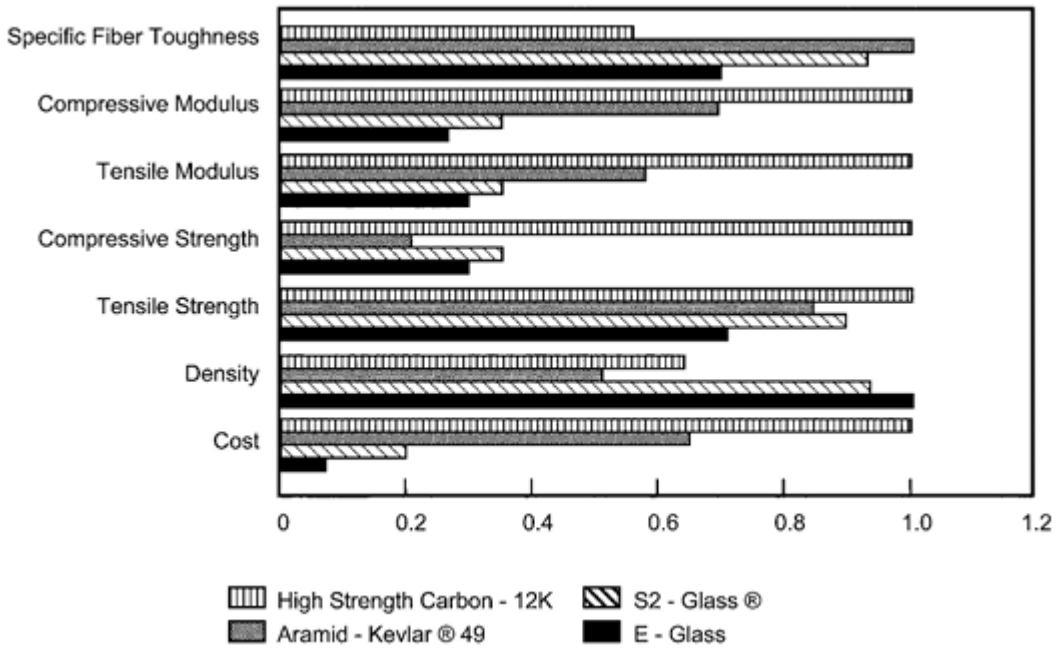


**Figure 3: Relative fibre cost and performance of some high strength fibres [10]**

Glass fibres are produced by drawing molten glass through tiny orifices in a gravity fed tank to form continuous filaments, which are then immediately quenched with a water or air spray. A chemical sizing (coating) is then applied to the filaments, which protects the filament surfaces and also binds them together. A large number of filaments are wound onto a high speed drum and gathered to form a strand. Individual filament diameters are typically between five to 20 micrometres [10]. A number of individual strands are usually then collected into a parallel bundle without twisting to form a roving. The production method described results in individual filaments that have small diameters, are isotropic, and are very flexible.

Carbon fibres typically have a carbon content of 80 to 95 percent, whereas graphite fibres typically have carbon content in excess of 99 percent. The terms carbon and graphite fibres are often used interchangeably, therefore the general term carbon will be used for both carbon and graphite fibres in

this study. Carbon fibres exhibit excellent fatigue properties, do not corrode, and as shown in Figure 3, carbon fibres exhibit high specific strength and stiffness; however they are relatively expensive. These properties make carbon fibre ideal for aerospace and military applications, especially where weight saving is critical. Formula One racing vehicles are renowned for their use of carbon fibres in various components such as the chassis, engine cover, wings, and suspension.

Generally, structural carbon filaments are manufactured by controlled pyrolysis (chemical decomposition by heat) from polyacrylonitrile (PAN) precursor fibres, rather than from rayon or petroleum based pitch precursor fibres. Although more expensive than using rayon, PAN is preferred as it yields almost double the carbon. The pitch process produces fibres that have lower strength than PAN produced fibres, but can produce high modulus fibres [10]. Individual carbon filaments have small diameters of four to 10 micrometres and tows can consist of 3000 to 30000 filaments, resulting in very flexible fibres (or tows). The microstructure of carbon fibres is heterogeneous. The morphology depends on the manufacturing process used, where for example PAN-based carbon fibres typically have an onion skin appearance. Carbon fibres thus have anisotropic properties [11].

### 1.1.3 Matrix materials

The matrix binds the reinforcing fibres in an orderly array and protects these fibres from the environment. The matrix transfers loading to the fibres and in the event fibre breakage occurs, the matrix redistributes the load to the remaining fibres. The matrix prevents premature failure due to fibre micro buckling under compression loading, and provides toughness, damage tolerance, and impact and abrasion resistance. The matrix properties may also determine the temperature usage range, moisture resistance, and thermal and oxidative stability [10]. Different matrix materials are used in

continuous fibre composites, such as polymers, metals (e.g. aluminium, titanium, and copper), and ceramics. Polymeric matrix materials are commonly used and are discussed for the purposes of this study.

Polymeric matrix materials can be classified as either thermoplastics or thermosets. Thermoplastics soften and can be reshaped with heat and pressure. High toughness, high volume, and low cost processing are potential advantages of thermoplastics. Thermoplastics have an operating temperature range in excess of 225 degrees Celsius [11]. Various thermoplastics in use include polypropylene, polyvinyl chloride, nylon, polyurethane, poly-ether-ether-ketone (PEEK), polyphenylene sulphide (PPS), and polysulfone. Thermosets do not soften and cannot be reshaped with heat and pressure. Commonly used thermosets are polyesters, epoxies, and polyimides. Polyesters are extensively used in commercial applications, particularly with glass fibres as reinforcement. Polyesters are relatively inexpensive, lightweight, have an operating temperature range up to 100 degrees Celsius [11], and have some resistance to environmental exposures. Although more expensive than polyesters, epoxies are extensively used for high-performance composites due to their excellent combination of strength, adhesion, lower shrinkage on curing, processing versatility, and lower moisture absorption. The maximum operating temperature range for epoxies is approximately 175 degrees Celsius [11]. Polyimides are intended for high temperature applications around 300 degrees Celsius [11]; however they are difficult to fabricate. Noteworthy potential problems with the use of polymers as a matrix material are the limited operating temperature ranges, low transverse strength, high residual stresses due to large differences in the thermal expansion coefficients between the fibres and matrix, and susceptibility to environmental degradation due to moisture and radiation.

### 1.1.4 Coordinate systems

In the discussions that follow, two Cartesian coordinate systems will be employed for continuous fibre reinforced composite materials, namely a principal material coordinate system and a global coordinate system as shown in Figure 4. The principal material coordinate system is designated by *1-2-3 axes* with the *1-axis* parallel or longitudinal to the fibre direction and the *2-axis* transverse to the fibre direction. The global coordinate system is attached to a fixed reference point and is designated by *x-y-z axes*. The angle $\theta$ (degrees) specifies the fibre orientation of continuous unidirectional laminae with respect to the global *x-axis*. The angle $\theta$ is positive in the counter clockwise direction if the *1-axis* and *z-axis* point vertically upwards.

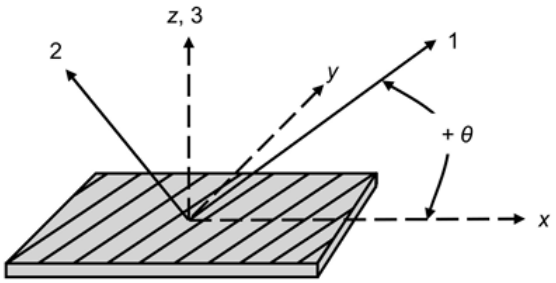


**Figure 4: Global *x-y-z* coordinate system, principal material *1-2-3* coordinate system, and fibre orientation angle $\theta$ for continuous fibre reinforced composite materials [10]**

### 1.1.5 Unidirectional laminae

Unidirectional laminae (also referred to as plies) are composed of continuous fibres embedded in a matrix, where all fibres are aligned in the same direction. Continuous fibres have lengths much greater than their cross-sectional dimensions, where the fibre lengths are generally comparable to the overall dimensions of the composite structure or part. Many laminae may

be stacked together with the same fibre orientation to create a single lamina. Laminae have different properties parallel (i.e. longitudinal to the fibre axis) and perpendicular to the fibres. The continuous fibres provide desirable stiffness and strength properties parallel to the fibres as the loading is carried by the fibres. These longitudinal properties are typically significantly higher than in the transverse directions, because the load must be carried by the significantly weaker matrix in the transverse directions.

### 1.1.6 Laminates

Generally, composite structures are composed of more than one lamina stacked together at various orientations to form a laminate as shown in Figure 5 and Figure 6. Since each lamina may have its own specified fibre orientation, the strength of the laminate may be enhanced in the primary loading direction. Longitudinal (parallel to the fibres) tension and compression loads are carried by the fibres, whilst the matrix distributes the loads between the fibres in tension and prevents fibre buckling in compression. Additionally, the matrix is the primary load carrier for interlaminar shear (i.e. shear between the layers) and tension in the transverse direction.

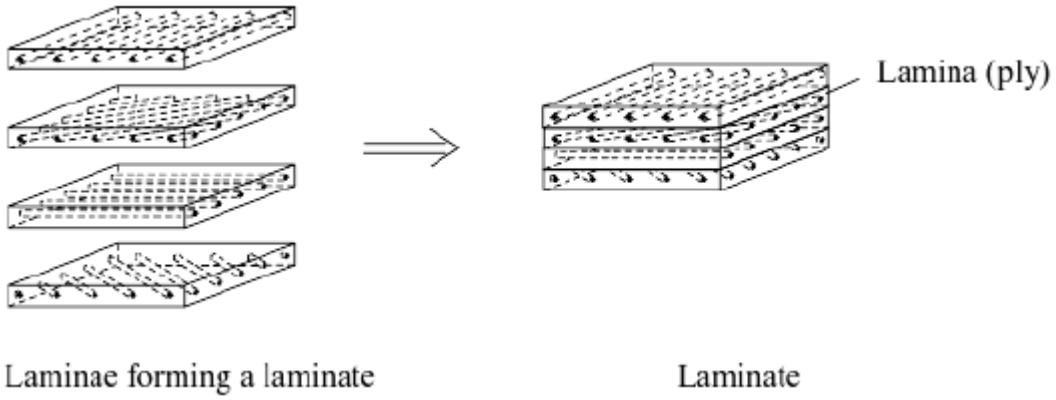


**Figure 5: Composite laminate [9]**

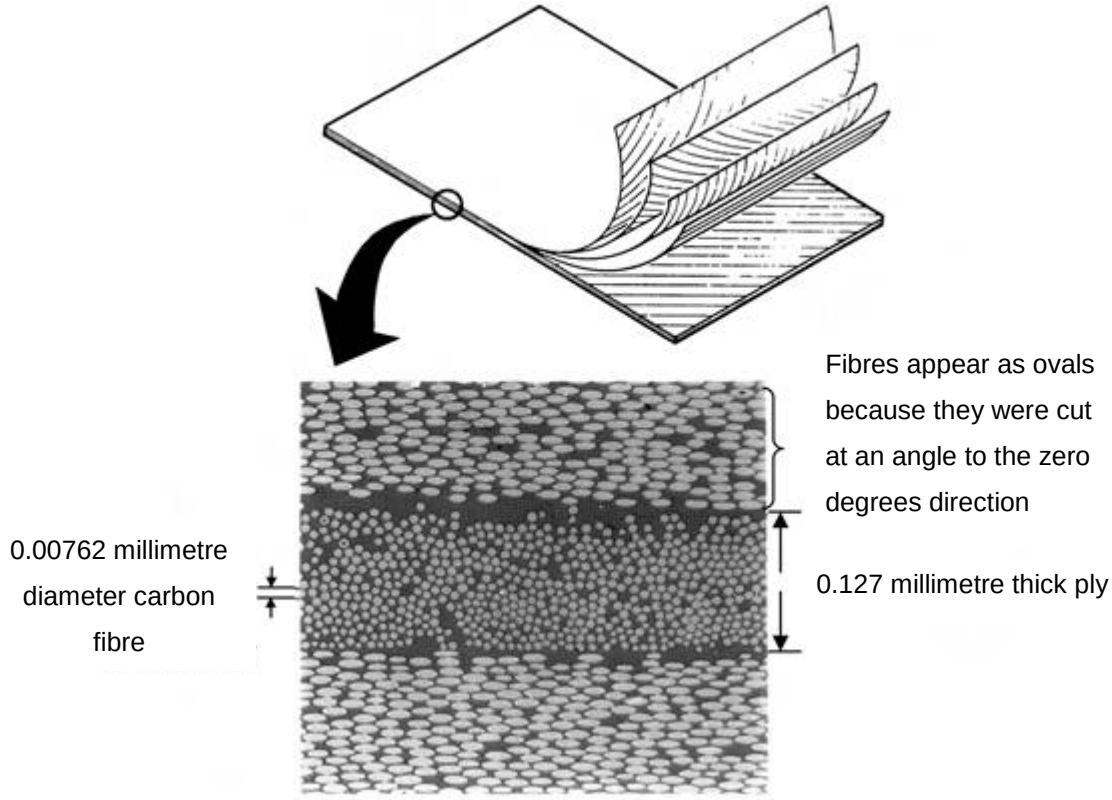


**Figure 6: Cross-section of a cross-plied continuous carbon fibre / epoxy laminate [10]**

Typical laminate notation is used to describe the stacking sequence of laminae within a laminate, where fibre orientations are listed from a laminate reference angle. The laminae orientations are listed starting from the top lamina to the bottom lamina of the laminate. Numerical subscripts within the square brackets indicate the number of adjacent laminae. Outside the square brackets, the subscript s indicates that the pattern is repeated in reverse order, which is known as a symmetric laminate. A multiplier numerical subscript outside the square brackets may also be used to indicate multiple groups of laminae. An overbar is used to indicate the central lamina of a laminate, which is not repeated. Examples are given below.

Example 1:

$$[45°/-45°/0°/0°/45°/-45°/0°/0°/0°/0°/-45°/45°/0°/0°/-45°/45°]$$

In laminate notation,

$$[\pm 45°/0_2^o]_{2s}$$

Example 2:

$$[45°/-45°/0°/0°/90°/0°/0°/-45°/45°]$$

In laminate notation,

$$\left[\pm 45°/0_2^o/\overline{90°}\right]_s$$

Metals and polymers are generally treated as isotropic materials, meaning that they have identical material properties in all directions. By contrast, composite materials are generally anisotropic, meaning that they have different material properties in all directions. They can be further classified as orthotropic. An orthotropic material has three mutually perpendicular planes of symmetry with respect to the alignment of the fibres, with differing material properties in all three directions. A transversely isotropic material is also orthotropic as it has three planes of symmetry; however the material is treated as isotropic in one of the planes of symmetry. A unidirectional composite material with all the fibres aligned along the *1-axis* is known as transversely isotropic, where the *2-3 plane* is treated as isotropic, viz.

$$E_{22} = E_{33};\ G_{12} = G_{13};\ \nu_{12} = \nu_{13}$$

where:

$E$ = modulus of elasticity

$G$ = shear modulus of elasticity

$\nu$ = Poisson's ratio

The first subscript identifies the axis normal to the plane on which the variable acts, and the second gives the direction on that plane.

In a symmetric laminate, the lamina fibre orientations are symmetrical about the laminate's mid-plane. Each lamina above the mid-plane has identical fibre orientation, thickness, and material properties as its corresponding lamina located symmetrically about the mid-plane (i.e. located at an equal distance below the mid-plane).

Balanced laminates are orthotropic and are defined as laminates where for every positive $\theta$ lamina orientation; there is a lamina of negative $\theta$ orientation having identical thickness and material properties. A balanced laminate does not have to be symmetric.

Quasi-isotropic laminates are orthotropic and are deemed important because they exhibit isotropic elastic behaviour in the *1-2 plane*. They are not termed isotropic as both the bending response and strength of these laminates do not exhibit isotropic characteristics. They are symmetric laminates consisting of *N* equal thickness laminae $(\frac{1}{2}N \geq 3)$ and $\frac{1}{2}N$ equal angles $\Delta\theta$ between fibre orientations. The material properties are identical for all laminae. An example quasi-isotropic lay-up is shown in Figure 7. For $\frac{1}{2}N$ equal angles of $\Delta\theta$:

$$\Delta\theta = \frac{\pi}{\frac{1}{2}N} \tag{1}$$

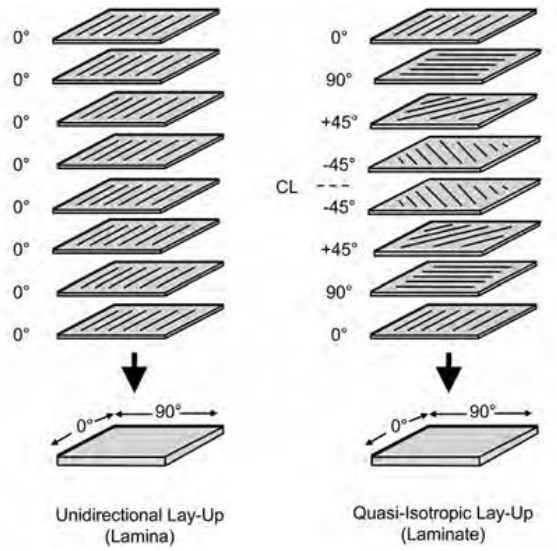


**Figure 7: Unidirectional and quasi-isotropic lay-ups [10]**

### 1.1.7 Fibre volume fraction

Fibre volume content has a significant effect on the properties of composite materials, as it is the fibres that carry the majority of applied loads. The amount of fibre present in a composite material is usually expressed as a percentage volume fraction of the entire composite material. Typically, fibre volume fractions for continuous unidirectional fibre reinforced composite materials range between 50 and 70 percent of the total composite volume. A fibre volume fraction of 100 percent is not physically possible due to the shape of the fibres, and is undesirable for wet-out (i.e. the impregnation of resin into the fibres). The total volume content is defined by Equation 2, where unity represents 100 percent fibre volume.

$$V_f + V_m = 1 \qquad (2)$$

where:

$V_f$ = fibre volume content

$V_m$ = matrix volume content

### 1.1.8 Rule of mixtures

The rule of mixtures may be used to develop approximate expressions for effective (average) properties of continuous unidirectional fibre laminae. The rule of mixtures expresses effective material properties in terms of the properties and volume fractions of the individual constituent materials (i.e. fibre and matrix). Herakovich [11] has shown that the rule of mixtures can be used to predict approximate effective axial and transverse moduli, amongst other effective properties such as Poisson's ratio $\nu_{12}$ and shear modulus $G_{12}$. When a lamina is loaded in the fibre direction, the fibres and matrix function in parallel (analogous to springs connected in parallel), with the majority of the load carried by the fibres. The effective axial modulus can thus be approximated using Equation 3 and has been rearranged in Equation 4. As can be seen in Equation 4 and Figure 8, the effective axial modulus is linearly proportional to the fibre volume fraction, highlighting the importance of fibre volume fraction and its effect on material properties.

$$E_{11} = E_f.V_f + E_m.V_m \tag{3}$$

$$E_{11} = (E_f - E_m)V_f + E_m \tag{4}$$

where:

$E_{11}$ = effective axial modulus (fibre direction)
$E_f$ = fibre modulus
$E_m$ = matrix modulus

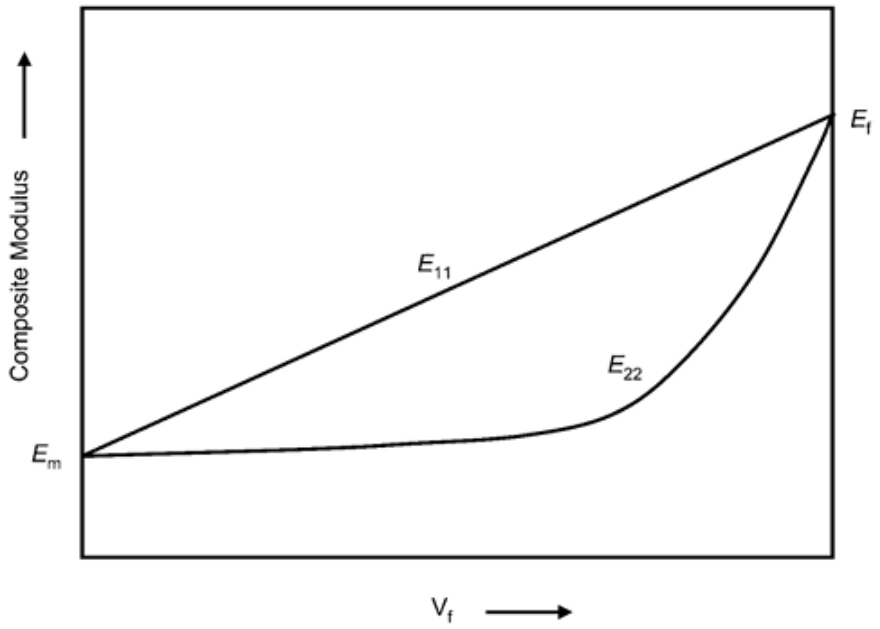


**Figure 8: Variation of composite modulus of a unidirectional 0º lamina as a function of fibre volume fraction [10]**

When a lamina is loaded in the transverse direction to the fibres, the fibres and matrix function in series (analogous to springs connected in series) with both constituents carrying equal loads. The effective transverse modulus can thus be approximated using Equation 5 and has been rearranged in Equation 6. As can be seen in Equation 6 and Figure 8, the relationship between the effective transverse modulus and fibre volume fraction is non-linear, once again highlighting the importance of fibre volume fraction and its effect on material properties.

$$\frac{1}{E_{22}} = \frac{V_f}{E_f} + \frac{V_m}{E_m} \tag{5}$$

$$E_{22} = \frac{E_m}{\left[V_f\left(\frac{E_m}{E_f} - 1\right) + 1\right]} \tag{6}$$

where:

$E_{22}$ = effective transverse modulus (perpendicular to the fibres)

### 1.1.9 Analysis of laminates

Numerous theories have been developed for the analysis of laminated composite plates. Two common approaches are classical plate lamination theory (CPLT) and first-order shear deformable theory (FSDT). Prior to the discussions of the two lamination theories, the stress-strain relations of unidirectional laminae must first be understood. For simplicity reasons, the stress-strain relations will be discussed within the context of CPLT; however the differences between CPLT and FSDT will be highlighted in the discussions that follow.

The following cross-section of a laminate with *N* laminae shown in Figure 9 will be considered for the discussion on CPLT as well as FSDT.

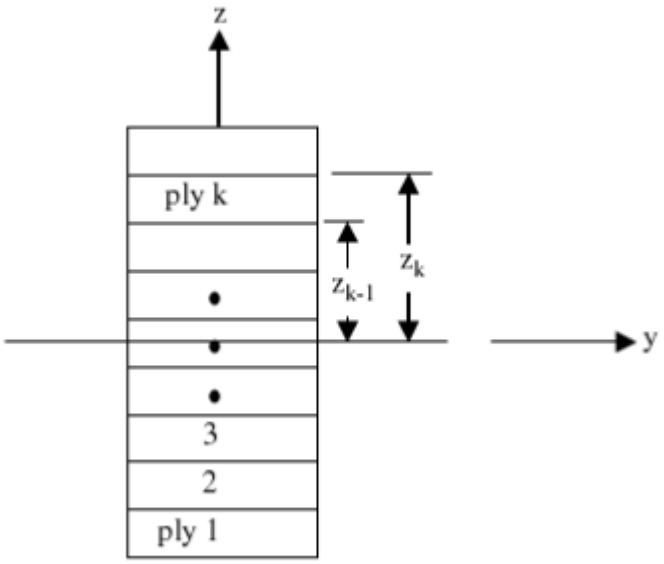


**Figure 9: Coordinate and lamina (ply) numbering system for a typical laminate [12]**

**Lamina stress-strain relations for classical plate lamination theory**

For the stress-strain relations of unidirectional laminae, the laminae are treated as effective homogenous, transversely isotropic materials. The constitutive equation for transversely isotropic materials in the principal material coordinates (*1-2-3*) is shown to be [10, 13]:

$$\begin{Bmatrix} \varepsilon_{11} \\ \varepsilon_{22} \\ \varepsilon_{33} \\ 2\varepsilon_{23} \\ 2\varepsilon_{13} \\ 2\varepsilon_{12} \end{Bmatrix} = \begin{bmatrix} \frac{1}{E_{11}} & -\frac{\nu_{12}}{E_{11}} & -\frac{\nu_{12}}{E_{11}} & 0 & 0 & 0 \\ -\frac{\nu_{12}}{E_{11}} & \frac{1}{E_{22}} & -\frac{\nu_{23}}{E_{22}} & 0 & 0 & 0 \\ -\frac{\nu_{12}}{E_{11}} & -\frac{\nu_{23}}{E_{22}} & \frac{1}{E_{22}} & 0 & 0 & 0 \\ 0 & 0 & 0 & \frac{1}{G_{23}} & 0 & 0 \\ 0 & 0 & 0 & 0 & \frac{1}{G_{12}} & 0 \\ 0 & 0 & 0 & 0 & 0 & \frac{1}{G_{12}} \end{bmatrix} \begin{Bmatrix} \sigma_{11} \\ \sigma_{22} \\ \sigma_{33} \\ \sigma_{23} \\ \sigma_{13} \\ \sigma_{12} \end{Bmatrix} \tag{7}$$

which may be written as:

$$\{\varepsilon_l\} = [S]\{\sigma_l\} \tag{8}$$

The following symmetry relations have been taken into account in Equation 7:

$$\frac{\nu_{21}}{E_{22}} = \frac{\nu_{12}}{E_{11}} = \frac{\nu_{31}}{E_{33}} = \frac{\nu_{13}}{E_{11}};\ \frac{\nu_{23}}{E_{22}} = \frac{\nu_{32}}{E_{33}} \tag{9}$$

and

$$E_{33} = E_{22};\ G_{13} = G_{12} \tag{10}$$

$$G_{23} = \frac{E_{22}}{2(1+\nu_{23})}$$

$$\nu_{13} = \nu_{12}$$

The compliance matrix [S] relates the stress and strain components in the principal material coordinate system and is denoted by subscript $l$. Engineering shear strains $(\gamma_{ij})$ rather than tensorial shear strains $(\varepsilon_{ij})$ are commonly used in lamina analysis, therefore a factor of two has been introduced in Equation 7 (i.e. engineering shear strain is twice the tensorial shear strain).

In addition, a plane state of stress is assumed where $\sigma_{13}$, $\sigma_{23}$, and $\sigma_{33}$ are all equal to zero as this occurs for both in-plane loading and bending at a sufficient distance from the lamina edges (note that the transverse shear stresses $\sigma_{13}$ and $\sigma_{23}$ are not equal to zero for FSDT). Unidirectional laminates are almost always loaded in plane stress conditions (i.e. in the *1-2* or *x-y* plane) as loading along the *3-axis* (or *z-axis*) can have catastrophic consequences since there are no fibres parallel to the loading direction, therefore the load will be carried by the weaker matrix. The plane stress constitutive equation in the principal material coordinates for CPLT is shown to be [13]:

$$\begin{Bmatrix} \varepsilon_{11} \\ \varepsilon_{22} \\ 2\varepsilon_{12} \end{Bmatrix} = \begin{bmatrix} \frac{1}{E_{11}} & \frac{-\nu_{12}}{E_{11}} & 0 \\ \frac{-\nu_{12}}{E_{11}} & \frac{1}{E_{22}} & 0 \\ 0 & 0 & \frac{1}{G_{12}} \end{bmatrix} \begin{Bmatrix} \sigma_{11} \\ \sigma_{22} \\ \sigma_{12} \end{Bmatrix} \tag{11}$$

The above equation may be inverted to obtain:

$$\{\sigma_l\} = [Q]\{\varepsilon_l\} \tag{12}$$

The reduced lamina stiffness matrix $[Q]$ is defined as the inverse of the compliance matrix. The reduced lamina stiffness matrix and its terms for CPLT are defined by [10, 13]:

$$[Q] = \begin{bmatrix} Q_{11} & Q_{12} & 0 \\ Q_{12} & Q_{22} & 0 \\ 0 & 0 & Q_{66} \end{bmatrix} \tag{13}$$

where:

$$Q_{11} = \frac{E_{11}}{1 - \nu_{12}^2 \frac{E_{22}}{E_{11}}} = \frac{E_{11}}{1 - \nu_{12}\nu_{21}} \tag{14}$$

$$Q_{22} = \frac{E_{22}}{1 - \nu_{12}^2 \frac{E_{22}}{E_{11}}} = \frac{E_{22}}{1 - \nu_{12}\nu_{21}}$$

$$Q_{12} = \frac{\nu_{12}E_{22}}{1 - \nu_{12}^2 \frac{E_{22}}{E_{11}}} = \frac{\nu_{12}E_{22}}{1 - \nu_{12}\nu_{21}} = \frac{\nu_{21}E_{11}}{1 - \nu_{12}\nu_{21}}$$

$$Q_{66} = G_{12}$$

Lamina response in directions other than in the principal material coordinate system may be defined using the following transformation relations for stress [13]:

$$\begin{Bmatrix} \sigma_{xx} \\ \sigma_{yy} \\ \sigma_{xy} \end{Bmatrix} = \begin{bmatrix} m^2 & n^2 & -2mn \\ n^2 & m^2 & 2mn \\ mn & -mn & m^2 - n^2 \end{bmatrix} \begin{Bmatrix} \sigma_{11} \\ \sigma_{22} \\ \sigma_{12} \end{Bmatrix} \tag{15}$$

which may be written as:

$$\{\sigma_x\} = [\theta]\{\sigma_l\} \tag{16}$$

where $m = \cos\theta$, $n = \sin\theta$, the subscript $x$ denotes the laminate (or arbitrary) coordinate system, and $[\theta]$ is the transformation matrix for stress. In terms of strain, a different transformation matrix is required because engineering (rather than tensorial) shear strains are utilised, therefore [13]:

$$\begin{Bmatrix} \varepsilon_{xx} \\ \varepsilon_{yy} \\ 2\varepsilon_{xy} \end{Bmatrix} = \begin{bmatrix} m^2 & n^2 & -mn \\ n^2 & m^2 & mn \\ 2mn & -2mn & m^2 - n^2 \end{bmatrix} \begin{Bmatrix} \varepsilon_{11} \\ \varepsilon_{22} \\ 2\varepsilon_{12} \end{Bmatrix} \tag{17}$$

which may be written as:

$$\{\varepsilon_x\} = [\Psi]\{\varepsilon_l\} \tag{18}$$

where $[\Psi]$ is the transformation matrix for engineering strains.

The plane stress constitutive equation in the laminate coordinate system (*x-y-z*) of the $k^{th}$ layer can be found by combining Equation 16 and Equation 18 with Equation 12, resulting in [10]:

$$\begin{Bmatrix} \sigma_{xx} \\ \sigma_{yy} \\ \sigma_{xy} \end{Bmatrix}^k = \begin{bmatrix} \overline{Q}_{11} & \overline{Q}_{12} & \overline{Q}_{16} \\ \overline{Q}_{12} & \overline{Q}_{22} & \overline{Q}_{26} \\ \overline{Q}_{16} & \overline{Q}_{26} & \overline{Q}_{66} \end{bmatrix}^k \begin{Bmatrix} \varepsilon_{xx} \\ \varepsilon_{yy} \\ 2\varepsilon_{xy} \end{Bmatrix}^k \tag{19}$$

which may be written as:

$$\{\sigma_x\}^k = \left[\overline{Q}\right]^k \{\varepsilon_x\}^k \tag{20}$$

The transformed reduced stiffness matrix $\left[\overline{Q}\right]$ relates stress and strain in the laminate coordinate system. The terms within $\left[\overline{Q}\right]$ are [13]:

$$\overline{Q}_{11} = Q_{11}m^4 + Q_{22}n^4 + 2m^2n^2(Q_{12} + 2Q_{66}) \quad (21)$$

$$\overline{Q}_{12} = m^2n^2(Q_{11} + Q_{22} - 4Q_{66}) + (m^4 + n^4)Q_{12}$$

$$\overline{Q}_{16} = [Q_{11}m^2 - Q_{22}n^2 - (Q_{12} + 2Q_{66})(m^2 - n^2)]mn$$

$$\overline{Q}_{22} = Q_{11}n^4 + Q_{22}m^4 + 2m^2n^2(Q_{12} + 2Q_{66})$$

$$\overline{Q}_{26} = [Q_{11}n^2 - Q_{22}m^2 + (Q_{12} + 2Q_{66})(m^2 - n^2)]mn$$

$$\overline{Q}_{66} = (Q_{11} + Q_{22} - 2Q_{12})m^2n^2 + Q_{66}(m^2 - n^2)^2$$

As can be seen in Equation 21, $[\overline{Q}]$ is symmetric and fully populated with additional nonzero coefficients $\overline{Q}_{16}$ and $\overline{Q}_{26}$. These two additional coefficients define the coupling between in-plane extensional and shear loadings. Extensional-shear coupling does not occur for orthotropic materials when the loading direction is parallel or transverse to the fibres. This is evident for angle $\theta$ equal to zero or ninety degrees as $\overline{Q}_{16}$ and $\overline{Q}_{26}$ will then equal zero. Figure 10 shows extensional-shear coupling for nonzero values of $\overline{Q}_{16}$ and $\overline{Q}_{26}$ (i.e. the loading direction is not parallel or perpendicular to the fibres). Additionally, the elastic constants in an arbitrary coordinate system are functions of all of the elastic constants in the principal material directions as well as the fibre orientation. A typical example of the variation of elastic modulus with fibre orientation for a unidirectional lamina is shown in Figure 11.

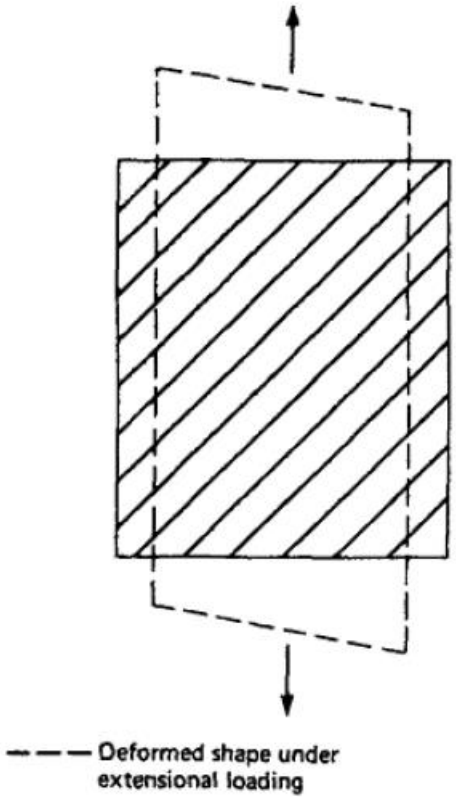


**Figure 10: Extensional-shear coupling [13]**

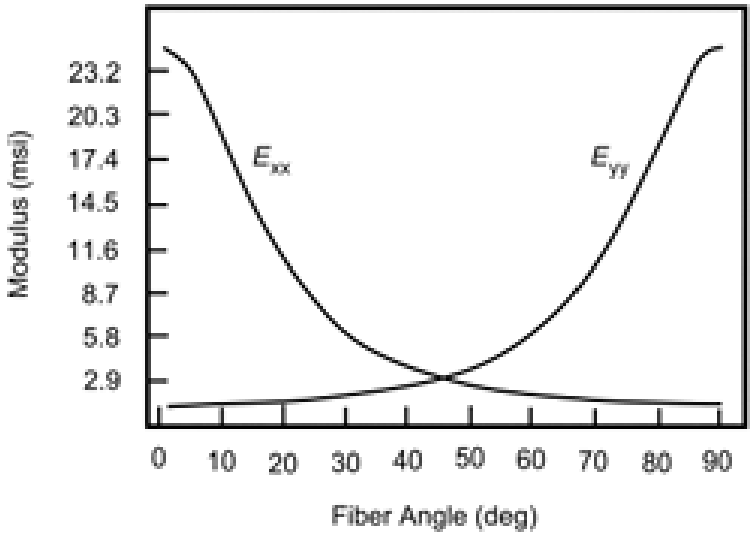


**Figure 11: Variation of elastic modulus with fibre orientation for a unidirectional lamina [10]**

**Classical plate lamination theory**

The linear elastic response of thin, flat laminates subjected to in-plane loads and bending moments can be described using CPLT. The assumptions in CPLT are: the thickness of the plate is much smaller than the in-plane dimensions; the strains in the deformed plate are small compared to unity; transverse normals to the undeformed plate surface remain normal to the deformed plate surface; vertical deflection does not vary through the thickness; stress normal to the plate surface is negligible; the laminae are perfectly bonded together; individual laminae are treated as homogenous; and individual laminae properties are orthotropic or transversely isotropic [10].

Based on these assumptions, it can be shown that the in-plane displacements consist of a mid-surface displacement (designated by superscript 0), plus a linear displacement through the thickness, represented by:

$$\begin{aligned} \varepsilon_{xx} &= \varepsilon_{xx}^{0} + z\kappa_{xx} \\ \varepsilon_{yy} &= \varepsilon_{yy}^{0} + z\kappa_{yy} \\ 2\varepsilon_{xy} &= 2\varepsilon_{xy}^{0} + z\kappa_{xy} \end{aligned} \tag{22}$$

where $\kappa$ refers to curvatures in the laminate and $z$ is the distance from the mid-plane in the thickness direction. The linear strain displacement and curvature relations are:

$$\varepsilon_{xx}^{0} = \frac{\partial u}{\partial x};\ \varepsilon_{yy}^{0} = \frac{\partial v}{\partial y};\ 2\varepsilon_{xy}^{0} = \frac{\partial u}{\partial y} + \frac{\partial v}{\partial x} \tag{23}$$

$$\kappa_{xx} = -\frac{\partial^2 w}{\partial x^2};\ \kappa_{yy} = -\frac{\partial^2 w}{\partial y^2};\ \kappa_{xy} = -2\frac{\partial^2 w}{\partial x \partial y}$$

where $u$, $v$ and $w$ represent the displacements at any point in the $x$, $y$ and $z$ directions respectively.

As can be seen by Equation 22, the strain at any point in the laminate is defined as the sum of the mid-surface strain and curvature, multiplied by the distance from the mid-surface.

The applied force ($N$) and moment resultants ($M$) experienced by a laminate are shown in Figure 12. It can be shown that the applied force and moment resultants are related to the mid-plane strains and curvatures by:

$$\{N\} = [A]\{\varepsilon^0\} + [B]\{\kappa\} \tag{24}$$

$$\{M\} = [B]\{\varepsilon^0\} + [D]\{\kappa\} \tag{25}$$

The laminate extensional stiffnesses are given by:

$$[A] = \sum_{k=1}^{N} \left[\overline{Q}\right]^k (z_k - z_{k-1}) \tag{26}$$

The laminate coupling stiffnesses are given by:

$$[B] = \frac{1}{2}\sum_{k=1}^{N} \left[\overline{Q}\right]^k (z_k^2 - z_{k-1}^2) \tag{27}$$

The laminate bending stiffnesses are given by:

$$[D] = \frac{1}{3}\sum_{k=1}^{N} \left[\overline{Q}\right]^k (z_k^3 - z_{k-1}^3) \tag{28}$$

where $N$ is the total number of laminae, $k$ is the number of a particular lamina under consideration, and $z_k - z_{k-1}$ is the lamina thickness.

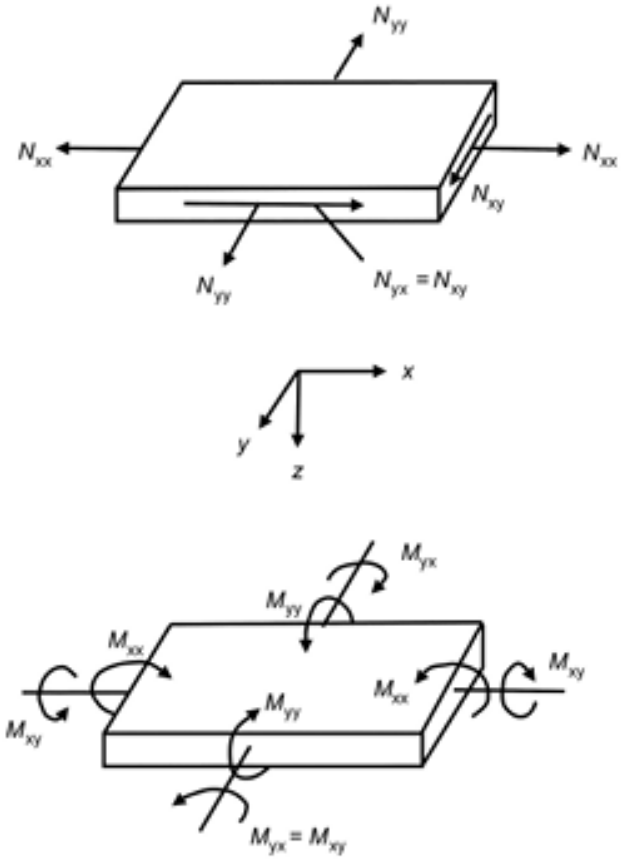


**Figure 12: Laminate applied force and moment resultants [10]**

Equation 24 and Equation 25 combine to give the fundamental equation of CPLT:

$$\begin{Bmatrix} N_x \\ N_y \\ N_{xy} \\ M_x \\ M_y \\ M_{xy} \end{Bmatrix} = \begin{bmatrix} A_{11} & A_{12} & A_{16} & B_{11} & B_{12} & B_{16} \\ A_{12} & A_{22} & A_{26} & B_{12} & B_{22} & B_{26} \\ A_{16} & A_{26} & A_{66} & B_{16} & B_{26} & B_{66} \\ B_{11} & B_{12} & B_{16} & D_{11} & D_{12} & D_{16} \\ B_{12} & B_{22} & B_{26} & D_{12} & D_{22} & D_{26} \\ B_{16} & B_{26} & B_{66} & D_{16} & D_{26} & D_{66} \end{bmatrix} \begin{Bmatrix} \varepsilon_{xx}^0 \\ \varepsilon_{yy}^0 \\ 2\varepsilon_{xy}^0 \\ \kappa_{xx} \\ \kappa_{yy} \\ \kappa_{xy} \end{Bmatrix} \quad (29)$$

Examination of Equation 29 reveals various types of coupling that may occur. $A_{ij}$ elements represent the in-plane stiffnesses that relate in-plane forces to in-plane deformations. Non-zero $A_{16}$ and $A_{26}$ elements result in extensional-shear coupling. $D_{ij}$ elements represent the bending stiffnesses that relate the moments to the curvatures. Non-zero $D_{16}$ and $D_{26}$ elements result in bending-twisting coupling. $B_{ij}$ elements represent in-plane-out-of-plane coupling stiffnesses that relate in-plane forces to the curvatures, and the moments to the in-plane deformations. Non-zero $B_{ij}$ elements result in in-plane-out-of-plane coupling, where in-plane forces cause out-of-plane deformations, and the moments cause in-plane deformations. Non-zero $B_{16}$ and $B_{26}$ elements result in extension-twist coupling and bending-shear coupling. An illustration of the coupling terms is shown in Figure 13. When the element in the last column is zero, there is no coupling. The coupling terms $A_{26}$, $D_{26}$, $B_{26}$, and $B_{22}$ can be illustrated in a similar manner by applying a force $N_y$ and a moment $M_y$ in the y-z plane [9].

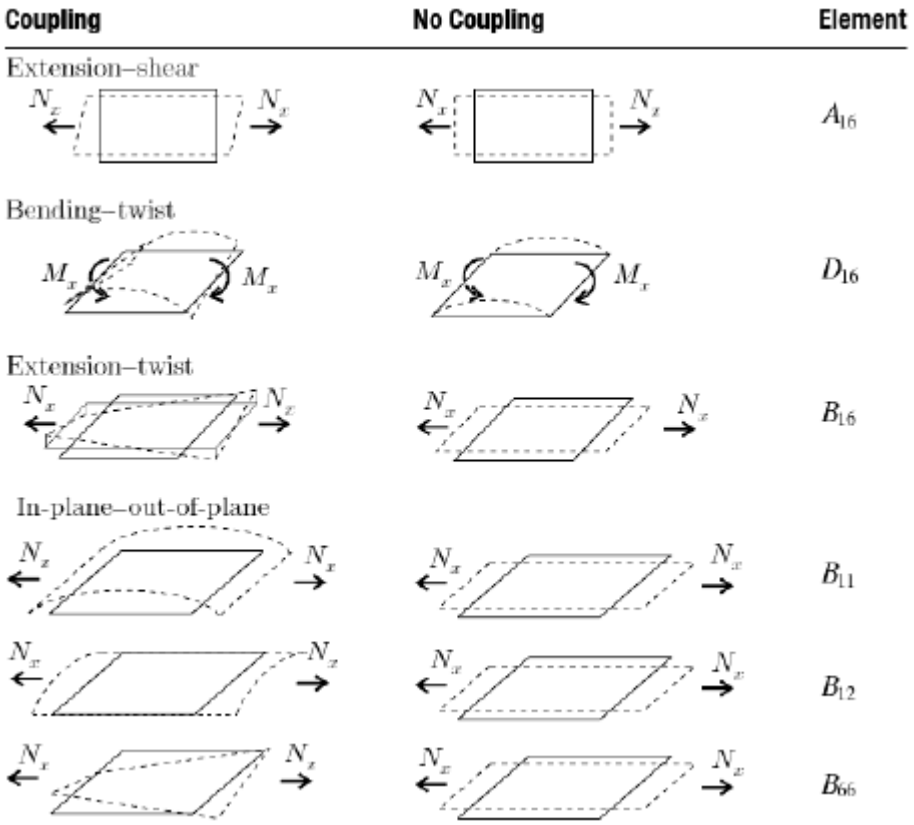


**Figure 13: Illustration of the coupling terms $A_{ij}$, $D_{ij}$, and $B_{ij}$ for composite materials [9]**

In orthotropic laminates, the $A_{16}$, $A_{26}$, $B_{16}$, $B_{26}$, $D_{16}$, and $D_{26}$ elements equal zero; therefore eliminating extension-shear coupling, bending-twisting coupling, and extension-twisting coupling. This example highlights the importance of lamina orientation and stacking sequence when constructing laminates.

**Lamina stress-strain relations for first-order shear deformable theory**

In CPLT, transverse shear strains are neglected and therefore the theory is more suited for thin laminated structures. For thicker laminated composite plates, transverse shear deformations are considered important to achieve better predictions of the response of laminates. The FSDT proposed by Mindlin is based on the assumption that the displacement $w$ is constant

through the thickness whilst the displacements $u$ (in the $x$ direction) and $v$ (in the $y$ direction) vary linearly through the thickness of each layer [14]. Unlike CPLT, the transverse normals *do not* remain perpendicular to the mid-surface after deformation for FSDT, therefore transverse shear strains are included. Transverse shear strains and therefore transverse shear stresses are constant through the laminate thickness in FSDT; however it is known that for laminated composite plates, the transverse shear stresses at the very least vary quadratically through the laminate layers. Different variations of the FSDT exist; however that of Thai and Choi [15] is discussed.

The reduced lamina stiffness matrix and its terms for FSDT are defined by [15]:

$$\begin{Bmatrix} \sigma_{11} \\ \sigma_{22} \\ \sigma_{12} \\ \sigma_{23} \\ \sigma_{13} \end{Bmatrix} = \begin{bmatrix} Q_{11} & Q_{12} & 0 & 0 & 0 \\ Q_{12} & Q_{22} & 0 & 0 & 0 \\ 0 & 0 & Q_{66} & 0 & 0 \\ 0 & 0 & 0 & Q_{44} & 0 \\ 0 & 0 & 0 & 0 & Q_{55} \end{bmatrix} \begin{Bmatrix} \varepsilon_{11} \\ \varepsilon_{22} \\ 2\varepsilon_{12} \\ 2\varepsilon_{23} \\ 2\varepsilon_{13} \end{Bmatrix} \tag{30}$$

where the additional terms for FSDT are:

$$Q_{44} = G_{23};\ Q_{55} = G_{13} \tag{31}$$

The plane stress constitutive equation in an arbitrary coordinate system for FSDT is shown in Equation 32, where $[\overline{Q}]$ relates stress and strain in the laminate coordinate system [15]:

$$\begin{Bmatrix} \sigma_{xx} \\ \sigma_{yy} \\ \sigma_{xy} \\ \sigma_{yz} \\ \sigma_{xz} \end{Bmatrix} = \begin{bmatrix} \overline{Q}_{11} & \overline{Q}_{12} & \overline{Q}_{16} & 0 & 0 \\ \overline{Q}_{12} & \overline{Q}_{11} & \overline{Q}_{26} & 0 & 0 \\ \overline{Q}_{16} & \overline{Q}_{26} & \overline{Q}_{66} & 0 & 0 \\ 0 & 0 & 0 & \overline{Q}_{44} & \overline{Q}_{45} \\ 0 & 0 & 0 & \overline{Q}_{45} & \overline{Q}_{55} \end{bmatrix} \begin{Bmatrix} \varepsilon_{xx} \\ \varepsilon_{yy} \\ 2\varepsilon_{xy} \\ 2\varepsilon_{yz} \\ 2\varepsilon_{xz} \end{Bmatrix} \tag{32}$$

The additional terms within $[\overline{Q}]$ for FSDT are:

$$\bar{Q}_{44} = Q_{44}m^2 + Q_{55}n^2 \quad (33)$$
$$\bar{Q}_{45} = (Q_{55} - Q_{44})mn$$
$$\bar{Q}_{55} = Q_{55}m^2 + Q_{44}n^2$$

**First-order shear deformable theory**

In the FSDT presented by Thai and Choi [15], the transverse displacement $w$ is divided into bending ($w_b$) and shear ($w_s$) parts (i.e. $w = w_b + w_s$). The resulting strain components for FSDT are similar to those of CPLT; however additional transverse shear strain components are considered for FSDT as shown by Equation 34. The superscripts and subscripts $b$ and $s$ denote bending and shear components.

$$\varepsilon_{xx} = \varepsilon_{xx}^0 + z\kappa_{xx}^b \quad (34)$$
$$\varepsilon_{yy} = \varepsilon_{yy}^0 + z\kappa_{yy}^b$$
$$2\varepsilon_{xy} = 2\varepsilon_{xy}^0 + z\kappa_{xy}^b$$
$$2\varepsilon_{xz} = 2\varepsilon_{xz}^0$$
$$2\varepsilon_{yz} = 2\varepsilon_{yz}^0$$

where [16]:

$$\kappa_{xx}^b = -\frac{\partial^2 w_b}{\partial x^2};\ \kappa_{yy}^b = -\frac{\partial^2 w_b}{\partial y^2};\ \kappa_{xy}^b = -2\frac{\partial^2 w_b}{\partial x \partial y} \quad (35)$$
$$2\varepsilon_{yz} = \frac{\partial w_s}{\partial y}; 2\varepsilon_{xz} = \frac{\partial w_s}{\partial x}$$

Following similar processes as for CPLT, the fundamental equation for FSDT is shown to be [15, 17]:

$$\begin{Bmatrix} N_{xx} \\ N_{yy} \\ N_{xy} \\ M_{xx} \\ M_{yy} \\ M_{xy} \end{Bmatrix} = \begin{bmatrix} A_{11} & A_{12} & A_{16} & B_{11} & B_{12} & B_{16} \\ A_{12} & A_{22} & A_{26} & B_{12} & B_{22} & B_{26} \\ A_{16} & A_{26} & A_{66} & B_{16} & B_{26} & B_{66} \\ B_{11} & B_{12} & B_{16} & D_{11} & D_{12} & D_{16} \\ B_{12} & B_{22} & B_{26} & D_{12} & D_{22} & D_{26} \\ B_{16} & B_{26} & B_{66} & D_{16} & D_{26} & D_{66} \end{bmatrix} \begin{Bmatrix} \varepsilon_{xx}^0 \\ \varepsilon_{yy}^0 \\ 2\varepsilon_{xy}^0 \\ \kappa_{xx}^b \\ \kappa_{yy}^b \\ \kappa_{xy}^b \end{Bmatrix} \quad (36)$$

$$\begin{Bmatrix} Q_{yz} \\ Q_{xz} \end{Bmatrix} = K \begin{bmatrix} A_{44} & A_{45} \\ A_{45} & A_{55} \end{bmatrix} \begin{Bmatrix} 2\varepsilon_{yz}^0 \\ 2\varepsilon_{xz}^0 \end{Bmatrix}$$

where $K$ is the shear correction factor and $Q_{yz}$ and $Q_{xz}$ are the resultant shear forces [18].

A shear correction factor $K$ is often used to reduce the discrepancy between the actual transverse shear stress state and the assumed constant transverse shear stress state [19]. Essentially, this factor adjusts the transverse shear stiffness.

Note that a Key-Hoff finite element formulation based on Mindlin shell theory [20] was chosen to represent the laminated composites used in the aircraft structure in this study, as transverse shear deformation is important to achieve accurate material response for thick laminates.

**Bending of rectangular laminates**

Consider a rectangular symmetrically laminated composite plate of length *a*, width *b* and total thickness *h* under a uniformly distributed transverse bending load $q(x, y)$ as shown in Figure 14. The plate is constructed of an arbitrary number *N* of orthotropic layers with principal material fibre orientations $\theta_k$, where *k* = 1, 2, …, *N*. The *x*-*y* plane of the Cartesian coordinate system is located at the undeformed mid-plane of the plate.

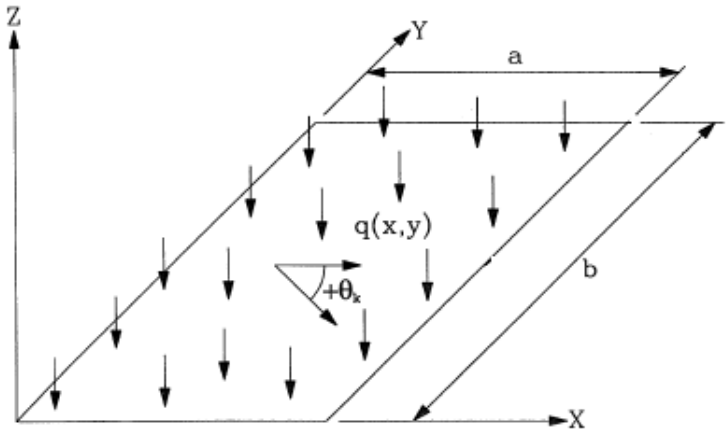


**Figure 14: Geometry and loading of a symmetrically laminated composite plate [21]**

**Mid-surface deflection derived using classical plate lamination theory**

The mid-surface deflection $w$ in the $z$ direction under a transverse bending load $q$ satisfies the following governing differential equation [22]:

$$D_{11}\frac{\partial^4 w}{\partial x^4} + 4D_{16}\frac{\partial^4 w}{\partial x^3 \partial y} + 2(D_{12} + 2D_{66})\frac{\partial^4 w}{\partial x^2 dy^2} + 4D_{26}\frac{\partial^4 w}{\partial x \partial y^3} + D_{22}\frac{\partial^4 w}{\partial y^4} - q = 0 \quad (37)$$

**Mid-surface deflection derived using first-order shear deformation theory**

The equations of motion (expressed in terms of displacements) for a FSDT derived by Thai and Choi [15] are presented below. These equations may also be used to solve for the mid-surface deflection $w$ in the $z$ direction due to a uniformly distributed transverse bending load $q(x, y)$ as shown in Figure 14.

$$A_{11}\frac{\partial^2 u}{\partial x^2}+2A_{16}\frac{\partial^2 u}{\partial x\partial y}+A_{66}\frac{\partial^2 u}{\partial y^2}+A_{16}\frac{\partial^2 v}{\partial x^2}+(A_{12}+A_{66})\frac{\partial^2 v}{\partial x\partial y}+A_{26}\frac{\partial^2 v}{\partial y^2}-\left[B_{11}\frac{\partial^3 w_b}{\partial x^3}+3B_{16}\frac{\partial^3 w_b}{\partial x^2\partial y}+(B_{12}+2B_{66})\frac{\partial^3 w_b}{\partial x\partial y^2}+B_{26}\frac{\partial^3 w_b}{\partial y^3}\right]=I_0\ddot{u} \quad (38)$$

$$A_{16}\frac{\partial^2 u}{\partial x^2}+(A_{12}+A_{66})\frac{\partial^2 u}{\partial x\partial y}+A_{26}\frac{\partial^2 u}{\partial y^2}+A_{66}\frac{\partial^2 v}{\partial x^2}+2A_{26}\frac{\partial^2 v}{\partial x\partial y}+A_{22}\frac{\partial^2 v}{\partial y^2}-\left[B_{16}\frac{\partial^3 w_b}{\partial x^3}+(B_{12}+2B_{66})\frac{\partial^3 w_b}{\partial x^2\partial y}+3B_{26}\frac{\partial^3 w_b}{\partial x\partial y^2}+B_{22}\frac{\partial^3 w_b}{\partial y^3}\right]=I_0\ddot{v}$$

$$B_{11}\frac{\partial^3 u}{\partial x^3}+3B_{16}\frac{\partial^3 u}{\partial x^2\partial y}+(B_{12}+2B_{66})\frac{\partial^2 u}{\partial x\partial y^2}+B_{26}\frac{\partial^3 u}{\partial y^3}+B_{16}\frac{\partial^3 v}{\partial x^3}+(B_{12}+2B_{66})\frac{\partial^3 v}{\partial x^2\partial y}+3B_{26}\frac{\partial^2 v}{\partial x\partial y^2}+B_{22}\frac{\partial^3 v}{\partial y^3}-D_{11}\frac{\partial^4 w_b}{\partial x^4}-4D_{16}\frac{\partial^4 w_b}{\partial x^3\partial y}-2(D_{12}+2D_{66})\frac{\partial^4 w_b}{\partial x^2\partial y^2}-4D_{26}\frac{\partial^4 w_b}{\partial x\partial y^3}-D_{22}\frac{\partial^4 w_b}{\partial y^4}+q=I_0(\ddot{w}_b+\ddot{w}_s)-I_2\nabla^2\ddot{w}_b$$

$$\kappa A_{55}\frac{\partial^2 w_s}{\partial x^2}+\kappa A_{44}\frac{\partial^2 w_s}{\partial y^2}+2\kappa A_{45}\frac{\partial^2 w_s}{\partial x\partial y}+q=I_0(\ddot{w}_b+\ddot{w}_s)$$

where:

$I_0$ and $I_2$ are the mass inertias defined by $(I_0, I_2) = \int_{-h/2}^{h/2}(1, z^2)\rho dz$.

$\rho$ is the mass density of the plate.

The dot-accent convention indicates differentiation with respect to time.

### 1.1.10 Sandwich structures

A sandwich structure consists of a light weight core with face sheets (skins) adhesively bonded both sides of the core as shown in Figure 15. In this discussion, the face sheets are fibre reinforced composite laminates. Sandwich structures are used instead of solid laminates due to their high flexural stiffness-to-weight ratio. Engineering theory has shown that the flexural stiffness (i.e. the modulus of elasticity multiplied by the moment of inertia) of a structure is exponentially proportional to the height of the structure. As an example, for an I-beam manufactured from traditional isotropic engineering materials (e.g. mild steel), the moment of inertia has a cubic relation to the height of the I-beam. The high flexural stiffness in a sandwich structure therefore results from the distance between the face sheets. The low density of the core material results in a light weight structure, with typical core densities in the range of 16 to 480 kilograms per cubic metre [10]. The face sheets carry the flexural loads (compression and tension), whilst the core carries the shear loads. Typical core materials include metallic and non-metallic honeycomb core, balsa wood, open and closed cell foams, and syntactics (matrix such as epoxy filled with hollow spheres such as glass or ceramic micro-balloons). Sandwich structures are extremely structurally efficient, especially in stiffness-critical applications, and are therefore used extensively in aerospace and commercial industries. Honeycomb cores offer higher performance than foam cores; however foam cores are cheaper and easier to work with. This is why foam cores are generally used for commercial applications such as boat and light aircraft construction, and honeycomb cores are used in the aerospace industry.

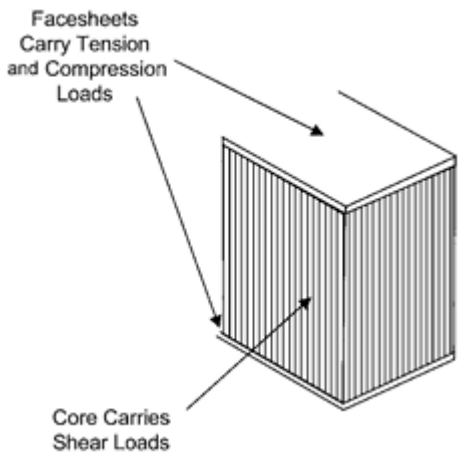


**Figure 15: Sandwich structure [10]**

Honeycomb cores may be considered transversely isotropic materials, whilst foam cores may be considered isotropic materials. The core may be treated as another lamina within the laminate for calculation purposes within lamination theory (e.g. CPLT or FSDT). For example, $E_{11}$ equals $E_{22}$ in an isotropic material, and would be used to define the stress-strain relations. It is noted that crushing of the core is not accounted for in lamination theory due to the assumption that the laminae are in a state of plane stress.

### 1.1.11 Failure theories

The purpose of failure criteria in laminated composites is to define failure envelopes to predict final failure strengths of structures under combined loading conditions. Failure criteria data is generally obtained from relatively simple uniaxial and pure shear experiments because combined stress experiments are difficult to perform, especially when loaded in biaxial compression. Every failure criterion has its strengths and weaknesses; therefore careful consideration of the loading conditions is required when selecting an appropriate failure criterion. Four common failure criteria are discussed, namely Maximum Stress, Tsai-Hill, Tsai-Wu, and Puck. The

discussions are limited to plane-stress conditions and emphasis has been placed on the Tsai-Wu failure criterion due to its implementation in this study.

**Maximum Stress failure criterion**

In the Maximum Stress failure criterion, the principal stresses in each ply are compared with their corresponding strength values. Failure occurs when any stress in the principal material directions is equal to or greater than the corresponding allowable strength. For failure to occur, the Maximum Stress failure criterion must satisfy:

$$\begin{gathered} \sigma_{11} \geq X_T \ (\sigma_{11} > 0) \\ |\sigma_{11}| \geq X_C \ (\sigma_{11} < 0) \\ \sigma_{22} \geq Y_T \ (\sigma_{22} > 0) \\ |\sigma_{22}| \geq Y_C \ (\sigma_{22} < 0) \\ |\sigma_{12}| \geq S \end{gathered} \tag{39}$$

where:

$X_T$ = longitudinal tensile strength
$X_C$ = longitudinal compressive strength
$Y_T$ = transverse tensile strength
$Y_C$ = transverse compressive strength
S = shear strength in the *xy* or 1-2 plane

The failure mode is determined by which part of Equation 39 is satisfied. A disadvantage of the Maximum Stress failure criterion is that it does not account for the interaction of stresses.

**Tsai-Hill failure criterion**

The Tsai-Hill failure criterion considers the interaction of stresses which may lead to failure and is an adaptation of the von Mises yield criterion for isotropic materials. The von Mises yield criterion is modified to account for anisotropy of composite materials; however it does not account for different strengths in tension and compression. In the Tsai-Hill failure criterion, composite failure strengths replace yield strengths typical of isotropic materials. For failure to occur, the Tsai-Hill failure criterion must satisfy:

$$\frac{\sigma_{11}^2}{X^2} - \frac{\sigma_{11}\sigma_{22}}{X^2} + \frac{\sigma_{22}^2}{Y^2} + \frac{\sigma_{12}^2}{S^2} \geq 1 \qquad (40)$$

where:

X = longitudinal strength
Y = transverse strength
S = shear strength in the *xy* or 1-2 plane

The von Mises criterion is based on distortional energy theory and is not applicable to composite materials. The Tsai-Hill failure criterion should therefore be viewed as a curve-fit model rather than a model based on physics. The Tsai-Hill failure criterion is a quadratic criterion and is based on the premise that a second-order curve has more parameters with which to fit experimental data than does a straight line. The Tsai-Hill failure criterion does not indicate failure modes.

**Tsai-Wu failure criterion**

The Tsai-Wu failure criterion was a result of an attempt to mathematically generalise the Tsai-Hill failure criterion creating a curve fit based on tensor theory and accounting for the differences in tensile and compressive

strengths of composite materials [12]. Similar to the Tsai-Hill failure criterion, the Tsai-Wu failure criterion is quadratic, does not indicate failure modes, and should be viewed as a curve-fit model rather than a model based on physics. For failure to occur, the Tsai-Wu failure criterion must satisfy:

$$F_1\sigma_{11} + F_2\sigma_{22} + F_{11}\sigma_{11}^2 + F_{22}\sigma_{22}^2 + 2F_{12}\sigma_{11}\sigma_{22} + F_{66}\sigma_{12}^2 \geq 1 \qquad (41)$$

$$F_1 = \frac{1}{X_T} - \frac{1}{X_C}, \qquad F_2 = \frac{1}{Y_T} - \frac{1}{Y_C}$$

$$F_{11} = \frac{1}{X_T X_C}, \qquad F_{22} = \frac{1}{Y_T Y_C}, \qquad F_{66} = \frac{1}{S^2},$$

$$F_{12}\ by\ biaxial\ test$$

where:

$X_T$ = longitudinal tensile strength
$X_C$ = longitudinal compressive strength
$Y_T$ = transverse tensile strength
$Y_C$ = transverse compressive strength
S = shear strength in the *xy* or 1-2 plane
F = strength parameter

It is difficult to perform testing where failure occurs due to an equally biaxial stress state, as would be required to determine the $F_{12}$ interaction coefficient shown in Equation 41. According to Herakovich [11], the $F_{12}$ interaction coefficient is small and is often assumed to be zero.

At the lamina level, Hinton et al. [23] show that the Tsai-Wu failure criterion is the most favourable criterion for predicting the strength of unidirectional laminae under biaxial loading. Overall, the Tsai-Wu failure criterion has the

ability to predict biaxial failure stresses to within 10 percent of experimental results; however the results must be viewed with caution in the compression-compression quadrant. Figure 16 shows that the Tsai-Wu failure criterion predicts much greater strengths in the compression-compression quadrant when compared to alternative failure criteria, although no experimental data is available for this quadrant to confirm the accuracy of the Tsai-Wu failure criterion.

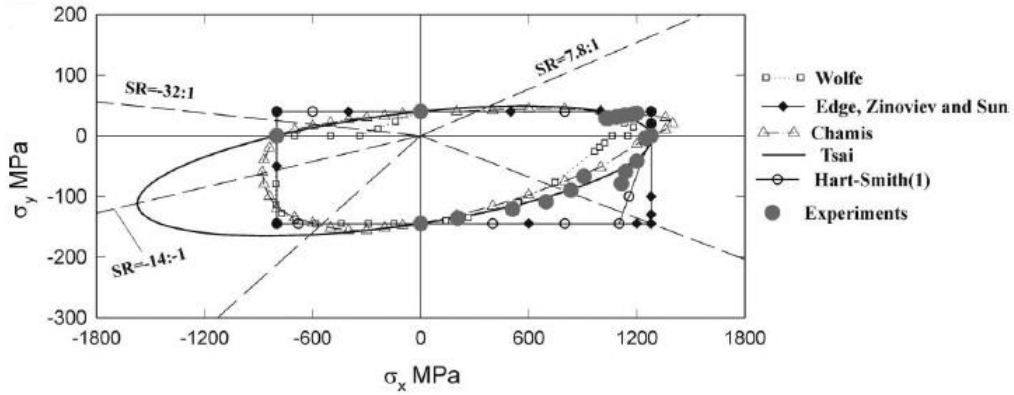


**Figure 16: Comparison between the predicted and measured biaxial failure envelope of $0^o$ GRP lamina under combined $\sigma_x$ and $\sigma_y$ stresses. Material: E-glass/MY750 epoxy [23]**

Multi-directional laminates subjected to various loading conditions may still have a load carrying capacity beyond first-ply failure. The Tsai-Wu failure criterion employs a degradation model where the material properties (i.e. stiffness coefficients) of the failed lamina are suddenly reduced. If loading continues to increase beyond first-ply-failure, progressive ply failure occurs until last-ply-failure is reached.

Laminates with quasi-isotropic layups are commonly used in the aerospace industry, since some of the fibres will likely be closely aligned with loading directions. This layup arrangement is also assumed for large portions of the aircraft presented in this study; therefore a comparison between the predicted and experimental biaxial last-ply failure stresses for quasi-isotropic

layups of AS4/3501-6 laminates is shown in Figure 17 to investigate the performance of the Tsai-Wu failure criterion. The Tsai-Wu failure envelope is not smooth because at certain combined stresses, predicted last-ply failure may jump from one ply orientation to another [24]. As shown in Figure 17, reasonably conservative results were achieved with the Tsai-Wu failure criterion for predicting the final strength of multidirectional laminates; however largely over-predicted final laminate strength under compression-compression biaxial loading when compared to alternative failure theories. The over-predicted final laminate strength results from the over-predicted unidirectional laminae strength under biaxial compression as shown in Figure 16. There is a lack of definitive experimental data in the compression-compression quadrant; therefore it is not possible to confirm the accuracy of the Tsai-Wu failure criterion in this quadrant; however the results should be viewed with caution. Hinton et al. [23] also believe that shell buckling influenced the experimental data in the compression-compression quadrant, resulting in lower ultimate strengths than anticipated. Overall, according to Hinton et al. [23], the Tsai-Wu failure criterion has the ability to predict the biaxial failure stresses of multi-directional laminates to within 50 percent of experimental results for the majority of combined biaxial loadings, resulting in a favourable ranking when compared to the majority of alternative failure criteria.

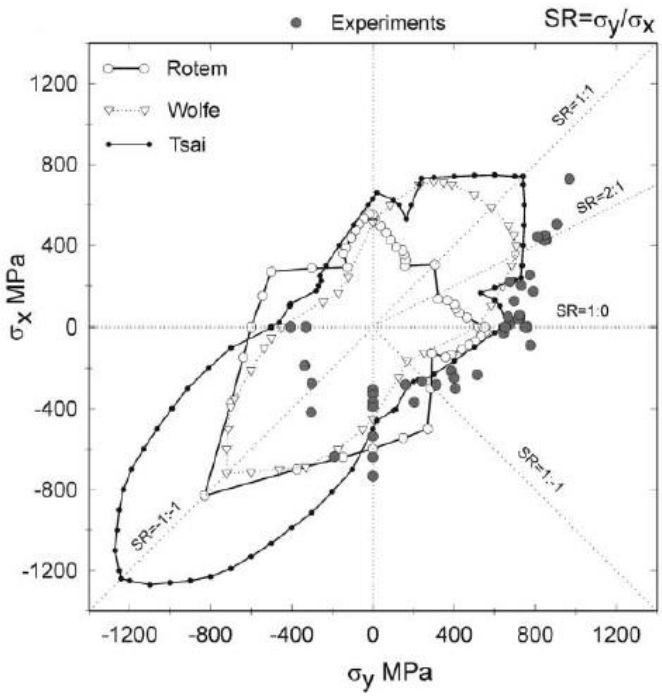


**Figure 17: Comparison between the predicted and measured biaxial last-ply failure stresses for $[0^o/\pm45^o/90^o]_s$ AS4/3501-6 laminates [23]**

The Tsai-Wu failure criterion predicts the entire shape of stress-strain curves reasonably well for fibre-dominated cases such as quasi-isotropic laminates as shown in Figure 18 and Figure 19. The Tsai-Wu failure criterion, like many alternative criteria considered, has been shown to perform poorly in predicting laminate deformation where shear stresses and matrix behaviour have a significant effect in the failure process, and where large deformations are present before final failure as may be the case for angle-ply laminates such as that shown in Figure 20. In general, the Tsai-Wu failure criterion accurately predicts the deformation of laminates at low strains. At moderate strains, the Tsai-Wu theory may underestimate measured strains and over-estimate stiffness as a result of assumed linear elastic material behaviour.

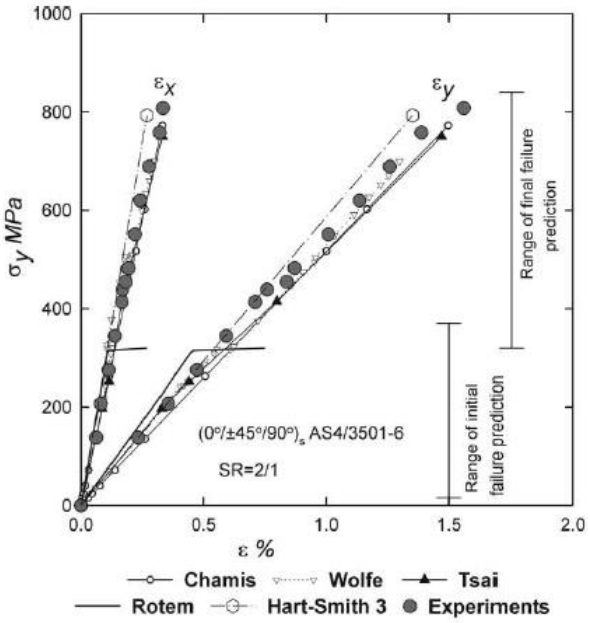


**Figure 18: Comparison between the predicted and measured stress-strain curves for $[0^o/\pm45^o/90^o]_s$ AS4/3501-6 laminates under biaxial stress ($\sigma_y/\sigma_x$ = 2/1) [23]**

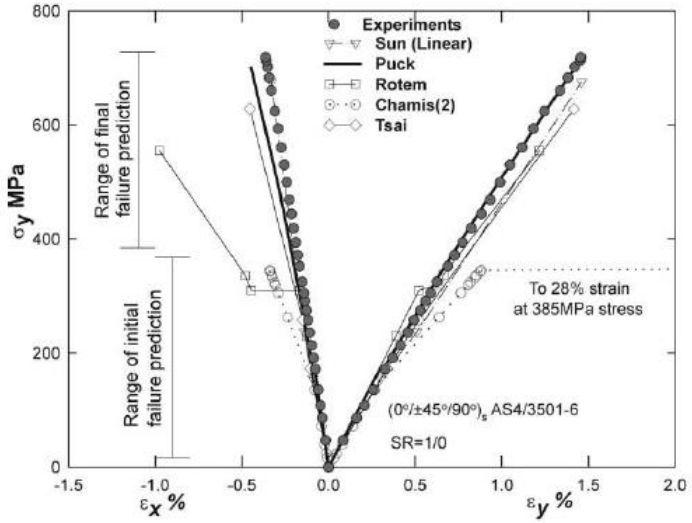


**Figure 19: Comparison between the predicted and measured stress-strain curves for $[0^o/\pm45^o/90^o]_s$ AS4/3501-6 laminates under uniaxial tension ($\sigma_y/\sigma_x$ = 1/0) [23]**

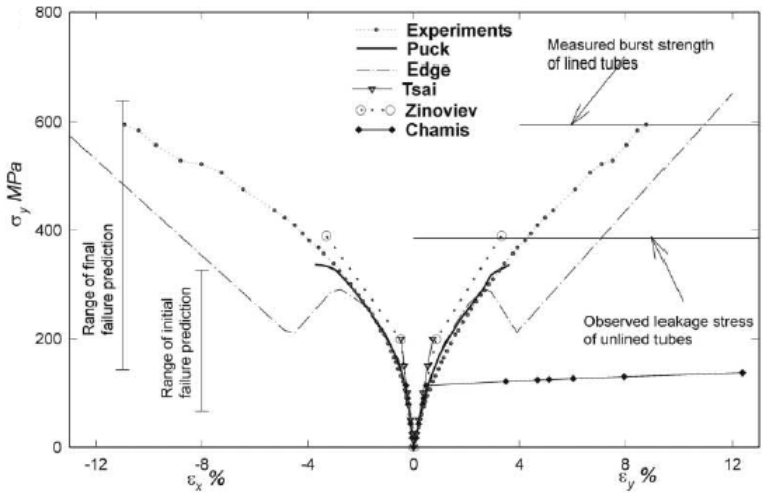


**Figure 20: Comparison between the predicted and measured stress-strain curves for $[\pm 55^{o}]_{s}$ E-glass/MY750 laminates under uniaxial tension ($\sigma_y/\sigma_x$ = 1/0) [23]**

**Puck failure criterion**

The Puck failure criterion is a physically based phenomenological model. It consists of five failure modes, two for fibre failure (tensile and compressive), and three for matrix failure (denoted as A, B and C) [25]. The three matrix failure modes are shown in Figure 21. The calculations for fibre failure were born from the assumption that fibre failure in a unidirectional composite under a combined state of stress will occur at the same fibre stress as that which is acting in the fibres at failure under a uniaxial stress $\sigma_1$. For matrix (inter-fibre) failure, the calculations were born from Mohr's hypothesis for brittle materials where fracture is exclusively created by the stresses which act on the fracture plane. Due to the brittle nature of composites, a failure criterion based on Mohr appears to be much more appropriate for the analysis of composites when compared to that of Tsai-Hill and Tsai-Wu. Tsai-Hill and Tsai-Wu adapted their work from von Mises, which was originally developed for ductile materials. Further details of the Puck failure criterion may be found in reference [26].

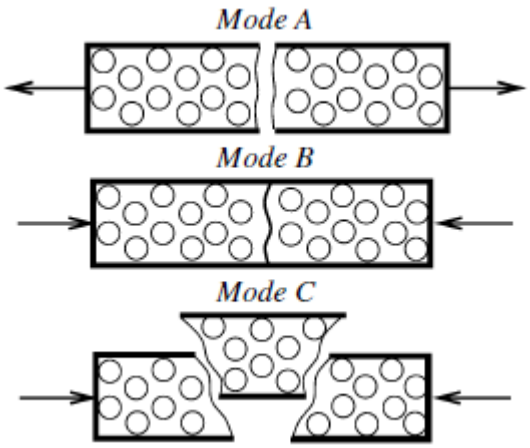


**Figure 21: Mechanisms causing matrix failure [25]**

## 1.2 The finite element method

### 1.2.1 Introduction

This section aims to introduce the basic fundamental concepts of the finite element method (FEM) and the associated terminology. The FEM was only used as an engineering tool in this study, therefore an in depth discussion of the FEM is avoided. The FEM is a numerical analysis technique for obtaining approximate solutions to a wide variety of engineering problems [27]. For example, in the context of structural analysis, the FEM is used to calculate the deformations, stresses and strains of complex structures where conventional methods are impractical. The FEM is based on the concept of discretisation where the body of interest (domain) is subdivided into a number of smaller regions called finite elements (subdomains). The collection of non-overlapping and interconnected finite elements is referred to as the finite element mesh of the domain. The element vertices are called nodal points (or nodes); however additional nodal points, such as boundary and internal nodal points, may exist in an element. The discretisation process involves approximation; therefore the solution obtained is not exact but rather

an approximation of the exact solution. For example, the area of a circle is approximated by the use of a finite number of polygons (elements) as shown in Figure 22. As can be seen, by increasing the amount of polygons, accuracy is increased; however computational time is increased due to an increase in calculations. This process of successively moving towards an exact solution is termed convergence.

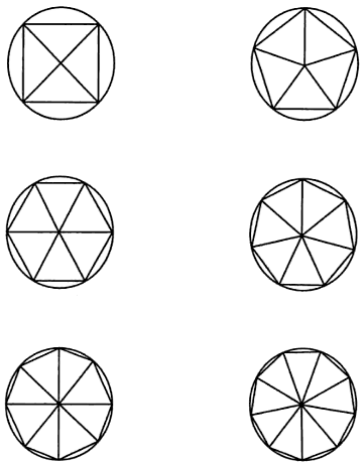

**Figure 22: Discretisation of a circle [28]**

In the FEM, we seek an approximate solution to the governing (partial) differential equation over each finite element, subject to appropriate boundary conditions. For example, the governing differential equation for two-dimensional problems may typically be described by a second-order partial differential equation as [29]:

$$-\left[\frac{\partial}{\partial x}\left(a_{xx}\frac{\partial \phi}{\partial x}\right)+\frac{\partial}{\partial y}\left(a_{yy}\frac{\partial \phi}{\partial y}\right)\right]=f(x,y)\ in\ \Omega \tag{42}$$

where: $\Omega$ is a two-dimensional domain with boundary $\Gamma$; $a_{xx}$ and $a_{yy}$ are material coefficients in the $x$ and $y$ directions, respectively; $f(x,y)$ is the known source; and $\phi$ is the solution to be determined (i.e. the unknown field variable).

The finite element discretisation procedures reduce the continuum problem to one of a finite number of unknowns by dividing the solution domain into elements and by expressing the unknown field variable (i.e. solution to be determined) in terms of assumed approximating functions (also referred to as interpolation functions) within each element. Once the elements and their interpolation functions have been selected, one of three approaches may be used to determine the matrix equations expressing the properties of the individual elements (i.e. equations governing element behaviour); namely the direct approach, the variational approach, or the weighted residual approach [27]. The resulting element equation may be expressed in matrix form as:

$$[K]^{(e)}\{\phi\}^{(e)} = \{F\}^{(e)} \tag{43}$$

where: $[K]^{(e)}$ is the element property matrix (stiffness matrix); $\{\phi\}^{(e)}$ is the vector of unknown field variables at the element nodal points (e.g. vector of nodal displacements); and $\{F\}^{(e)}$ is the vector of nodal forcing parameters (e.g. vector of nodal forces).

The matrix equations for the individual elements are combined (i.e. assembled) to form the matrix equations expressing the behaviour of the entire system. Shared nodal points result in an assembly of elements into a global system of equations. The assembling process is based on the law of compatibility or continuity, which requires that a body remains continuous. In other words, the displacements of two adjacent nodal points must be identical. Depending on the problem, additional continuity conditions may be required. For example, bending problems require continuity of displacements and continuity of the first derivative of displacements (slopes) at adjacent nodes. $C^n$ continuity refers to continuity of the $n^{th}$ derivatives of equations. Thus, $C^0$ continuity refers to continuity of the zero$^{th}$ derivative of displacement, $C^1$ continuity refers to continuity of the first derivative of

displacement (in addition to $C^0$ continuity), and so on. The global system of equations is expressed as:

$$[K]\{\phi\} = \{F\} \tag{44}$$

where: $[K]$ is the global property matrix (global stiffness matrix); $\{\phi\}$ is the global vector of unknown field variables (e.g. nodal displacement vector); and $\{F\}$ is the global vector of nodal forcing parameters (e.g. nodal load vector).

The global system matrices may be obtained by simple addition of the element matrices within the global system matrices in the appropriate locations (note that the global system matrices have the same form as the equations for the individual elements except that they contain many more terms because they include all nodal points).

Boundary conditions are physical constraints or supports that must exist so that a structure can stand in space uniquely. The boundary conditions are specified at this stage as known nodal values of the unknowns. The numbers of unknowns or degrees of freedom are dependent on the problem at hand. In the context of structural analysis, a degree of freedom may be defined as an independent (unknown) displacement that can occur at a point [28]. For example, if a nodal point is free to translate in the x and y directions only (as is the case for plane deformation), it has two degrees of freedom. A triangular element with three nodal points under plane deformation has a total of six degrees of freedom (i.e. two degrees of freedom at each nodal point).

The system equations may now be solved to obtain the unknown nodal values. A set of linear or nonlinear algebraic equations must be solved for problems describing steady or equilibrium behaviour. Standard solution techniques such as Gaussian elimination (direct method) and Newton-Raphson (iteration method) may be used to solve the linear and nonlinear algebraic equations, respectively. A set of linear or nonlinear ordinary

differential equations must be solved for unsteady problems where the nodal values are a function of time. A popular general procedure for solving the time-dependent equations is known as mode superposition; alternatively recurrence relations may be used, which permits a time-stepping (or time-marching) solution [27]. Once the nodal unknowns (primary unknowns such as displacement) have been solved for, secondary quantities (such as strains, stresses, moments, shear forces) may then be determined from the primary unknowns.

### 1.2.2 Elements and interpolation functions

#### Basic element types

There are many types of elements available for use in finite element analysis (FEA). Some of the basic element types are shown in Figure 23. In the context of structural analysis, the choice of element generally depends on the load and deformation characteristics of the actual structure that the finite element model represents. The discussions that follow will focus on the four-node $C^o$-linear quadrilateral shell element due to its application in the Key-Hoff finite element formulation as discussed in Chapter 1 Section 2.6.

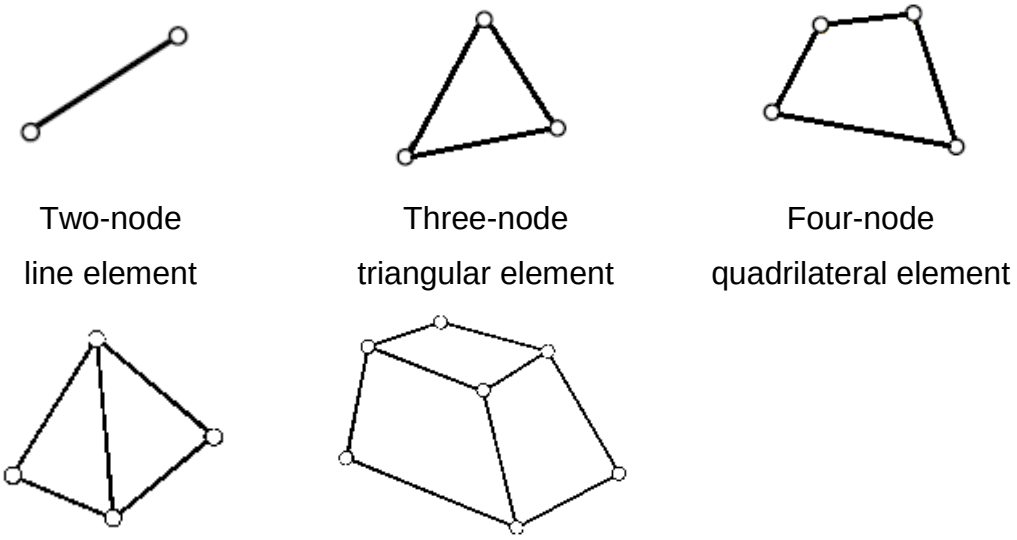


**Figure 23: Basic element types**

Shell elements are two-dimensional and are used to model thin structures where the thickness is small compared to the length. Commonly used triangular and quadrilateral shell elements consist of three and four nodal points respectively. Shell elements may support in-plane and bending loads. Transverse shear stiffness may also be accounted for. Triangular shell elements may exhibit excessive stiffness and are commonly used in mesh transition zones and for filling in irregular boundaries. The use of triangular shell elements should be avoided around areas of interest.

**Interpolation functions**

Interpolation functions represent the behaviour of the solution within an element. The polynomial type of interpolation functions are most commonly used as: (i) it is relatively easy to perform differentiation or integration with polynomials to formulate and computerise the finite element equations; and (ii) the accuracy of results can be improved by increasing the order of the polynomial. Figure 24 shows polynomial approximations in one dimension

and how the accuracy of results can be improved by increasing the order of the polynomial. Elements with interpolation polynomials of order one are termed “linear elements”, whereas for orders of two or more, the elements are referred to as “higher order elements” [30].

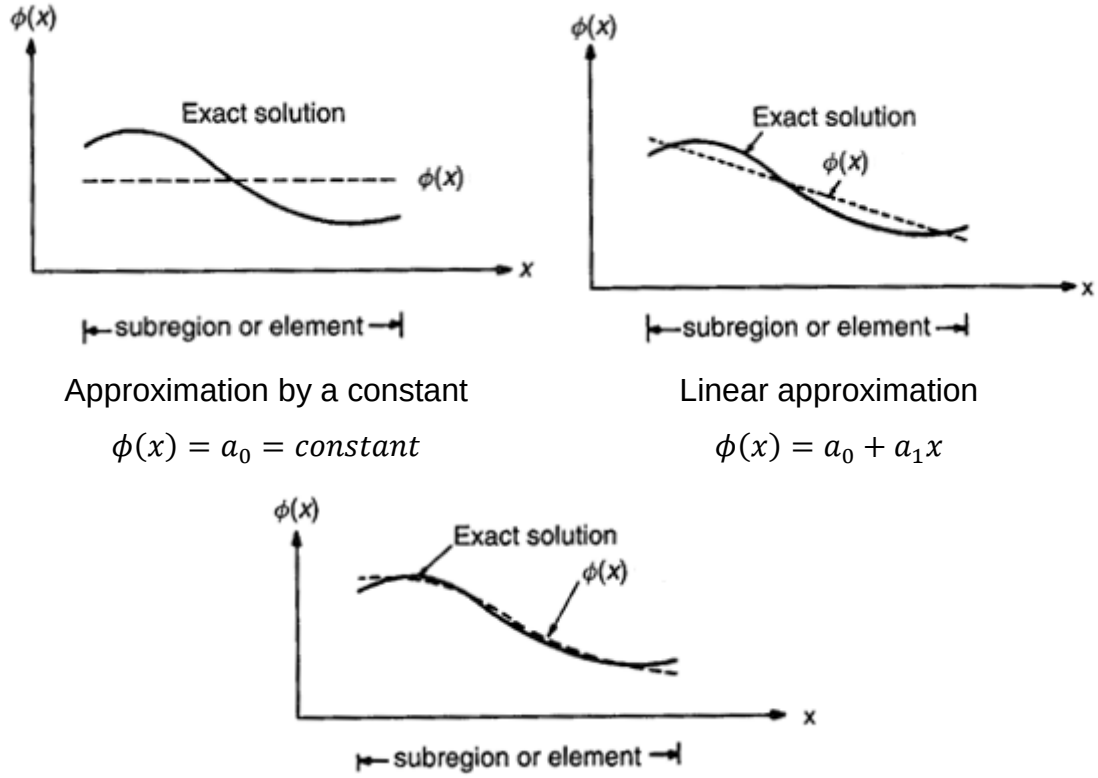


Approximation by a constant

$\phi(x) = a_0 = constant$

Linear approximation

$\phi(x) = a_0 + a_1 x$

Quadratic approximation

$\phi(x) = a_0 + a_1 x + a_2 x^2$

**Figure 24: Polynomial approximation in one dimension [30]**

The four-node $C^o$-linear quadrilateral element only requires continuity of the field variable $\phi$ at the element interfaces and will be discussed in the text that follows.

For a domain $\Omega$ consisting of $M$ number of elements, the finite element approximation of the dependent unknown field variable $\phi$ may be

approximated over a typical finite element domain $\Omega^e$ with the use of polynomial interpolation functions as [27, 29]:

$$\phi \approx \sum_{e=1}^{M} \phi^{(e)} = \sum_{e=1}^{M} \left[N^{(e)}\right]\{\phi\}^{(e)}, e = 1, 2, \dots, M \tag{45}$$

where for $n$ number of nodal points:

$$\phi^{(e)} = \left[N^{(e)}\right]\{\phi\}^{(e)} = \sum_{i=1}^{n} N_i \phi_i, i = 1, 2, \dots, n \tag{46}$$

$[N^e]$ are the interpolation functions, which are functions of the coordinates of the nodal points; and $\phi^e$ represents an approximation of $\phi$ over the element domain.

The interpolation functions are defined in terms of the values of the field variables at the nodal points, such that $N_i$ has a value of one at node $i$ and zero at all other nodes [31]. In order to satisfy certain compatibility conditions, interpolation functions are chosen so that the field variable or its derivatives are continuous across adjoining element boundaries. The selection of interpolation functions are applied to the formulation of various types of elements [27].

Methods for deriving interpolation functions often rely on the use of natural coordinates, which is a local coordinate system reliant on the element geometry for its definition with coordinates ranging between zero and unity within the element. Other methods for deriving interpolation functions include classical interpolation polynomials such as Lagrange polynomials and Hermite polynomials, which will not be discussed. Natural coordinate systems basically describe the location of a point inside an element in terms of coordinates associated with the nodal points of the element [27].

**The four-node $C^o$-linear quadrilateral element**

Figure 25 shows a “master element” (regular) in a natural (local) coordinate system ($\xi, \eta$ space) and also shows the master element mapped onto a “real element” (irregular) in a Cartesian (global) coordinate system ($x, y$ space). The use of natural coordinates allows for the use of identical interpolation functions for each four-node $C^o$-linear quadrilateral element. The master element is chosen to be a bi-unit square, rather than unit, for convenience in later applying the Gauss quadrature, which integrates from -1 to +1 [32]. The master elements, for which interpolation functions are developed, can be used for numerical evaluation of integrals on real elements. This requires a transformation of the geometry from the actual element shape to an associated master element [32]. Real elements may have arbitrary corner angles and side lengths within allowable distortion limits; however the sides must be straight. It is recommended that interior corner angles stay within approximately 20 or 30 degrees of a right angle, whilst the aspect ratio of the element side lengths be limited to approximately 5:1 or 10:1 depending on the problem [32].

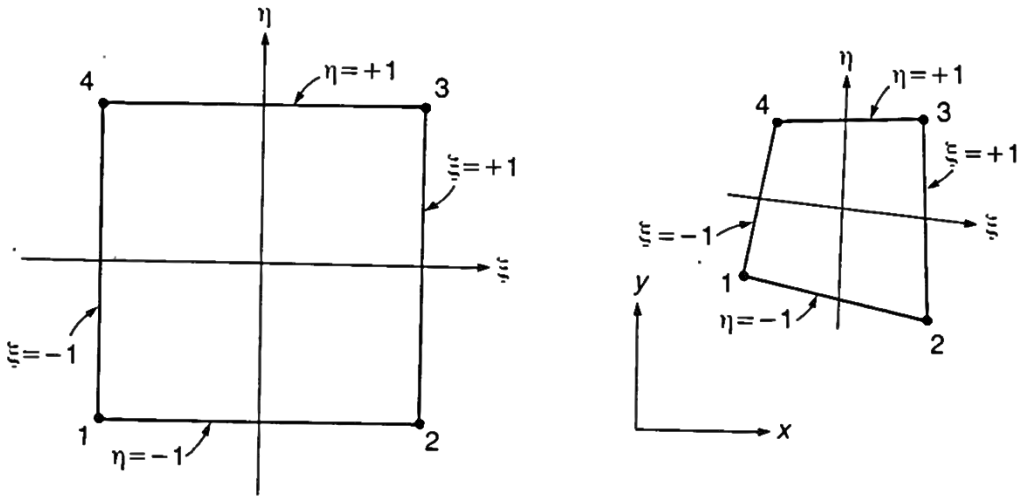


Master element

Real element with master element mapped onto it

**Figure 25: Master and real elements for the four-node C$^o$-linear quadrilateral element [32]**

The natural and Cartesian coordinates are related by the following equation [30]:

$$\begin{Bmatrix} x \\ y \end{Bmatrix} = \begin{bmatrix} N_1 & N_2 & N_3 & N_4 & 0 & 0 & 0 & 0 \\ 0 & 0 & 0 & 0 & N_1 & N_2 & N_3 & N_4 \end{bmatrix} \cdot \begin{Bmatrix} x_1 \\ x_2 \\ x_3 \\ x_4 \\ y_1 \\ y_2 \\ y_3 \\ y_4 \end{Bmatrix} \tag{47}$$

where $(x_i, y_i)$ are the $(x, y)$ coordinates of node $i$ $(i = 1, 2, 3, 4)$, and the bilinear interpolation functions are:

$$N_i = \frac{1}{4}(1 + \xi\xi_i)(1 + \eta\eta_i); i = 1, 2, 3, 4 \tag{48}$$

The natural coordinates of the quadrilateral element are given by:

$$(\xi_1, \eta_1) = (-1, -1), \qquad (\xi_2, \eta_2) = (1, -1), \qquad (\xi_3, \eta_3) = (1, 1), \qquad (\xi_4, \eta_4) = (-1, 1) \tag{49}$$

If the field variable is a function of the natural coordinates, its derivatives with respect to $x$ and $y$ can be found as:

$$\begin{Bmatrix} \frac{\partial \phi}{\partial x} \\ \frac{\partial \phi}{\partial y} \end{Bmatrix} = [J]^{-1} \begin{Bmatrix} \frac{\partial \phi}{\partial \xi} \\ \frac{\partial \phi}{\partial \eta} \end{Bmatrix} \tag{50}$$

where $[J]$ is the Jacobian matrix of the transformation given by:

$$[J] = \begin{bmatrix} \frac{\partial x}{\partial \xi} & \frac{\partial y}{\partial \xi} \\ \frac{\partial x}{\partial \eta} & \frac{\partial y}{\partial \eta} \end{bmatrix} \tag{51}$$

$$[J] = \frac{1}{4} \begin{bmatrix} -(1-\eta) & (1-\eta) & (1+\eta) & -(1+\eta) \\ -(1-\xi) & -(1+\xi) & (1+\xi) & (1-\xi) \end{bmatrix} \cdot \begin{bmatrix} x_1 & y_1 \\ x_2 & y_2 \\ x_3 & y_3 \\ x_4 & y_4 \end{bmatrix}$$

For a linear quadrilateral element, the interpolation model is taken as:

$$\phi^{(e)}(x, y) = [N]^{(e)} \{\phi\}^{(e)} = [N_1 \quad N_2 \quad N_3 \quad N_4] \{\phi\}^{(e)} \tag{52}$$

where $N_i$ $(i = 1, 2, 3, 4)$ is according to Equation 48 and the vector of nodal values of the field variable of element $e$ is:

$$\{\phi\}^{(e)} = \begin{Bmatrix}\phi_1\\ \phi_2\\ \phi_3\\ \phi_4\end{Bmatrix}^{(e)} = \begin{Bmatrix}\phi(x_1,y_1)\\ \phi(x_2,y_2)\\ \phi(x_3,y_3)\\ \phi(x_4,y_4)\end{Bmatrix}^{(e)} \equiv \begin{Bmatrix}\phi(at\ \xi=-1,\eta=-1)\\ \phi(at\ \xi=1,\eta=-1)\\ \phi(at\ \xi=1,\eta=1)\\ \phi(at\ \xi=-1,\eta=1)\end{Bmatrix}^{(e)} \quad (53)$$

The first two nodal shape functions for a linear four-node quadrilateral element are shown in Figure 26. As can be seen, the shape functions are linear along each side of the element. This ensures $C^o$ continuity between elements since there are two nodes on a side, which uniquely determine a straight line [32].

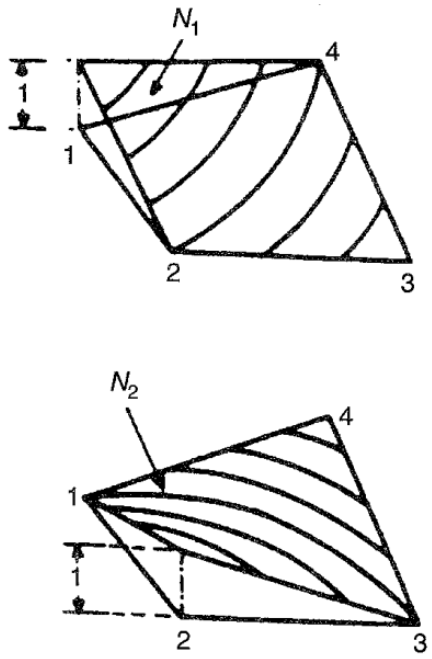


**Figure 26: Linear interpolation functions for a four-node quadrilateral element where $N_1 = \frac{1}{4}(1-\xi)(1-\eta)$; $N_2 = \frac{1}{4}(1+\xi)(1-\eta)$**

**Rigid body elements**

A rigid body element (RBE) is not strictly a finite element. Rather, it describes a displacement relationship between two or more nodal points. It defines a rigid body whose independent degrees of freedom are specified at a single

nodal point and whose dependent degrees of freedom are specified at an arbitrary number of nodal points. In other words, it allows particular degrees of freedom to be coupled so that the nodal points always translate and or rotate the same amount. It must be noted that RBEs cannot fail.

### 1.2.3 Convergence

Convergence of the finite element solutions by increasing the number of elements within the domain is termed h-convergence. Convergence of the solution may also be obtained by increasing the order of interpolation polynomials, which is termed p-convergence [33]. Since the order of the interpolation polynomials remains fixed in this study, only h-convergence is of concern.

In order for the approximate solution to converge to the true solution, the following conditions must be satisfied over an element domain: (i) $\phi^{(e)}(x, y)$ must be continuous; (ii) the polynomials used to represent $\phi^{(e)}(x, y)$ must be complete (i.e. all terms beginning with a constant term up to the highest order used in the polynomial should be included in the expression $\phi^{(e)}(x, y)$); and (iii) all terms in the polynomial should be linearly independent, where the number of linearly independent terms dictates the shape and number of degrees of freedom of the element [29].

### 1.2.4 Numerical integration

The exact evaluation of the definite integrals appearing in the element property matrices and vector of unknown field variables is not always possible due to the complexity of the differential equations. Additionally, the definite integrals need to be replaced by a numerical equivalent suitable to computers. Numerical integration, also referred to as numerical quadrature,

aims to find a suitable function $P(x)$ that is both a suitable approximation of $R(x)$ and simple to integrate. Interpolating polynomials of order $n$, denoted by $P_n$, which interpolate the integrand at $n+1$ points in the interval $[a, b]$, often satisfies these aims [33].

Several schemes exist for the numerical evaluation of definite integrals, such as the commonly used Newton-Cotes quadrature and Gauss quadrature. The Gauss quadrature is more frequently used than the Newton-Cotes quadrature because it requires fewer base (sampling) points to achieve the same accuracy, therefore increasing computational efficiency [33].

### 1.2.5 Dynamic analysis

In this section, the FEM of time-dependent propagation problems is considered. For example, it may be necessary to evaluate how the stresses and deflections propagate through a structure subjected to time-dependent loading. For the equations that follow, a slightly different notation is used where the brackets have been omitted for matrices and the accent notation for the field variables is replaced for simplification purposes. The dynamic finite element formulation is based on the dynamic equilibrium equation of motion, expressed as [27, 34]:

$$Ma_n + Cv_n + Ku_n = F_n^{ext} \tag{54}$$

where:

$M$ = mass matrix (represents the system inertia)
$C$ = damping matrix
$K$ = stiffness matrix
$F_n^{ext}$ = externally applied load vector (time dependent)

$a$ = vector of the second derivative of the field variables at the nodal points (e.g. acceleration)
$v$ = vector of the first derivative of the field variables at the nodal points (e.g. velocity)
$u$ = vector of field variables at the nodal points (e.g. displacement)
Subscript $n$ = iteration (or step) number

The above second-order differential equation expresses the dynamic equilibrium condition at the instant of time $t$, which may be rewritten as:

$$Ma_n = F_n^{ext} - F_n^{int} \tag{55}$$
$$\therefore a_n = M^{-1}F_n^{residual}\ (Newton's\ Second\ Law)$$

where:

$F_n^{int}$ = vector of internal loads = $Cv_n + Ku_n$
$F_n^{residual}$ = residual load vector = $F_n^{ext} - F_n^{int}$

Solution of the dynamic equilibrium equation is achieved through direct integration of the dynamic equilibrium equation with the use of either implicit (traditional finite element approach) or explicit time integration schemes. Explicit finite element codes have been extensively employed in nonlinear transient dynamic analyses. MSC Dytran, an explicit finite element code, is used for crashworthiness analyses in this study due to the computational efficiency it offers relative to implicit finite element codes in nonlinear transient dynamic events. Typical applications of such events are explosions and high speed impacts such as automobile and aircraft crashworthiness. Details of the explicit method are therefore discussed in this study.

In the explicit method, the acceleration can be calculated explicitly with information available at time $t_n$ in the form of Newton's Second Law as

shown in Equation 55. If the mass matrix $M$ is made diagonal (termed lumped mass matrix), its inversion is trivial, and the system of equations decouples. Formation of lumped mass matrices assumes that element mass and damping characteristics are concentrated at the nodal points [27]. Its overall solution can then be performed independently and quickly for each degree of freedom (subscript $i$) as follows:

$$a_{ni} = F_{ni}^{residual}/M_i \tag{56}$$

The central difference method is used to advance in time, with the assumption that acceleration is constant during a particular time increment $\Delta t$ (also referred to as time step, where $t_{n+1} - t_n = \Delta t$). The velocity is calculated at time $n + \frac{1}{2}$ and the nodal positions (or displacements) are calculated at time $n + 1$ as shown:

$$v_{n+1/2} = v_{n-1/2} + a_n\left(\Delta t_{n+1/2} + \Delta t_{n-1/2}\right)/2 \tag{57}$$

$$u_{n+1} = u_n + v_{n+1/2}\Delta t_{n+1/2} \tag{58}$$

The incremental deformation results in increments of strain and stress, therefore internal forces may be obtained. The external force at time $t_{n+1}$ is calculated by the prescribed loading conditions, and the acceleration at time $t_{n+1}$ is subsequently calculated. The steps involved in the explicit method are repeated for each time increment as shown in Figure 27.

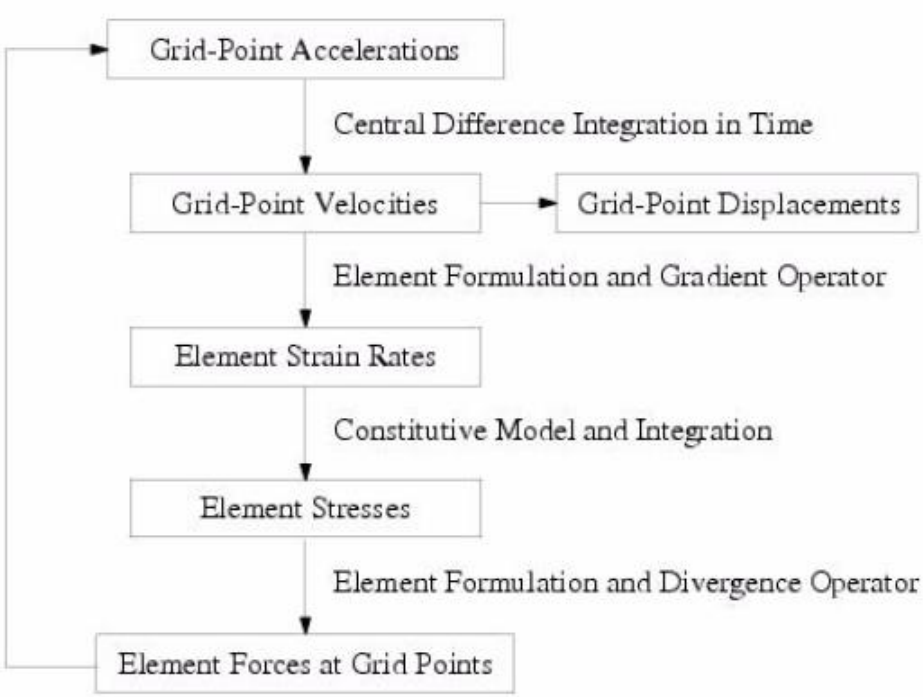


**Figure 27: Flow diagram illustrating a typical loop carried out for each time increment using the explicit method [34]**

Stability of the central difference method requires that the time increment $\Delta t$ must be less than the time taken for a stress wave to propagate through the smallest element in the mesh. Explicit methods are therefore stable whenever the size of the time increment $\Delta t$ is smaller than or equal to a critical time increment $\Delta t_{cr}$ satisfying [34]:

$$\Delta t \leq \Delta t_{cr} = \frac{L_e}{c_e} \tag{59}$$

where:

$L_e$ = smallest element dimension (smallest distance between nodes)

$c_e = \sqrt{\frac{E}{\rho}}$ = speed of sound

$E$ = Elastic modulus

$\rho$ = density

The explicit method is therefore conditionally stable. If the time increment is larger than the critical time increment, the response may become unstable and the computed field variable (e.g. displacement) values will grow without bound as time increases.

### 1.2.6 Finite element formulations for explicit transient dynamics

Finite elements used for explicit transient dynamics are required to be computationally efficient whilst retaining an essential representation of the physical behaviour of the domain. The Belytschko-Lin-Tsay (BLT) shell element is a popular finite element formulation and algorithm employing explicit time integration for the nonlinear dynamic analysis of impulsively loaded shells. Its popularity is mainly attributed to its computational efficiency. The BLT algorithm uses a four-node $C^0$-linear quadrilateral shell element with bilinear interpolation functions, single-point (in-plane) quadrature, and hourglass control. For the discussions that follow, the work performed by Belytschko et al. [35] is discussed and similar notation followed.

The reference surface (i.e. the mid-surface) of the shell element is defined by the location of the four corner nodal points, with coordinates $x^m$, $y^m$ and $z^m$. Orthogonal unit vectors $e_1$, $e_2$, and $e_3$ are defined as a reference frame for each element. The vectors $e_1$ and $e_2$ are tangent to the reference surface, whilst $e_3$ is normal to the reference surface. The vectors are termed co-rotational as they rotate with the material, except that $e_1$ and $e_2$ remain tangent to the reference surface. Figure 28 shows the element coordinate system used for the BLT shell element, where the superscript caret (^) indicates the component of a tensor expressed in terms of the base vector $e_i$.

For further information regarding the construction of the element coordinate system, refer to references [35, 36].

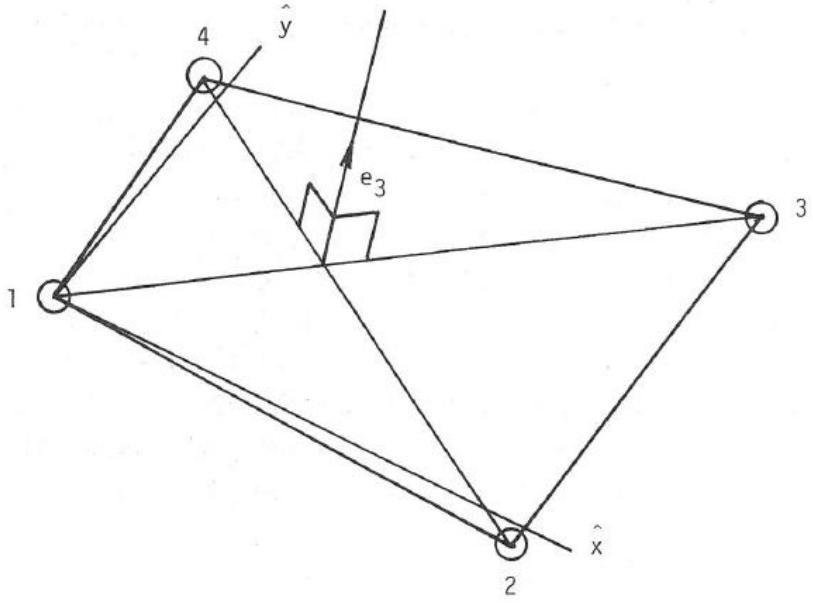


**Figure 28: BLT shell element coordinate system [35]**

The BLT shell element is based on Mindlin theory of plates and shells (first-order shear deformable theory). In this theory, the velocity of a point in the shell is defined by the velocity of the reference surface and the angular velocity by [35, 36]:

$$v = v^m - \hat{z}e_3 \times \theta \tag{60}$$

where:

$v$ = velocity vector

$\theta$ = angular velocity vector

$\hat{z}$ = distance along the fibre direction (thickness) of the shell element

The superscript $m$ refers to the mid-surface (reference surface).

The co-rotational components of the velocity-strain (rate of deformation) $d$ are given by [35]:

$$\hat{d}_{ij} = \frac{1}{2}\left(\frac{\partial \hat{v}_i}{\partial \hat{x}_j} + \frac{\partial \hat{v}_j}{\partial \hat{x}_i}\right) \tag{61}$$

Substitution of Equation 60 into Equation 61 results in the following equations for velocity-strain [35, 36]:

$$\begin{aligned}
\hat{d}_x &= \frac{\partial \hat{v}_x^m}{\partial \hat{x}} + \hat{z}\frac{\partial \hat{\theta}_y}{\partial \hat{x}} \\
\hat{d}_y &= \frac{\partial \hat{v}_y^m}{\partial \hat{y}} - \hat{z}\frac{\partial \hat{\theta}_x}{\partial \hat{y}} \\
2\hat{d}_{xy} &= \frac{\partial \hat{v}_x^m}{\partial \hat{y}} + \frac{\partial \hat{v}_y^m}{\partial \hat{x}} + \hat{z}\left(\frac{\partial \hat{\theta}_y}{\partial \hat{y}} - \frac{\partial \hat{\theta}_x}{\partial \hat{x}}\right) \\
2\hat{d}_{yz} &= \frac{\partial \hat{v}_z^m}{\partial \hat{y}} - \hat{\theta}_x \\
2\hat{d}_{xz} &= \frac{\partial \hat{v}_z^m}{\partial \hat{x}} + \hat{\theta}_y
\end{aligned} \tag{62}$$

Using a co-rotational velocity-strain formulation, the BLT algorithm is directly applicable to anisotropic materials without any corrections for frame invariance of material property tensors as the coordinate system rotates with the material.

Bilinear interpolation functions are used to approximate the coordinates, velocity, and angular velocity of the reference surface by [35, 36]:

$$\begin{aligned}
x^m &= N_I(\xi,\eta)x_I \\
\theta^m &= N_I(\xi,\eta)\theta_I \\
v^m &= N_I(\xi,\eta)v_I
\end{aligned} \tag{63}$$

where the subscript $I$ pertains to the nodal points of the element and when repeated, is summed over the nodal points of the element. The nodal point velocities are obtained by differentiation of the nodal point coordinates with respect to time. The bilinear interpolation functions are [35, 36]:

$$N_1 = \frac{1}{4}(1-\xi)(1-\eta);\ N_2 = \frac{1}{4}(1+\xi)(1-\eta)$$
$$N_3 = \frac{1}{4}(1+\xi)(1+\eta);\ N_4 = \frac{1}{4}(1-\xi)(1+\eta) \tag{64}$$

Through substitution of Equation 63 and Equation 64 into Equation 62, the velocity-strains at the centre of the element ($\xi$ = 0, $\eta$ = 0) are found to be:

$$\hat{d}_x = B_{1I}\hat{v}_{xI} + \hat{z}B_{1I}\hat{\theta}_{yI}$$
$$\hat{d}_y = B_{2I}\hat{v}_{yI} - \hat{z}B_{2I}\hat{\theta}_{xI}$$
$$2\hat{d}_{xy} = B_{2I}\hat{v}_{xI} + B_{1I}\hat{v}_{yI} + \hat{z}\left(B_{2I}\hat{\theta}_{yI} - B_{1I}\hat{\theta}_{xI}\right) \tag{65}$$
$$2\hat{d}_{xz} = B_{1I}\hat{v}_{zI} + N_I\hat{\theta}_{yI}$$
$$2\hat{d}_{yz} = B_{2I}\hat{v}_{zI} - N_I\hat{\theta}_{xI}$$

where:

$$B_{1I} = \frac{\partial N_I}{\partial \hat{x}}$$
$$B_{2I} = \frac{\partial N_I}{\partial \hat{y}} \tag{66}$$

Local resultant element-centred forces and moments are obtained by suitable constitutive evaluations using the above velocity-strains and then integrating the resultant stresses through the thickness of the shell element. These local resultant element-centred forces and moments are shown to be related to the local nodal forces and moments by [35, 36]:

$$\hat{f}_{xI} = A\left(B_{1I}f_x + B_{2I}f_{xy}\right)$$
$$\hat{f}_{yI} = A\left(B_{2I}f_y + B_{1I}f_{xy}\right)$$
$$\hat{f}_{zI} = A\bar{\kappa}\left(B_{1I}f_{xz} + B_{2I}f_{yz}\right)$$
$$\hat{m}_{xI} = A\left[B_{2I}m_y + B_{1I}m_{xy} - \frac{1}{4}\bar{\kappa}f_{yz}\right]$$
$$\hat{m}_{yI} = A\left[-B_{1I}m_x - B_{2I}m_{xy} + \frac{1}{4}\bar{\kappa}f_{xz}\right]$$
$$\hat{m}_{zI} = 0 \tag{67}$$

where:

$$f_{\alpha\beta} = \int \hat{\sigma}_{\alpha\beta}\, d\hat{z}$$
$$m_{\alpha\beta} = -\int \hat{z}\hat{\sigma}_{\alpha\beta}\, d\hat{z} \tag{68}$$

and:

$m$ = moment
$f$ = force
$\bar{\kappa}$ = shear correction factor
$A$ = area of the element
$\sigma$ = stress

Hourglassing is associated with a keystone pattern of deformation as illustrated in Figure 29. The hourglass control used for the BLT shell element is based on the work of Flanagan and Belytschko [37], which involves the calculation of hourglass forces used to resist the hourglass modes. Hourglassing is a consequence of the use of a single-point quadrature under certain boundary conditions and may be severely detrimental to the finite element solution. Single-point quadrature is used because of its computational efficiency. According to Key and Hoff [20], single-point Gauss

quadrature (i.e. reduced integration) is about four times faster than a four point Gauss quadrature. The hourglass control has a minimal effect on the finite element solution; however it does slightly stiffen the overall response [35].

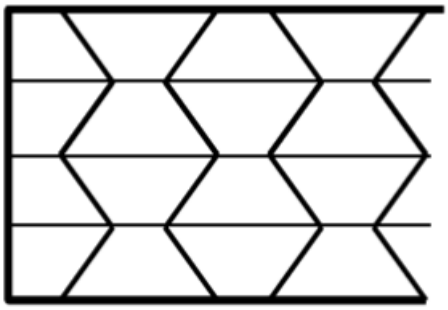

**Figure 29: Keystone pattern of deformation associated with hourglassing [31]**

Since the BLT shell element is based on Mindlin theory, both thin and moderately thick shells may be modelled with relative accuracy due to the inclusion of transverse shear strain. The performance of the BLT shell element reduces when the initial geometry of the element is warped (i.e. the four nodal points of the element do not define a flat surface) and the element is subjected to warping distortions (generated by torsion around the in-plane axis of the element).

A Key-Hoff shell element may be used as an alternative to the BLT shell element. The Key-Hoff shell element is based on the BLT shell element, where it uses a four-node $C^0$-linear quadrilateral shell element with bilinear interpolation functions, single-point (Gauss) quadrature, and Mindlin shell theory. The Key-Hoff shell element however offers two important improvements with only a moderate increase in computational cost. The improvements referred to are the inclusion of the effects of warped element geometry and the introduction of a physical stiffness in the warping deformation mode. The effects of warped element geometry are included

through the introduction of additional terms in the formulation due to unique normals at the nodal points. Introduction of a physical stiffness in the warping deformation mode diminishes the reliance on artificial hourglass control. A more realistic stiffness in the warping deformation mode is achieved through the assumption of a linear varying transverse shear stress over the element; compared to the BLT shell element with a constant stress assumption which ignores the warping deformation mode [20].

The Key-Hoff shell element was selected for use in this study to represent the structure of the aircraft due to the abovementioned improvements. Further details regarding both the BLT and Key-Hoff shell elements may be found in references [20, 35, 36].

### 1.2.7 Lagrangian and Eulerian descriptions

The time-dependent deformation of a continuous body may be described with one of two analytical approaches, namely the Lagrangian and Eulerian descriptions [29]. Consider a body with an initial configuration $C_0$, in which a particle $X$ of the body occupies position **X**, referenced to Cartesian coordinate system ($X_1$, $X_2$, $X_3$) (also referred to as the material coordinate system). After deformation (due to loading), the body assumes a new configuration $C$, and the particle $X$ now occupies position **x** in the deformed configuration $C$, as shown in Figure 30.

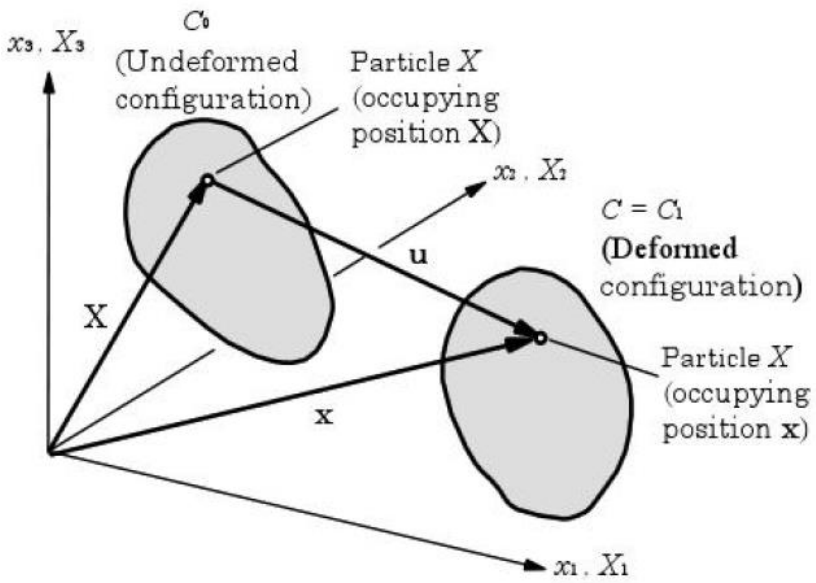


**Figure 30: Reference and deformed configurations of a body [29]**

In the Lagrangian description, the motion of the body is referred to a reference configuration, which is usually the undeformed configuration $C_0$. The current coordinates ($x_1$, $x_2$, $x_3$), along with the variation of a typical variable $\phi$ over the body, are therefore expressed in terms of the reference coordinates ($X_1$, $X_2$, $X_3$) as [29]:

$$\mathrm{x} = \mathrm{x}(\mathbf{X}, t); \quad \phi = \phi(\mathbf{X}, t) \tag{69}$$

A change in time $t$ implies that the same material particle $X$, occupying position **X** in $C_0$, has a different value $\phi$.

In the Eulerian description, the motion of a body is referred to the current configuration $C$, and $\phi$ is described with respect to the current position ($x_1$, $x_2$, $x_3$) (also termed spatial coordinates) in space currently occupied by material particle $X$ as [29]:

$$\phi = \phi(x, t); \quad \mathbf{X} = \mathbf{X}(x, t) \tag{70}$$

A change in time $t$ implies that a different value $\phi$ is observed at the same spatial location **x**, likely now occupied by a different material particle $X$.

The Eulerian description is preferred for the study of motion of fluids (including soft soil) because the configuration is known and remains unchanged. The changes of velocities, pressure, density, temperature, and so on are of interest here. The Eulerian description is less useful for the study of solid bodies as the configuration $C$ is unknown. The Lagrangian description is typically used to model structures.

MSC Dytran features a Lagrangian solver and an Eulerian solver. The nodal points of the Eulerian mesh are fixed in space and the material under analysis is said to flow through the Eulerian mesh, as shown in Figure 31. The elements therefore have constant volume and do not deform, whereas the nodal points with the Lagrangian solver move with the material resulting in element distortion and constant mass elements. The advantages of the Eulerian-based finite element approach compared to the Lagrangian-based finite element approach are that severe material deformations are allowed as the elements do not deform, tedious meshing operations are eliminated, and small time increments are prevented by eliminating the construction of small elements. Severe material and therefore element deformations associated with Lagrangian solvers may result in premature analysis termination due to numerical instabilities caused by negative element volumes, extremely small time increments, and so on.

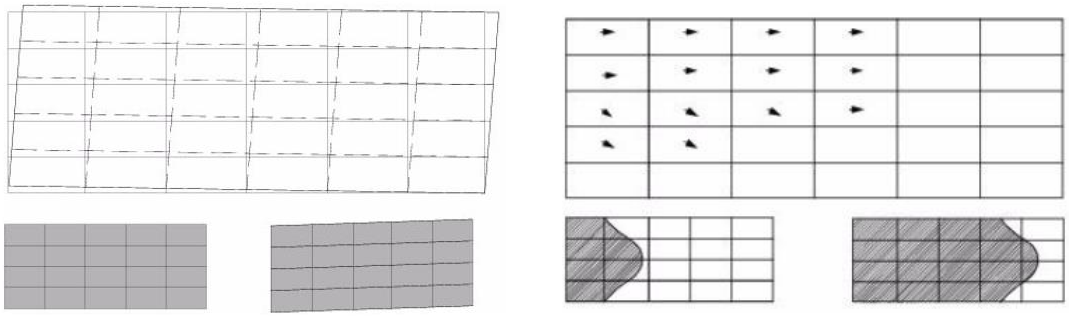

Lagrangian solver, showing element distortion

Eulerian solver, showing flow of material through fixed mesh

**Figure 31: Lagrangian and Eulerian solvers [34]**

Interaction between solvers is achieved with the General Coupling Method, where Lagrangian structures interact with Eulerian materials through the use of coupling surfaces. The coupling surface is essentially the outer surface of the Lagrangian structure and acts as a moving boundary condition for the Euler material. The pressure exerted on the coupling surface by the Euler material results in new nodal point forces on the Lagrangian structure and is displaced accordingly. The boundary for the Euler mesh is then updated due to the displacement of the Lagrangian structure.

Like the Lagrangian solver, the Eulerian solver uses the explicit time integration scheme for the solution of the dynamic equilibrium equation. As mentioned in Chapter 1 Section 2.5, stability of the central difference method requires that the time increment must be less than the time taken for a stress wave to propagate through the smallest element in the mesh. For structures (Lagrangian solver), the time increment depends on the speed of sound and smallest element dimension (refer to Equation 59); however for the Eulerian solver, the time increment depends on the smallest element dimension and the speed of sound superimposed on the material velocity. For the Eulerian solver, explicit methods are therefore conditionally stable whenever the size of the time increment satisfies:

$$\Delta t \leq \frac{L_e}{c_e + u} \tag{71}$$

where:

$L_e$ = smallest element dimension (smallest distance between nodes)
$c_e$ = speed of sound
$u$ = material velocity

Previous studies discussed in the Abstract have used an ALE approach. In the ALE approach, interaction between Eulerian and Lagrangian solvers is achieved through an ALE interface surface. Coupling between solvers requires that the velocities (or displacements) coincide at the interface. Practically, this means that one fluid node and one structural node should be placed at each point of the interface. The meshing of Eulerian elements can therefore be complex as the Lagrangian and Eulerian elements at the interface should be coincident [38, 39]. The ALE mesh may be moved in an arbitrary specified way to give a continuous rezoning capability, which allows for greater resolution than in a purely Eulerian approach where the mesh is fixed in space [38]. Rezoning involves the mapping of a distorted mesh onto a newly defined “regular” mesh [40]. An additional disadvantage of the ALE approach is that structural deformation should be relatively smooth over time (but not necessarily small in magnitude), which may not be the case in crashworthiness analyses. It is interesting to note that the ALE domain can be completely Lagrangian or Eulerian (or something in between) depending on the specified motions [40]. Further details regarding the ALE approach may be found in various readily available literature sources.

### 1.2.8 Contact

Contact surfaces may be used to model the interaction among parts of a finite element model. For general contact between two surfaces, MSC Dytran defines one surface as a slave surface and the second surface as a master surface, where each element face is called a segment of a surface. It is important to understand how contact is defined between Lagrangian nodal points and elements since various user-defined input parameters may be required for successful analysis. If a slave nodal point penetrates a master segment, forces are applied in a direction normal to the master segment to prevent further penetration. A penalty method is used to calculate the contact force in MSC Dytran. Here, Newton's Second Law is used where the contact force is proportional to the penetration distance divided by the time increment squared (i.e. average acceleration) and multiplied by an effective mass [41].

It is recommended that the mesh density of the slave surface be finer than that of the master surface, since the slave nodal points are checked for penetration of the master segments and not vice versa. If this recommendation is not adhered to, penetrations may occur, which may lead to hourglassing.

## 1.3 Anthropomorphic test devices and occupant analysis codes

Anthropomorphic test devices (ATDs) are instrumented mechanical devices that are used to replicate the human body response under various loading and accelerative conditions [42]. Modern ATDs, also known as crash test dummies, are required to be biofidelic. This means that they must replicate human physical characteristics such as mass, geometry, stiffness, and energy absorption and dissipation in order to achieve mechanical responses corresponding to human responses. These responses are trajectory, velocity,

acceleration, deformation, and articulation. Strategically placed transducers allow for the measurement of data required for injury risk assessment such as forces, moments, accelerations and deformations. Various ATDs currently exist for impact testing, such as the Hybrid II, Hybrid III, and Federal Aviation Administration (FAA) Hybrid III. The 50$^{th}$ percentile adult male Hybrid III ATD (refer to Figure 32) is the most extensively used in the automotive industry and has notably improved component biofidelity compared to the Hybrid II ATD. The 50$^{th}$ percentile adult male Hybrid III ATD represents an occupant of average height and mass, having a total mass of 78.2 kilograms and stands 1.75 metres tall. It has excellent biofidelity, durability, repeatability and reproducibility [43]. The 50$^{th}$ percentile adult male Hybrid III ATD was developed for automotive testing and therefore was not designed for accurate response to vertical impacts as is experienced in the aircraft crash environment. Special consideration must therefore be given to the effects of the impact force in the vertical direction. In the aerospace industry, the Hybrid II ATD or the FAA Hybrid III ATD is commonly used. The FAA Hybrid III ATD combined parts from the standard Hybrid II and Hybrid III ATDs to incorporate key features of the Hybrid II ATD for the aviation environment [44]. The primary key feature is the straight lumbar spine from the Hybrid II ATD incorporated into the FAA Hybrid III ATD, unlike the standard Hybrid III ATD with a curved spine. The straight spine is used because it is believed to better replicate the seated position of an occupant in the aerospace industry, whilst the curved spine is believed to better replicate the seated position of an occupant in the automotive industry. The differences between the spines of the Hybrid II, Hybrid III, and FAA Hybrid III ATDs are currently not well understood [45]. Polanco and Littell [45] compared the impact responses of the 50$^{th}$ percentile Hybrid III ATD with a curved lumbar spine to that of the 50$^{th}$ percentile Hybrid III and Hybrid II ATDs with a straight lumbar spine by conducting vertical drop tests. The trend observed was that the compression loads in the curved lumbar spine are lower than the loads in the straight lumbar spine.

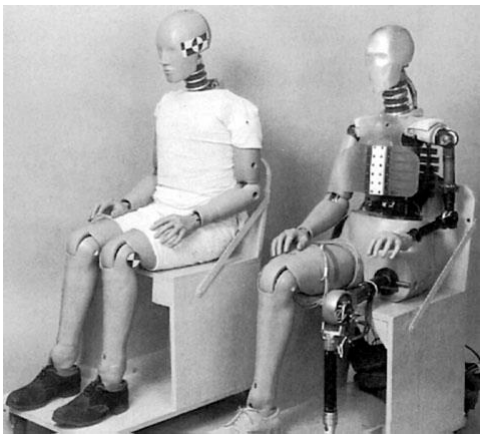

**Figure 32: 50th percentile adult male Hybrid III ATD with and without its skin [42]**

The Articulated Total Body (ATB) model and Mathematical Dynamic Model (MADYMO) are numerical codes primarily used for predicting gross human body response in various dynamic environments. These codes may be integrated with the finite element code MSC Dytran to allow for the interaction of the occupant with structural components modelled in MSC Dytran. In the aviation environment, the ATB and MADYMO codes are used for applications such as aircraft seat ejection, seat and passenger response in an aircraft crash, and space shuttle escape. The ATB and MADYMO codes were originally developed as linked, rigid body dynamics models, therefore analyses with these codes could not predict damage to biological tissue. Models have since been developed to directly relate external loading to internal injury mechanisms, such as the cervical spine model of de Jager in MADYMO [46]; however are ignored for the purposes of this study. The ATB code was implemented in this study due to availability of the code and supporting documentation. Details of the ATB model are discussed in Chapter 2 Section 1.

## 1.4 Human tolerance limits

Crashworthiness assessment requires an understanding of human tolerance limits to abrupt accelerations and the effect restraint systems have on preventing injurious contacts and providing support. For the discussions that follow, refer to Figure 33 for a typical coordinate system used for a seated human.

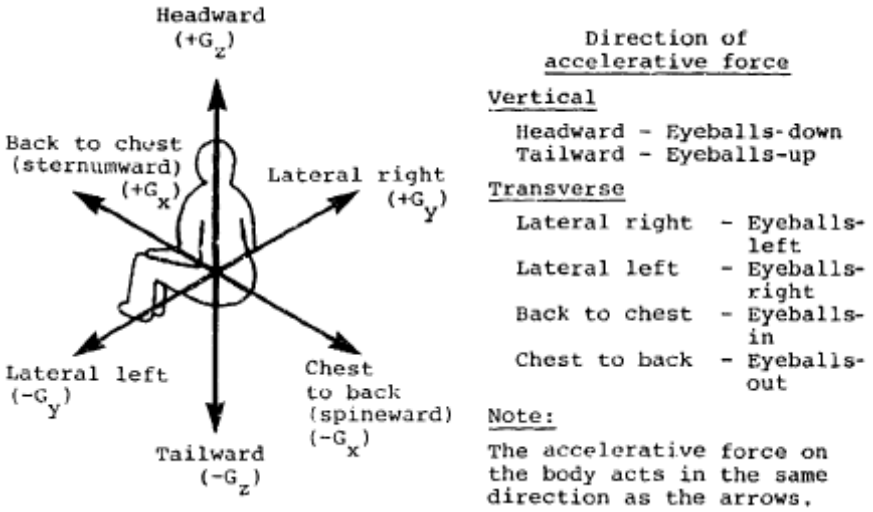


**Figure 33: Human coordinate system and direction of forces [1]**

The tolerance of the human body to impact forces depends on various factors, including characteristics of the individual such as age, gender, and general health. Probability of survival depends largely on the restraint system used. For example, use of upper and lower torso restraints may prevent the head and chest from striking the surrounding structure, therefore significantly reducing the probability of severe or fatal injury during particular crash conditions. The magnitude, direction and duration of the applied accelerative forces have definite effects on human tolerance limits. Table 1 presents whole-body accelerative force tolerance levels along different axes of the human body for a pulse duration of 0.1 seconds. A variety of full-torso

restraint systems were used to collect the data presented in Table 1. If the duration of an applied accelerative force is increased, the human tolerance level for the same magnitude decreases, and vice versa. Additionally, with lower levels of restraint, the tolerance levels significantly reduce. As is evident in Table 1, the human body can tolerate much greater forces in the $G_x$ direction compared to the $G_z$ direction. This is mainly due to the susceptibility of the lumbar vertebrae, which must support the majority of the upper torso load, to compression fracture. Spinal alignment is necessary to carry the maximum upper torso loads. Whole-body acceleration is not generally used as a tolerance criterion in aviation regulations due to differences in seat and restraint system performance; however may be useful during the initial phase of aircraft design [42]. The rate of onset of the applied force also has an effect on human tolerance levels; however is currently not well understood [1].

**Table 1: Human whole-body accelerative force tolerance levels along different axes of the human body for a pulse duration of 0.1 seconds and full restraint system [1, 47]**

| Direction of accelerative force | | Occupant's inertial response | Tolerance level (G) |
|---|---|---|---|
| Headward | (+Gz) | Eyeballs down | 20 - 25 |
| Tailward | (-Gz) | Eyeballs up | 15 |
| Lateral right | (+Gy) | Eyeballs left | 20 |
| Lateral left | (-Gy) | Eyeballs right | 20 |
| Back to chest | (+Gx) | Eyeballs out | 45 |
| Chest to back | (-Gx) | Eyeballs in | 45 |

As an example of the requirements used for crashworthiness assessment, Federal Aviation Regulation (FAR) 23 contains airworthiness standards for normal, utility, acrobatic and commuter category airplanes [48]. Compliance with requirements must be shown for emergency landing dynamic conditions

as stated in FAR 23.562 subpart C. Select requirements from this regulation regarding occupant survivability are summarised below:

- When contact with adjacent seats, structure, or other items in the cabin can occur, protection must be provided so that the head impact does not exceed a head injury criterion (HIC) of 1000.
- The loads in the individual shoulder harness straps must not exceed 794 kilograms (7789.14 Newtons).
- The lap belt must remain on the ATD's pelvis during impact.
- Each shoulder harness strap must remain on the ATD's shoulder during impact.
- The compression load between the pelvis and lumbar spine of the ATD may not exceed 680 kilograms (6670.8 Newtons).
- The attachment between the seat / restraint system and the test fixture must remain intact, although seat deformation may occur.

As per FAR 23.562 subpart B, the requirements from FAR 23.562 subpart C must be satisfied through tests conducted with an ATD defined by 49 CFR (Code of Federal Regulations) Part 572 subpart B, or an approved FAA equivalent, with a nominal mass of 77 kilograms and seated in an upright position. The choice of ATD is not specified; however the $50^{th}$ percentile adult male Hybrid II and the FAA Hybrid III ATDs satisfy these requirements.

The HIC is used to quantitatively assess the head injury risk in ATDs. The HIC considers both the impulse duration and resultant translational acceleration of the head during impact. The HIC cannot predict injury mechanism and severity of injuries but it does provide an initial approximation of the general injury risk. The HIC is a unitless number and provides a pass or fail measure. The maximum HIC is defined as follows [49]:

$$HIC = max_{t1,t2}\left[(t_2 - t_1)\left(\frac{1}{t_2 - t_1}\int_{t_1}^{t_2} a(t)dt\right)^{2.5}\right] \quad (72)$$

where:

$t_1$ = initial time of the interval (s)

$t_2$ = final time of the interval (s)

$a(t)$ = resultant translational head acceleration (G) at the centre of gravity of the head

Federal Motor Vehicle Safety Standard (FMVSS) 208 specifies that the HIC time interval $(t_2 - t_1)$ be equal to or smaller than 36 milliseconds [1] as longer acceleration times do not increase the risk of injury. The limited time interval effectively eliminates lower level accelerations that are not injurious and focuses on the short duration and high acceleration peak values. According to Henn [49], experts agree that HIC values above 1000 are life threatening. An issue surrounding the use of the HIC is whether it can be used for contact and non-contact impact scenarios. Contact injuries of the head result from deformation of the skull due to a direct impact to the head, whereas non-contact injuries result from injuries to the brain produced by the head's inertial response to acceleration. One of the concerns regarding the HIC is that its formulation is based on the Wayne State Tolerance Curve (WSTC), which represents a tolerance to skull fracture and not brain injury. Although this suggests that the HIC is not appropriate for non-contact impacts, researchers have still applied it to both contact and non-contact impacts [42].

## 1.5 Crash dynamics and environment

The primary environmental conditions considered for aircraft crashworthiness assessment were the impact terrain, impact angle, impact velocity, and attitude as shown in Figure 34. The aircraft attitude is stated in degrees of pitch, yaw, and roll of the aircraft, with positive directions in the direction of the large arrows shown in Figure 34.

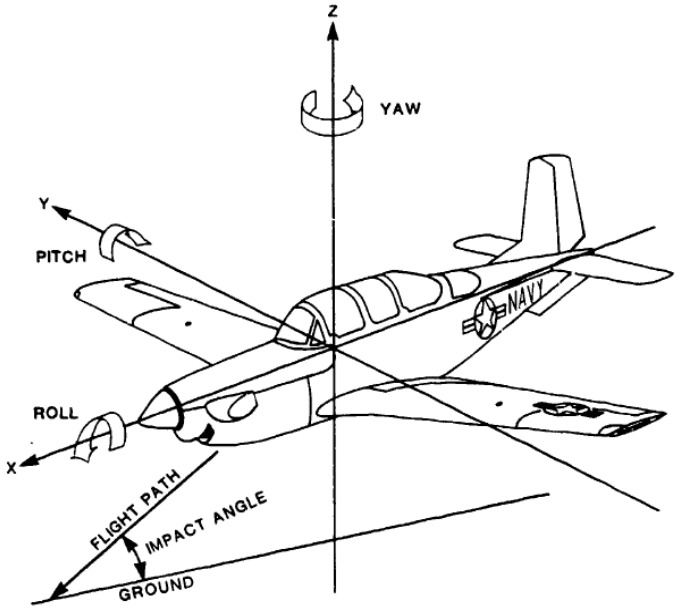


**Figure 34: Aircraft coordinate system and attitude directions [50]**

Typical aircraft kinematics following a nose-down impact into a hard terrain is shown in Figure 35. After initial impact with the terrain, the aircraft structure resists the contact forces and produces pitching moments that rotate the aircraft's velocity vector to a direction parallel to the ground. A tail slap-down response may be observed at high impact velocities. The change in aircraft pitch produces bending moments in the fuselage, which will result in compressive or tensile stresses along the length of the fuselage. Additional fuselage compressive stresses due to longitudinal impact forces may be added to the bending stresses along the length of the fuselage. For an impact into soft soil, an aircraft displaces a large mass of soil which may be

projected a considerable distance from the point of impact. The momentum transfer associated with the soil displacement may result in significant forces on the lower forward fuselage [42].

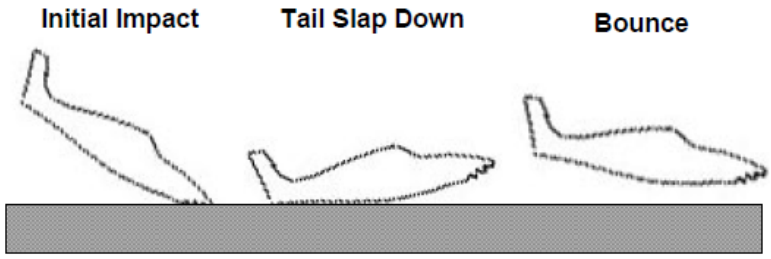


**Figure 35: Aircraft kinematics following impact into a hard terrain [42]**

As indicated above, the crash dynamics of aircraft are dependent on the characteristics of the impact surface. It is therefore important to consider impacts into both hard and soft terrains when assessing aircraft crashworthiness. Sareen et al. [51] previously observed different structural responses for different impact terrains. As represented in Figure 36, it was seen that for rigid terrains, concentrated loading is introduced into the stiffest parts of the aircraft structure, whereas for soft soil impacts, distributed loading is introduced into the fuselage skin. Additionally, nose down impacts into hard terrains typically produce sliding impacts with high aircraft decelerations in the vertical direction, whilst impacts into soft terrains typically produce high aircraft decelerations in the longitudinal direction and stop abruptly due to digging in of the aircraft into the soft terrain. These high longitudinal decelerations may result in failure of occupant restraint systems and may also compromise survivability of the occupant volume. A “crashworthy” aircraft would be designed to pitch positively out of a crater created by a nose-down impact into soft terrain, thereby increasing the stopping time and reducing longitudinal decelerations. Fundamentally, occupant survivability is significantly enhanced by increasing the aircraft’s stopping time, thereby reducing decelerations.

**Figure 36: Loading differences during hard surface (left) and soft soil / water (right) impact of a fuselage [51]**

Terry et al. [52] performed experiments of “crashworthy” small composite airframes impacting into hard and soft soil terrains. Figure 37 shows the time sequence for an impact into hard terrain, whilst Figure 38 shows the time sequence for an impact into soft soil terrain. The impact velocity was approximately 25 metres per second for both impacts. The impact angle for the hard terrain experiment was 26 degrees. The impact angle for the soft soil experiment was 30 degrees with a 6.5 degree angle of attack (i.e. angle between flight path and longitudinal axis of the aircraft). The roll and yaw angles were considered negligible. For the impact into soft soil, the crashworthy concepts introduced into the airframe allowed the airplane to pitch positively out of the crater and slide on top of the soil. It was also noted that the impacts onto hard terrain produced higher loads normal to the terrain than parallel to the terrain, whilst opposite results were produced for the soft soil terrain. Main wing spar failure was observed for impacts into both hard and soft soil terrains.

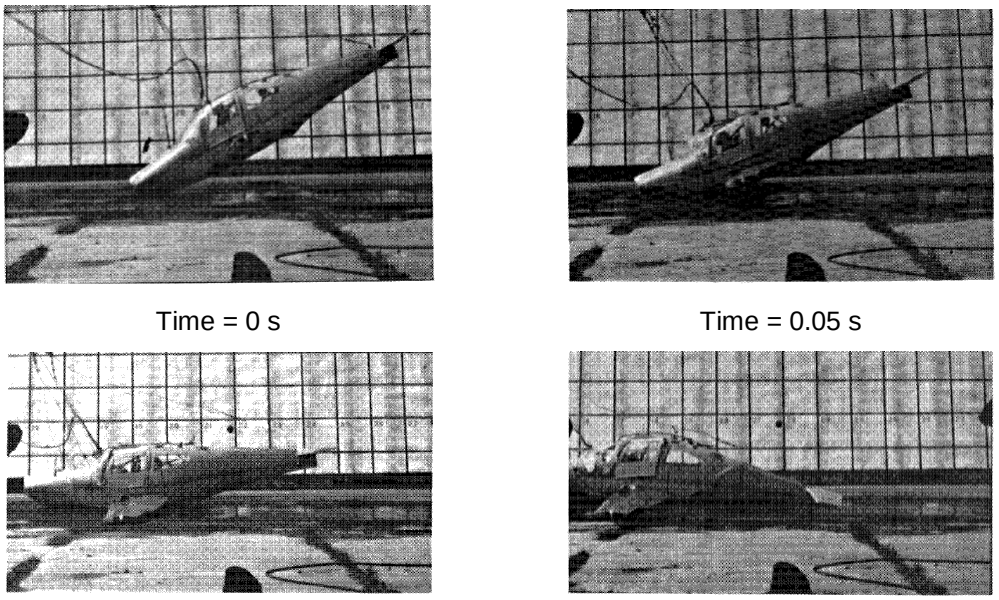

Time = 0 s  Time = 0.05 s

Time = 0.1 s  Time = 0.15 s

**Figure 37: Time sequence of a "crashworthy" small composite airframe impacting into a hard terrain [52]**

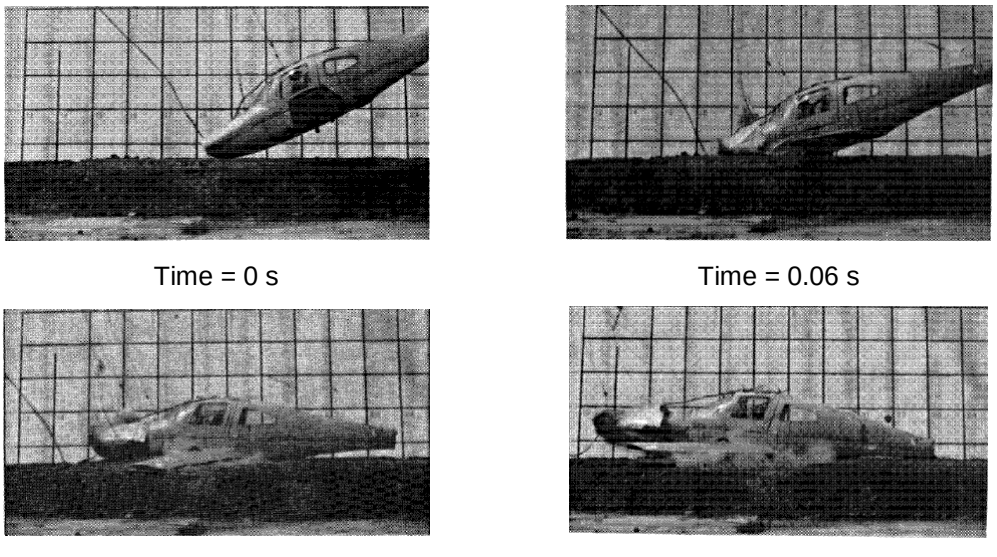

Time = 0 s  Time = 0.06 s

Time = 0.12 s  Time = 0.18 s

**Figure 38: Time sequence of a "crashworthy" small composite airframe impacting into soft soil terrain [52]**

# CHAPTER 2: NUMERICAL MODEL DEVELOPMENT

## 2.1 The Articulated Total Body model and its integration within MSC Dytran

The Articulated Total Body (ATB) model is primarily used for predicting gross human body response in various dynamic environments. In the ATB code, the human body is typically represented by 17 rigid segments (ellipsoids), which are connected by 16 joints as shown in Figure 39. Segment 1 (lower torso) is considered as the parent or reference segment and is used for positioning of the body. The description and ATB symbol assigned to each segment and joint, including connectivity, are shown in Table 2.

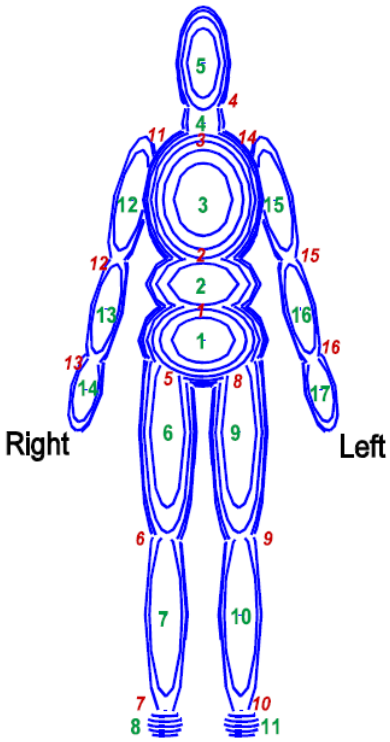


**Figure 39: ATB indicating segment (green) and joint (red) connectivity [53]**

**Table 2: ATB segment and joint assignments and connectivity [53]**

| Segment | Segment name | Symbol | Joint | Joint name | Symbol | Connects segments |
|---|---|---|---|---|---|---|
| 1 | Lower torso | LT | 1 | Pelvis | P | 1 – 2 |
| 2 | Centre Torso | CT | 2 | Waist | W | 2 – 3 |
| 3 | Upper Torso | UT | 3 | Neck pivot | NP | 3 – 4 |
| 4 | Neck | N | 4 | Head pivot | HP | 4 - 5 |
| 5 | Head | H | 5 | Right hip | RH | 1 – 6 |
| 6 | Right upper leg | RUL | 6 | Right knee | RK | 6 – 7 |
| 7 | Right lower leg | RLL | 7 | Right ankle | RA | 7 – 8 |
| 8 | Right foot | RF | 8 | Left hip | LH | 1 – 9 |
| 9 | Left upper leg | LUL | 9 | Left knee | LK | 9 – 10 |
| 10 | Left lower leg | LLL | 10 | Left ankle | LA | 10 – 11 |
| 11 | Left foot | LF | 11 | Right shoulder | RS | 3 – 12 |
| 12 | Right upper arm | RUA | 12 | Right elbow | RE | 12 – 13 |
| 13 | Right lower arm | RLA | 13 | Right wrist | RW | 13 – 14 |
| 14 | Right hand | RH | 14 | Left shoulder | LS | 3 – 15 |
| 15 | Left upper arm | LUA | 15 | Left elbow | LE | 15 – 16 |
| 16 | Left lower arm | LLA | 16 | Left wrist | LW | 16 - 17 |
| 17 | Left hand | LH | | | | |

MSC Dytran and ATB are coupled together to investigate occupant and vehicle interaction. They run concurrently, exchanging data as the analysis proceeds. The following steps are used to incorporate the ATB model into MSC Dytran:

1. Each segment contact ellipsoid used in ATB is defined in MSC Dytran through the RELEX entry. This entry defines a rigid ellipsoid whose properties are defined by ATB [54]. ATB provides segment data such as mass and moments-of-inertia, and joint data such as viscous and spring characteristics.
2. Shell elements are generated to represent the contact surfaces of the ATB ellipsoid segments in MSC Dytran. The shell elements cover the

ATB ellipsoid segments and also create more realistic human features as shown in Figure 40.

3. The shell elements representing the ellipsoid contact surfaces are attached to the appropriate ATB segment with the use of the RCONREL entry in MSC Dytran. This entry defines a connection between a rigid ellipsoid and Lagrangian nodal points or rigid bodies (i.e. MATRIG entries) [54].

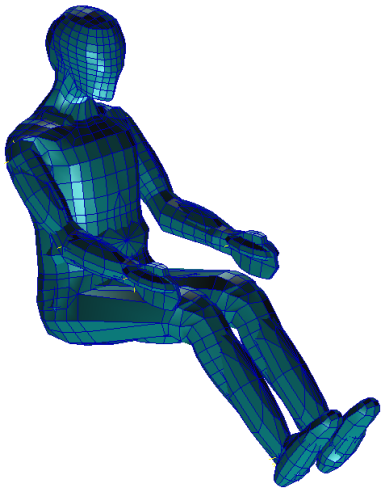

**Figure 40: MSC Dytran finite element representation of the 50th percentile adult male Hybrid III ATD**

MSC Dytran uses ATBSEG entries to define the position and orientation of the ATB segments. The position and orientation defined in the ATB G.2 and G.3 input cards are overwritten by the definitions provided in the ATBSEG entries [54].

## 2.2 Sled test analysis

### 2.2.1 Introduction

The technique required to examine the dynamic response of an occupant with MSC Dytran, coupled with the ATB model, is presented. The technique is demonstrated through the analysis of a sled test found in MSC Dytran's Example Problem Manual [55] and was validated through the comparison of numerical and experimental results found in the literature. The 50$^{th}$ percentile adult male (occupant of average height and mass) Hybrid III anthropomorphic test device (ATD) was used to replicate the human body response in the sled test. This ATD is not recommended for the aviation environment (refer to Chapter 1 Section 3); however the technique used to represent this ATD in the analysis models is similar for alternative ATDs, such as the 50$^{th}$ percentile adult male Hybrid II ATD.

### 2.2.2 Sled finite element model

The sled was defined in MSC Dytran, unlike in MSC Dytran's Example Problem Manual [55] where it was defined in the ATB code. The sled was created with the ATB model's inertial coordinate system in mind, which is with the positive z-axis pointing downward (from head to feet). The positive x-axis represents the forward direction (from back to chest) and the positive y-axis represents the lateral direction (from occupant's left to right side) [53]. The sled consisted of a back seat, bottom seat, floor, toe-board, and firewall as shown in Figure 41. The sled finite element model consisted of 1680 four-node quadrilateral shell elements, all defined as rigid with the MATRIG entry. The "rigid body object" function was used to constrain all six degrees of freedom for all nodal points associated with the sled.

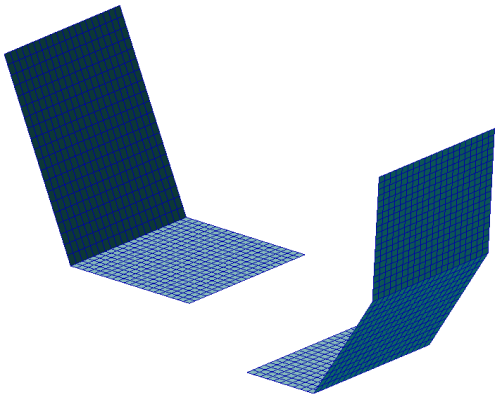

**Figure 41: MSC Dytran finite element model of the sled**

The 50th percentile Hybrid III ATD model uses the following identification numbers:

- Nodal points 20001 to 24138
- Elements 20001 to 24299
- Material ID's 20001 to 20017
- Property ID's 20001 to 20404

It may therefore be necessary to renumber all nodes, elements, materials and property sets to numbers above 30000 to ensure no entities are overwritten in the analysis.

### 2.2.3 Occupant positioning

The 50th percentile adult male Hybrid III ATD was manipulated and positioned in the sled as required. The ATD nodes must not penetrate the sled due to the contact formulation in MSC Dytran; otherwise contact may fail between the sled and ATD. The ATD must therefore be allowed to fall into a static position. Perfect equilibrium between the sled and ATD is generally not achievable due to this positioning process (i.e. initial gaps exist between the contact surfaces). Small initial accelerations are tolerable as long as they are negligible when compared to the accelerations induced by the dynamic

environment [53]. These initial accelerations were kept small by positioning the ATD as close as possible to the sled.

### 2.2.4 Seatbelt finite element model

The seatbelt geometry was created using one-dimensional curves as shown in Figure 42. The nodes of the ATD were used to help create the profile of the seatbelt. Slight penetration of the seatbelt curves on the ATD is allowed. The CONTACT card takes care of this initial penetration by use of the BELT1 entry for the algorithm version. This entry initially repositions slave nodes on top of the closest master face [54].

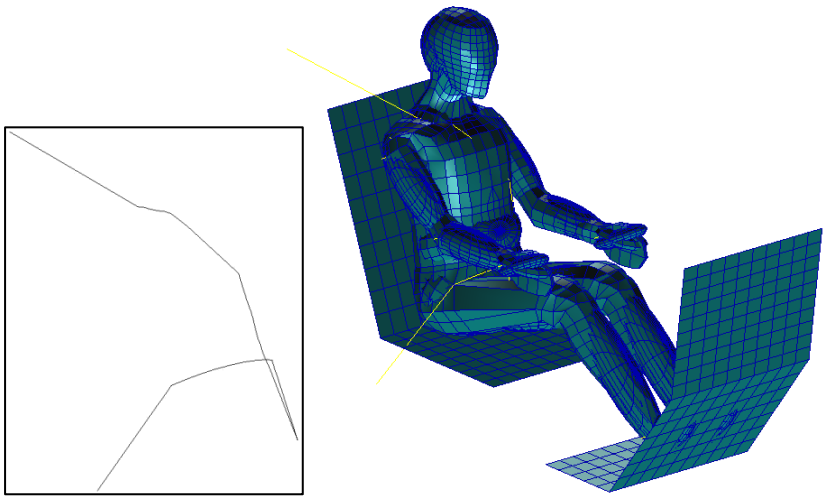

**Figure 42: MSC Dytran sled test setup with an insert showing the seatbelt geometry**

The seatbelt element properties were defined with the PBELT entry, which references a CROD entry (tension and compression element). The properties defined in this sled test were [55]:

- Belt element density (DENSITY) = 0.1860205 kg/m
- Damping force coefficient (DAMP1) = 0.1

- Damping force coefficient (DAMP2) = 0.1

The seatbelt loading / unloading and prestress curves are shown in Figure 43. The nodes at the seatbelt anchor points were fully constrained.

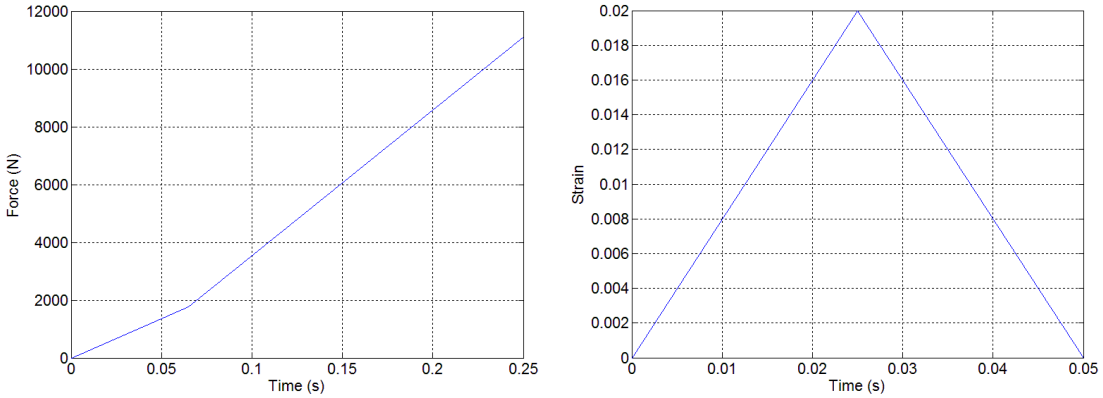


Loading / unloading curve Prestress curve

**Figure 43: Seatbelt loading / unloading and prestress curves**

### 2.2.5 Contact definition

For computational efficiency, contact was defined between specific areas of the ATD and sled. For example, contact was separately defined between the ATD's feet and toe-board only. An example CONTACT card is shown in Figure 44. The sled and seatbelt were defined as the slave nodes and the ATD as the master faces. For simple contact set definition, property sets were used to define the contact surfaces. Table 3 and Figure 45 show a list of the various property set identification numbers (PIDs) associated with the ATD for convenience.

```
$ BACK SEAT & DUMMY
$
CONTACT,1,ELEM,PROP,802,801,0.62,0.62,1,+
+,V4,TOP,FULL,,0,0.1,NO,NONE,+
+,,,DISTANCE,0.01,,0.001,,,+
+,0.0001
SET1,801,20101,20103,20104,20105,20301,THRU,20303
SET1,802,30000,THRU,30399
$
$ BOTTOM SEAT & DUMMY
$
CONTACT,2,ELEM,PROP,804,803,0.62,0.62,1,+
+,V4,TOP,FULL,,0,0.1,NO,NONE,+
+,,,DISTANCE,0.01,,0.001,,,+
+,0.0001
SET1,803,20101,20106,20107,20109,20110,20304,20305,+
+,20307,20308
SET1,804,30400,THRU,30799
$
$ TOEBOARD & DUMMY
$
CONTACT,3,ELEM,PROP,806,805,0.62,0.62,1,+
+,V4,TOP,FULL,,0,0.1,NO,NONE,+
+,,,DISTANCE,0.01,,0.001,,,+
+,0.0001
SET1,805,20108,20111
SET1,806,31000,THRU,31279
$
$ BELT & DUMMY
$
CONTACT,4,GRID,PROP,902,901,1,1,1,+
+,BELT1,TOP,FULL,,,,,SLAVE,+
+,,,,,,,,,+
+,,,,,,,2.54E-3
SET1,901,20101,20103,20104,20106,20109,20112,20114,+
+,20301,THRU,20304,20307,20310,20313
SET1,902,60000,THRU,60068
$
```

**Figure 44: Example CONTACT card defining contact between the ATD (dummy) and sled**

**Table 3: 50th percentile adult male Hybrid III property sets [55]**

| Rigid skin shell elements | | Coated rigid ellipsoid shell elements | | Connecting skin shells (DUMMY elements) | |
|---|---|---|---|---|---|
| Name | PID | Name | PID | Name | PID |
| Lower torso | 20101 | Lower torso | 20201 | Upper neck | 20301 |
| | | Middle torso | 20202 | Lower neck | 20302 |
| Upper torso | 20103 | Upper torso | 20203 | Middle torso | 20303 |
| Neck | 20104 | Neck | 20204 | Right upper leg | 20304 |
| Head | 20105 | Head | 20205 | Right knee | 20305 |
| Right upper leg | 20106 | Right upper leg | 20206 | Right ankle | 20306 |
| Right lower leg | 20107 | Right lower leg | 20207 | Left upper leg | 20307 |
| Right foot | 20108 | Right foot | 20208 | Left knee | 20308 |
| Left upper leg | 20109 | Left upper leg | 20209 | Left ankle | 20309 |
| Left lower leg | 20110 | Left lower leg | 20210 | Right shoulder | 20310 |
| Left foot | 20111 | Left foot | 20211 | Right elbow | 20311 |
| Right upper arm | 20112 | Right upper arm | 20212 | Right wrist | 20312 |
| Right lower arm | 20113 | Right lower arm | 20213 | Left shoulder | 20313 |
| Left upper arm | 20114 | Left upper arm | 20214 | Left elbow | 20314 |
| Left lower arm | 20115 | Left lower arm | 20215 | Left wrist | 20315 |
| Right hand | 20116 | Right hand | 20216 | | |
| Left hand | 20117 | Left hand | 20217 | | |

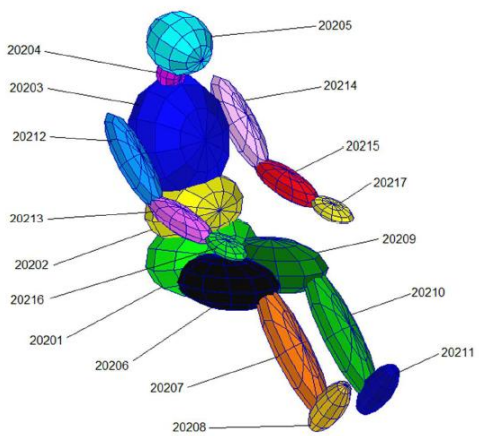


Rigid ellipsoid property sets

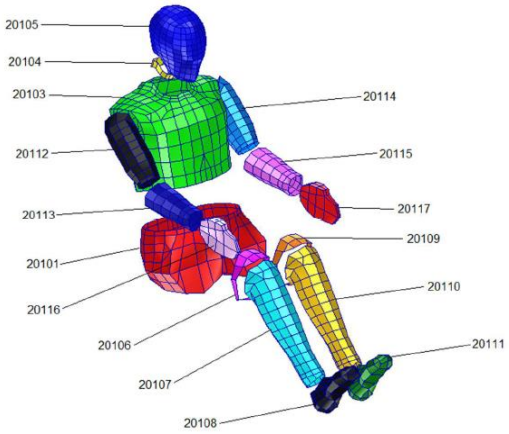


Rigid skin property sets

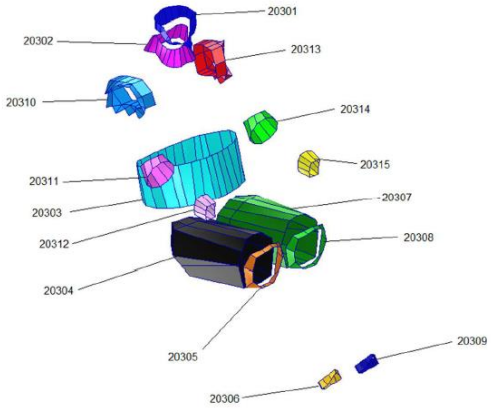


Connecting skin property sets

**Figure 45: 50th percentile adult male Hybrid III property sets**

Entries in the CONTACT card that have a significant effect on the analysis results include the mass-weighting factor (WEIGHT) and contact force scale factor (FACT). The friction coefficients have a significant effect for contact between the seatbelt and ATD. If the friction coefficients are too small, belt slippage through the ATD may occur. All friction coefficients were assumed due to a lack of experimental data. The mesh density of the sled also has an effect on analysis results. The mesh density of the slave surface (i.e. sled) must be finer than that of the master surfaces (i.e. ATD) [39].

### 2.2.6 Occupant loading

In MSC Dytran, an acceleration field can be applied to the ATB segments with the use of the ATBACC entry. The input card used for the sled test is shown in Figure 46 and the resulting acceleration profile is shown in Figure 47.

```
BEGIN BULK
$
$ Apply an x-acceleration to the dummy
$
TLOAD1,1,201,,,202
$
$ Offset with time to:
$     - allow the belt to prestress itself
$
TABLED1,202,,,,,,,,+
+,0.0E+00, 0.0,1.0E-02, 5.0,2.0E-02,12.0,3.0E-02,17.0,+
+,4.0E-02,22.0,5.0E-02,23.7,6.0E-02,23.0,7.0E-02,19.0,+
+,8.0E-02,15.0,9.0E-02,12.5,1.0E-01, 7.5,1.1E-01, 1.0,+
+,1.2E-01, 0.0,1.3E-01, 0.0,XOFFSET,50.0E-3
$
$ Table is acceleration in G
$ Use SCALE to convert it into m/s2 :  1 G = 9.8 m/s2
$
ATBACC,201,,9.8,1.0,0.0,0.0,,,+
+,LT,MT,UT,N,H,RUL,RLL,RF,+
+,LUL,LLL,LF,RUA,RLA,LUA,LLA,RHD,+
+,LHD
$
ENDDATA
```

**Figure 46: MSC Dytran input card showing the use of the ATBACC entry to apply an acceleration field to ATB segments**

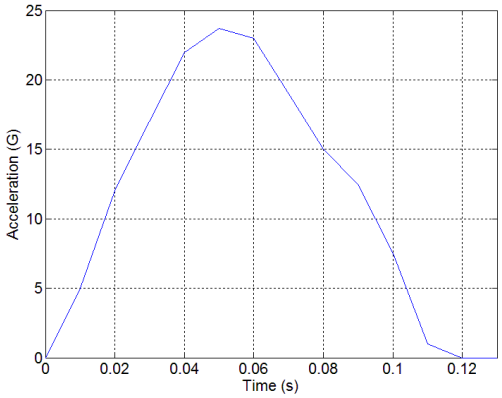


**Figure 47: Sled test acceleration profile**

The ATB input file (file extension ".ain") is written in FORTRAN format. Every line of the file corresponds to an input card with a unique alphanumeric identification. Each input card contains different parameters which defines the ATB model. These cards can be edited to, for example, apply an initial velocity to the ATD and request additional outputs such as joint forces.

An initial velocity for the ATD was not required for the sled test; however its application is described here as it is used in the full-scale crashworthiness models. In the ATB input file, field 8 of the G.1 input card must be set to 1. This indicates that the initial velocity will be supplied in card G.2. Fields 4 to 6 of card G.2 specify the x, y, and z components for the initial velocity. An example input card is shown in Figure 48.

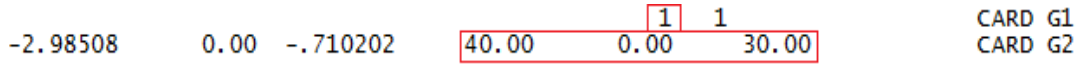


**Figure 48: Example ATB input file indicating inputs (outlined in boxes) required to apply an initial velocity to the ATD**

### 2.2.7 Requesting additional outputs

The compression load between the pelvis and lumbar spine is required to assess the survivability of the occupant in aircraft crashworthiness analyses; however it was not required for the purposes of the sled test. This joint load must be requested in the ATB input file as it is not a standard output. The MSC Dytran ATB-H-OUTPUT entry generates MSC Dytran time history files containing the outputs requested in the ATB input file. Figure 49 shows the ATB input cards that require editing, cards H.7 and H.9. Field 1 of both cards specifies the number of joints which require time history outputs. The remaining fields in card H.7 represent the ATB joint numbers (as shown in Figure 39 and Table 2) for which time history outputs are required. The remaining fields in card H.9 are represented as pairs of data. The first

number represents the reference segment that the joint forces are given in. The second number represents the joint where forces are required. The joint forces, at the joint location, keep the joined segments from separating. For the compression load between the pelvis and lumbar spine, the forces for joint 1 (pelvis) are required.


**Figure 49: Example ATB input file indicating values required to add joint time history output data ("pairs of data" are outlined in boxes)**

### 2.2.8 Results and discussion

MSC Dytran's representation of the gross body motion for the 50$^{th}$ percentile adult male Hybrid III ATD during a sled test is shown in Figure 50. The gross body motion results, although essentially qualitative, appear reasonable. Additionally, Figure 51 shows a comparison of gross body motion results presented in this study compared to results presented by Gong et al. [56] for validation purposes. As can be seen, the results at 0.125 seconds appear to be almost identical.

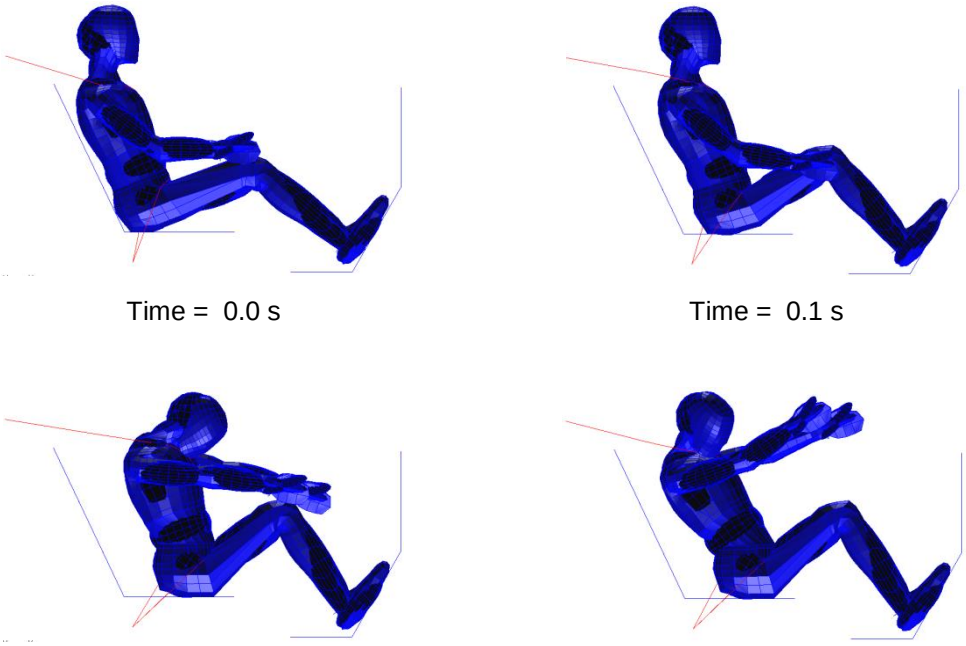


**Figure 50: MSC Dytran representation of the gross body motion for the 50th percentile adult male Hybrid III ATD during a sled test**

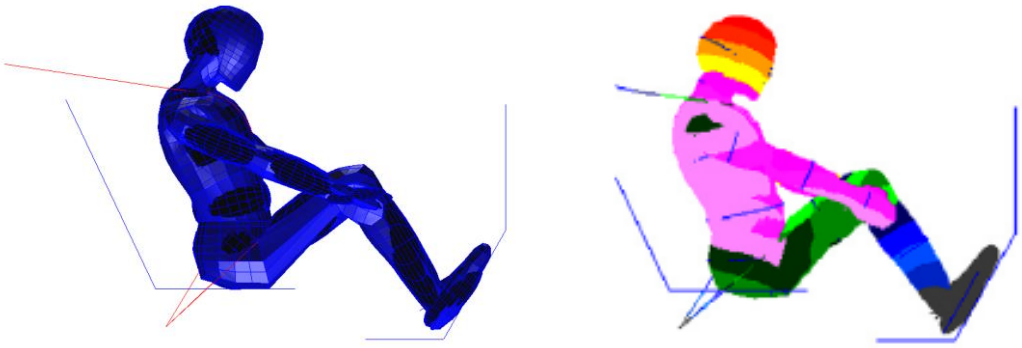


**Figure 51: Comparison of sled test gross body motion results at 0.125 seconds in MSC Dytran**

Resultant accelerations for the head, lower torso, and upper torso were filtered in MATLAB using a low-pass digital Butterworth filter with zero-phase distortion. The normalised cut-off frequency and filter order were set to 0.1 and 2 respectively for all resultant accelerations. The fast Fourier transform

was used to determine the main frequency components, thereby enabling the selection of suitable cut-off frequencies. Refer to Appendix A for further details regarding the low-pass digital Butterworth filter and fast Fourier transform. Figure 52 shows a comparison between numerical model results and experimental results acquired from Teng et al. [57]. The ATB acceleration output shown in MSC Dytran excludes the input acceleration and / or gravity applied. This is done so that only the reaction acceleration is shown, which is directly used for the HIC calculation. The trends of the accelerations are similar when comparing the numerical model results with the experimental results. The peak acceleration values are also in close agreement when comparing the numerical model results with the experimental results.

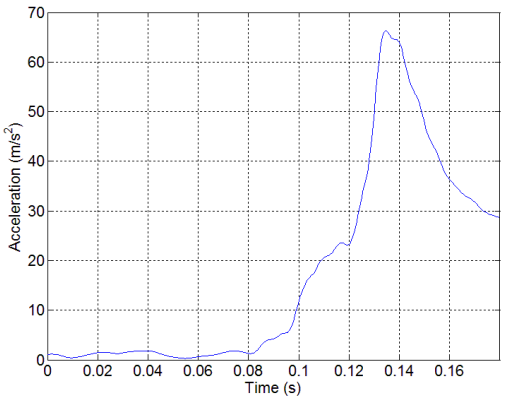


MSC Dytran / ATB resultant head acceleration (peak acceleration = 66.4 G)

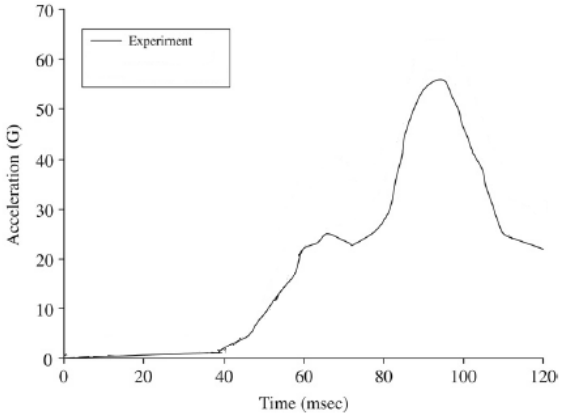


Experimental resultant head acceleration (peak acceleration = 55.7 G) [57]

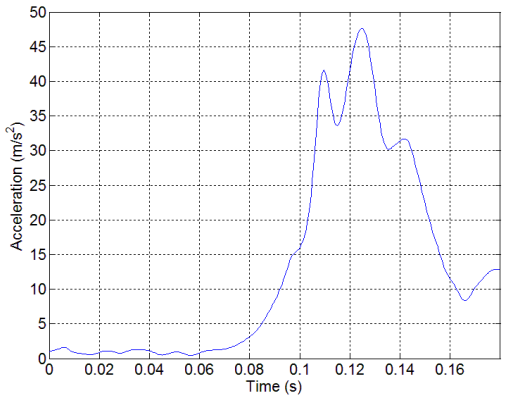


MSC Dytran / ATB resultant upper torso acceleration (peak acceleration = 47.7 G)

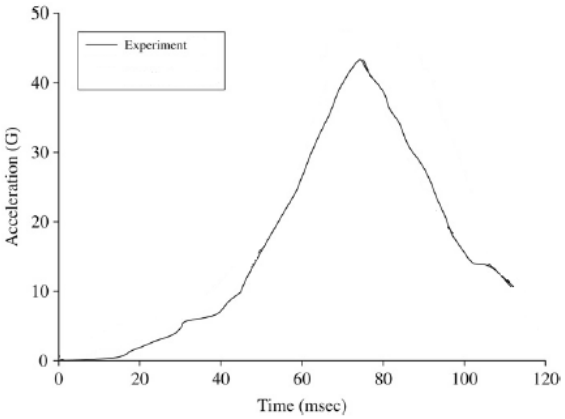


Experimental resultant upper torso acceleration (peak acceleration = 43.5 G) [57]

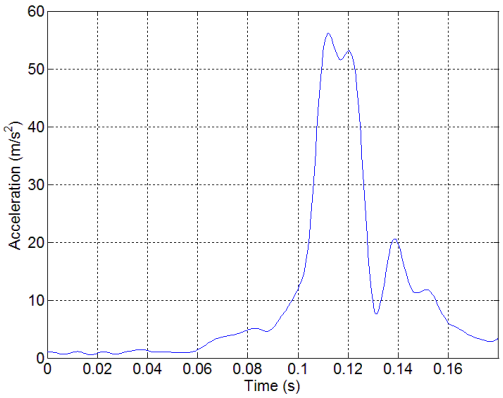


MSC Dytran / ATB resultant lower torso acceleration (peak acceleration = 56.2 G)

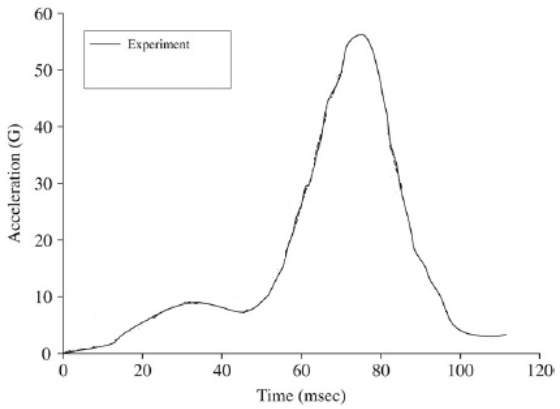


Experimental resultant lower torso acceleration (peak acceleration = 56.1 G) [57]

**Figure 52: Comparison of numerical model and experimental sled test acceleration results (filtered)**

The 50th percentile adult male Hybrid III ATD was developed for automotive testing and therefore was not designed for accurate response to vertical impacts as is experienced in the aircraft crash environment. In the aerospace industry, the Hybrid II ATD or the FAA Hybrid III ATD is commonly used; however only the Hybrid II is available in MSC Dytran. The Hybrid II ATD satisfies the requirements of 49 CFR Part 572 subpart B, and is suitable for use in design and certification, including the compression load between the pelvis and lumbar spine. Fasanella and Jackson [58] present an experimental drop test of a composite fuselage section with 50th percentile adult male Hybrid II ATDs. The experimental results were compared with predicted results developed with MSC Dytran and the integrated ATB code. Figure 53 shows a comparison between the predicted and experimental pelvis vertical accelerations. It can be seen that the predicted overall shape, pulse duration, and maximum acceleration are comparable with the experimental result. The maximum predicted acceleration was 24 G compared with 30 G measured experimentally.

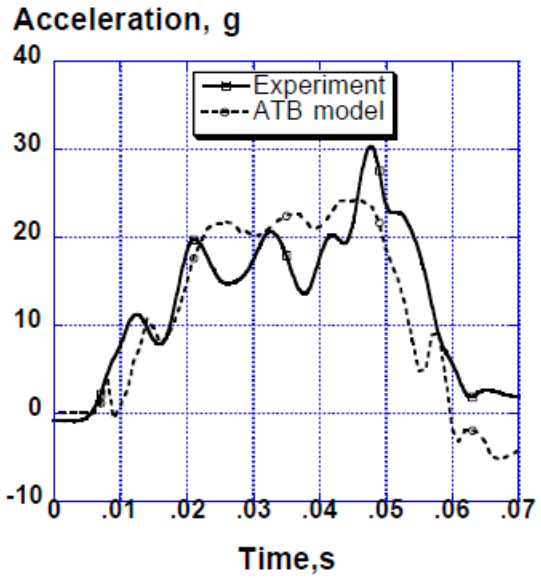


**Figure 53: MSC Dytran / ATB predicted pelvis vertical acceleration compared with experimental pelvis vertical acceleration for the 50th percentile Hybrid II ATD [58]**

### 2.2.9 Conclusions

The technique required to examine the dynamic response of an occupant with MSC Dytran, integrated with the Articulated Total Body (ATB) model, was demonstrated through the analysis of a sled test. The 50$^{th}$ percentile adult male (occupant of average height and mass) anthropomorphic test device (ATD) was used to replicate the human body response in the sled test. The ATB model was used to numerically represent the ATD.

The gross body motion results for the sled test, although essentially qualitative, appear reasonable and were comparable with the results presented by Gong et al. [56]. Resultant accelerations for the head, lower torso, and upper torso were compared with experimental results acquired from Teng et al. [57]. The trends of the accelerations were similar when comparing the numerical model results with the experimental results. The peak acceleration values were also in close agreement when comparing the numerical model results with the experimental results.

Based on the results obtained it was concluded that the technique employed to examine the dynamic response of an occupant is valid. Damage to biological tissues could not be predicted as the ATB model implemented in this study consists of rigid ellipsoids and is therefore non-deformable. Additionally, representation of the 50$^{th}$ percentile adult male Hybrid II ATD is recommended for future analyses as it satisfies the certification requirements of Federal Aviation Regulation (FAR) 23.562 subpart C for emergency landing dynamic conditions, unlike for the 50$^{th}$ percentile adult male Hybrid III ATD used in this study. This is because the compression load between the pelvis and lumbar spine resulting from vertical impacts is certifiable for the Hybrid II ATD, not the Hybrid III. The Federal Aviation Administration (FAA) Hybrid III may also be used for certification purposes; however it is currently not available in MSC Dytran. Although the Hybrid III ATD may not be

certifiable according to FAR 23.562 subpart C, the technique required to implement the various ATDs within MSC Dytran remains the same.

## 2.3 Soil impact analysis

### 2.3.1 Introduction

The crash dynamics of aircraft are dependent on the characteristics of the impact surface (refer to Chapter 1 Section 5). It is therefore important to consider impacts into both hard and soft terrains when assessing aircraft crashworthiness.

The work presented in this section aims to reduce the numerical instabilities commonly associated with Lagrangian-based finite element techniques by implementing an Eulerian-based finite element technique in MSC Dytran as an alternative for soft soil impact analyses. The effectiveness of the Eulerian-based finite element technique was determined through correlation of experimental penetrometer drop test results published by Fasanella et al. [59].

Similar studies performing dynamic finite element analyses of penetrometer drop tests into soil have previously been documented. Dynamic finite element analyses of free-falling penetrometers impacting into uniform clay were performed by Airey et al. [60], which may be used to evaluate mechanical properties of soil. The technique used was based on a time implicit based finite element code and an ALE approach. The penetrometer used in the paper by Airey et al. [60] was idealised as a rigid body. Seetamsetti [61] performed finite element analyses of penetrometer drop tests into soft soil as part of a validation study of soft soil properties. Time explicit based finite element codes were used and comparisons were performed between various

techniques namely; Lagrangian, ALE, and SPH. The penetrometers were idealised as rigid bodies, and penetrometer accelerations were output for comparative purposes. Note that in each study, different characterisation methods were used for soil definition, which is also true for this study.

### 2.3.2 Experimental data

Experimental data were acquired from previous work published by Fasanella et al. [59] of hemispherical penetrometer drop tests conducted at the Utah Test and Training Range (UTTR) as shown in Figure 54. Fourteen sets of experimental data are shown in Table 4 and were investigated to validate a constitutive soil model for impact analyses. Penetrometer diameter, mass, and impact velocity were varied during the experimentations.

**Figure 54: Post-test picture of 0.408m diameter penetrometer after 45m/s impact [59]**

**Table 4: Experimental data acquired from penetrometer drop tests performed at UTTR [59]**

| Data set | Diameter (m) | Mass (kg) | Impact velocity (m/s) | Experimental peak acceleration ($m/s^2$) |
|---|---|---|---|---|
| 1 | 0.203 | 2.98 | 5.74 | 833.85 |
| 2 | 0.408 | 12.05 | 34.97 | 11722.95 |
| 3 | 0.408 | 12.05 | 43.15 | 14538.42 |
| 4 | 0.408 | 12.05 | 44.9 | 16245.36 |
| 5 | 0.408 | 24.5 | 31.94 | 6023.34 |
| 6 | 0.408 | 24.5 | 39.42 | 7965.72 |
| 7 | 0.408 | 24.5 | 45.35 | 9966.96 |
| 8 | 0.514 | 11.02 | 16.7 | 4905 |
| 9 | 0.514 | 18.54 | 19.1 | 2943 |
| 10 | 0.514 | 18.91 | 16.7 | 2060.1 |
| 11 | 0.514 | 18.91 | 21.8 | 3188.25 |
| 12 | 0.514 | 18.91 | 25.9 | 5003.1 |
| 13 | 0.66 | 24.0 | 35 | 10594.8 |
| 14 | 0.66 | 24.0 | 40 | 12703.95 |

The nominal values for soil characterisation provided by Fasanella et al. [59] were as follows:

Elastic secant modulus (E) = 4 MPa

Poisson's ratio ($\nu$) = 0.3

Deviatoric yield stress or bearing pressure ($\sigma_y$) = 68.9 kPa

Density ($\rho$) = 2201.6 $kg/m^3$

Hardening modulus (EH) = 800 kPa (20% of E)

These parameters were approximate; however they were used as a basis for the work performed in this study due to a lack of available data. The test method used to characterise the soil was unknown; however a triaxial compression test methodology with a biaxial stress state was assumed, where $\sigma_1>\sigma_2=\sigma_3$ (major, intermediate, and minor principal stresses respectively). The triaxial compression test was assumed as it is the most

widely used methodology for investigating the strength and deformation behaviour of soils [62].

### 2.3.3 Soil characterisation

Generally, soils are non-homogenous, anisotropic and have non-linear stress-strain relationships. For analysis simplification purposes, the soil was assumed to be isotropic and to have elastic perfectly-plastic behaviour as shown in Figure 55. Idealisation of the stress-strain relationships with linear elastic theory was discussed by Craig [63] and was found to be a valid approach. It must be noted that in reality, varying soil properties are observed through the depth range; however this variation in properties was not considered due to a lack of available data.

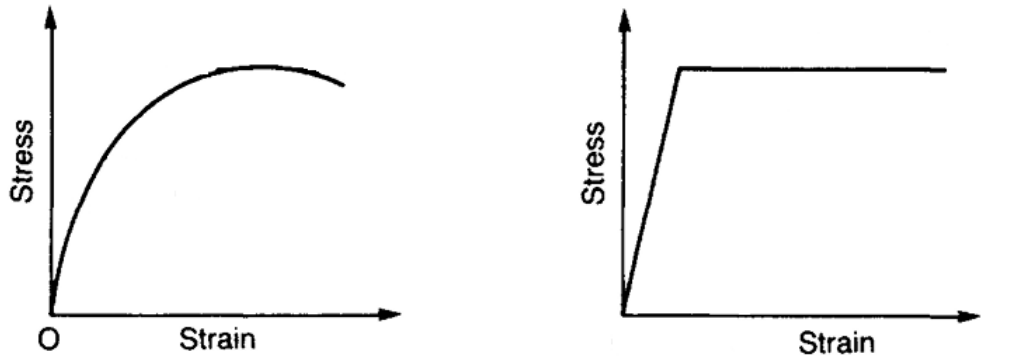


Actual non-linear soil relationship

Ideal elastic perfectly plastic soil representation

**Figure 55: Soil stress-strain relationships [63]**

A Mohr-Coulomb failure criterion was used to describe the conditions for which an isotropic material will fail [64]. Generally, the intermediate principal stress ($\sigma_2$) is equal to the minor principal stress ($\sigma_3$) due to the method of testing soils (i.e. biaxial stress state); therefore the intermediate principal stress was neglected. The Mohr-Coulomb failure criterion considers that the

shear stress of soil increases with an increase in mean normal stress as shown in Figure 56. Figure 56 also indicates that if a number of stress states are known, which produce shear failure of the soil, the Mohr-Coulomb failure criterion assumes that a common tangent can be drawn to the Mohr circles [63]. This common tangent is the failure envelope of the soil and is represented by:

$$\tau = c + \sigma . tan\varphi \tag{73}$$

where:

$\tau$ = shear stress on a failure plane
$c$ = cohesive shear strength
$\sigma$ = normal stress on a plane
$\varphi$ = angle of shearing resistance or angle of internal friction

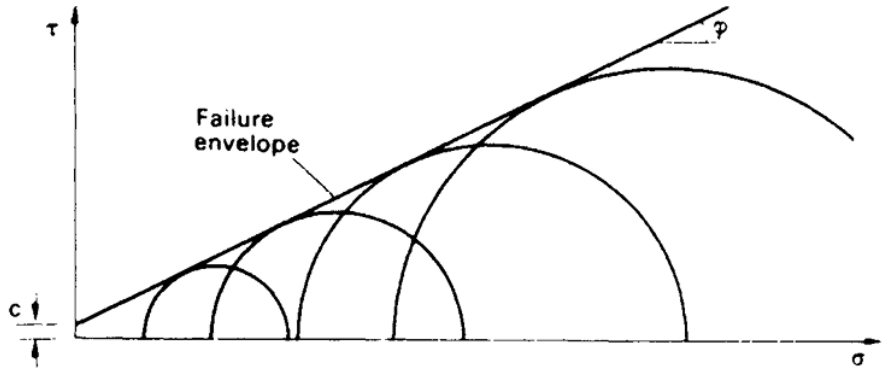


**Figure 56: Mohr-Coulomb failure criterion indicating an increase of shear stress with an increase of mean normal stress [63]**

Equation 73 and Figure 57 represent a material showing both friction (of soil particles along slip planes) and cohesion. The Mohr's circles are constructed with a positive convention for compression and $\sigma_1 > \sigma_3$.

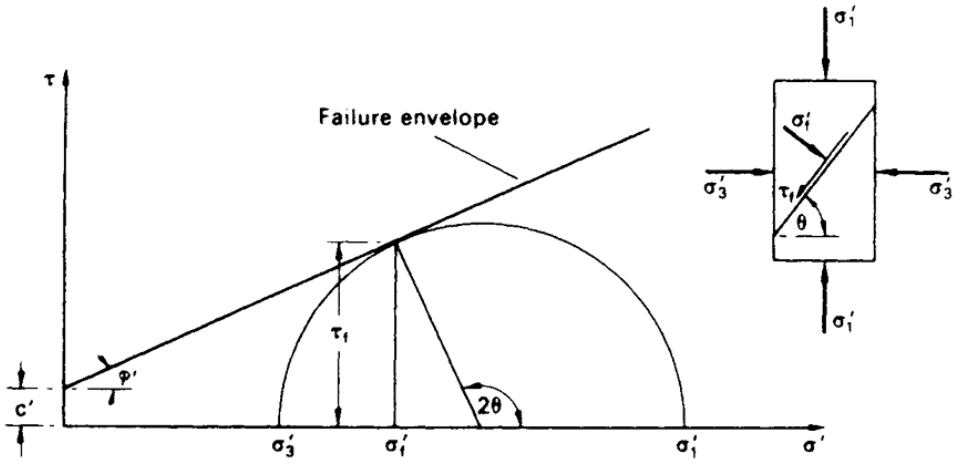


**Figure 57: General Mohr-Coulomb failure criterion representative of a material showing both friction and cohesion [63]**

The soil was assumed to be fully saturated, meaning that it consisted of only solid soil particles and water (no air was present). The inputs for the Mohr-Coulomb failure criterion are usually in terms of effective stresses (σ') for fully saturated soils. Figure 58 represents the different stress components in soil. The effective stress represents the stress component carried by the contact forces between soil particles (i.e. the stress transmitted through the soil "skeleton"). Pore water pressure (μ) is the pressure of water filling the void spaces between the solid soil particles. The total stress (σ) is equal to the sum of the pore water pressure and effective stress as shown in Equation 74.

$$\sigma = \mu + \sigma' \qquad (74)$$

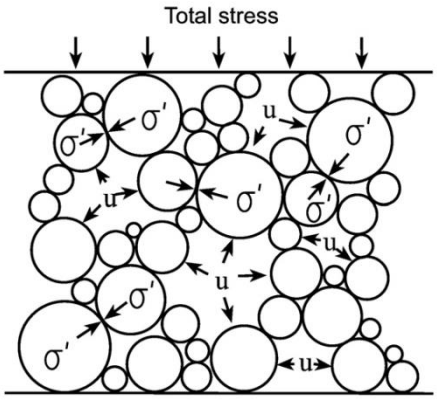


**Figure 58: Representation of soil stress components [65]**

To further characterise the soil, the individual soil particles and water were assumed to be incompressible, and the lateral strain of the soil was assumed to be negligible when subjected to an increase in vertical stress. Furthermore, the consolidation process must be understood. Consolidation refers to the reduction in volume of a fully saturated soil due to the drainage of some of the pore water. Consolidation occurs until all the excess pore water pressure has dissipated, where the excess pore water pressure was a result of an increase in total stress. A simple analogy is shown in Figure 59, which is used to describe the consolidation process. Figure 59 (a) shows a rigid cylinder filled with water, a piston with a closed valve, and a spring. The rigid cylinder represents negligible lateral strain, the water represents the pore water in the soil, the spring represents the solid soil particles, and the closed valve represents an undrained condition. An unconsolidated-undrained condition is shown in Figure 59 (b), where an increase in vertical stress results in an equal increase in pore water pressure (resulting in excess pore water pressure) only as the piston cannot move due to the incompressibility of water. The effective stress is therefore constant (i.e. the stress in the spring remains unchanged). Alternatively, in Figure 59 (c), the open valve results in drainage of excess pore water pressure and the load is also transmitted to the spring. A consolidated condition is shown in Figure 59 (d) where the excess pore water pressure has been fully dissipated and the

load is resisted by the spring only. Figure 59 (d) also represents a drained condition, meaning that there is no excess pore water pressure. It must be noted that the soil remains fully saturated throughout the process, even when in the drained condition.

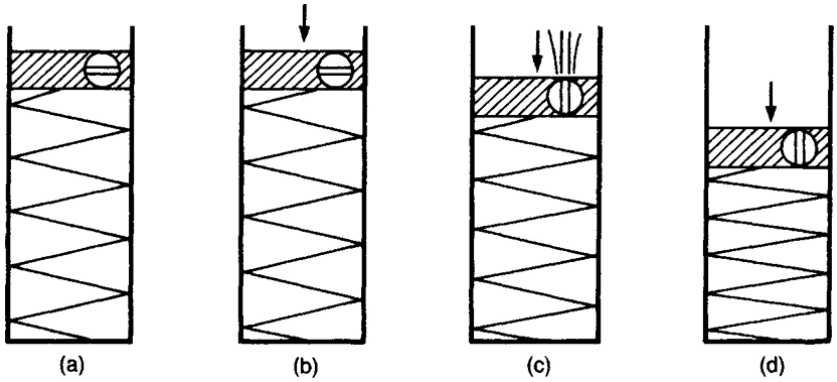


**Figure 59: Consolidation analogy [63]**

The rate of change in total stress was assumed to be much greater than the rate of dissipation of excess pore water pressure in impact conditions; therefore, an unconsolidated-undrained condition was deemed applicable for impact analyses as represented in Figure 59 (b) [63]. The resulting Mohr-Coulomb failure criterion was equivalent to the Tresca (maximum shear stress) failure criterion as shown in Figure 60, because an increase in total stress resulted in an equal increase in pore water pressure (i.e. the stress difference remained constant). The results were in terms of total stress with a horizontal failure envelope (i.e. $\varphi=0^{o}$) and the shear strength being equal to cohesion strength. Soil fails in shear when it is loaded in compression; therefore, the Mohr-Coulomb failure criterion agrees with the Tresca failure criterion [66]. The Mohr-Coulomb failure criterion is applicable for materials with much greater uniaxial compressive strength compared to uniaxial tensile strength [64].

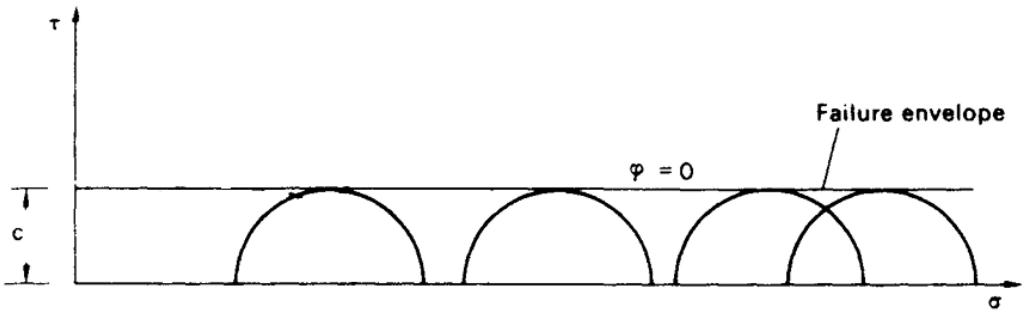


**Figure 60: Unconsolidated-undrained triaxial test results for saturated clay [63]**

### 2.3.4 Soil numerical model

A Mohr-Coulomb failure criterion, equivalent to a Tresca (maximum shear stress) failure criterion, was used to describe soil behaviour, as an alternative method to that used by Fasanella et al. [59]. The material parameters used to define the soil were: density ($\rho$); bulk modulus (K); shear modulus (G); deviatoric yield stress ($\sigma_y$); cohesion strength (c); and angle of shearing resistance ($\varphi$). MSC Dytran's representation of the Mohr-Coulomb yield model is shown in Figure 61, where Y1, Y2, and Y3 are the deviatoric yield stress, cohesion strength, and tangent function of the angle of shearing resistance ($\tan\varphi$) parameters respectively.

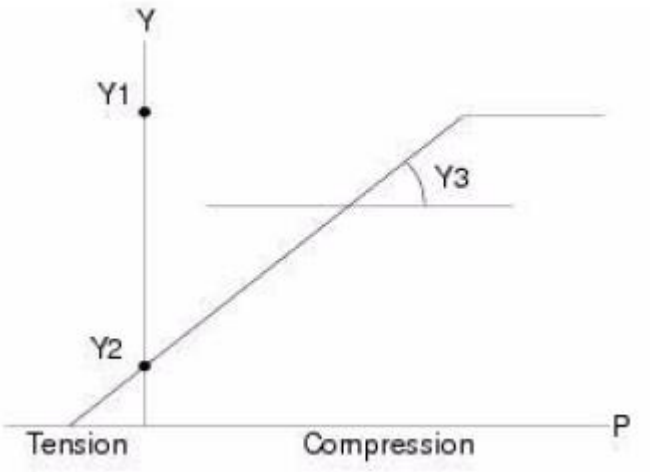


**Figure 61: MSC Dytran representation of the Mohr-Coulomb yield model [54]**

The deviatoric yield stress depends on the pressure as follows:

$$\sigma_y = \min(Y1, (Y2 + Y3 \times P)) \tag{75}$$

The soil was assumed to obey Hooke's law in the linear elastic region, therefore the shear modulus and bulk modulus were calculated from the modulus of elasticity (E) and Poisson's ratio ($\nu$) provided by Fasanella et al. [59]. The relationships are as follows:

$$G = \frac{E}{2(1+v)} \tag{76}$$

$$K = \frac{E}{3(1-2v)} \tag{77}$$

The resulting parameters used for the soil models were:

Density ($\rho$) = 2201.6 kg/m$^3$

Bulk modulus (K) = 3.333 MPa

Shear modulus (G) = 1.538 MPa

Deviatoric yield stress ($\sigma_y$), Y1 = 68.9 kPa
Cohesion strength (c), Y2 = 68.9 kPa
Tangent of the angle of shearing resistance ($\tan\varphi$), Y3 = 0

The Mohr-Coulomb failure criterion defined by Y1 equal to Y2, and Y3 equal to zero is equivalent to a Tresca failure criterion as previously shown in Figure 60.

A typical finite element mesh is shown in Figure 62. A void region was created above the soil to allow the penetrometer to be coupled to the Euler domain without initial contact with the soil, and to also allow the soil to displace into the void region. The use of the void region was based on the assumption that the effect of air was negligible. At the interface between the void and soil regions, a transition of colours appears in Figure 62. This was due to post-processing (i.e. interpolation of values) and may be ignored. The dimensions of the soil region were approximately eight times the penetrometer radius each side to ensure stress wave reflections at the edges of the Euler domain have a negligible effect on analyses results. Clarke and Shen [5] determined that the size of the Euler element edge length should be similar in size to that of the coupling surface element edge length for rotorcraft water impact analyses. The sizing of the Euler element edge lengths in this paper were based on the same determination as found by Clarke and Shen [5]; however, a bias was applied to the mesh for computational efficiency by reducing the number of elements. A simple convergence test was carried out for data set 14 to confirm this sizing approach. The results of this convergence test are shown in Table 5; however, convergence of results was not evident. An additional consideration to be taken into account regarding the Euler element size may be seen in the work performed by Fasanella et al. [7]. It was found that with large Euler elements (relative to the Lagrange elements), flow of water was not captured through failed Lagrangian elements at the ALE interface. When considering

time, accuracy, and element failure at the coupling surface (as is applicable in crashworthiness analyses), it is also recommended that the Euler element edge length be the same size of the Lagrangian element edge length at the coupling surface as per Clarke and Shen's [5] recommendation. The peak acceleration results in Table 5 were filtered with a low pass digital Butterworth filter as explained in Chapter 2 Section 3.6. A computer with two Intel(R) Core(TM) i7-4790K (4.0 GHz) central processing units, and 32 gigabytes random-access memory, was used for analyses.

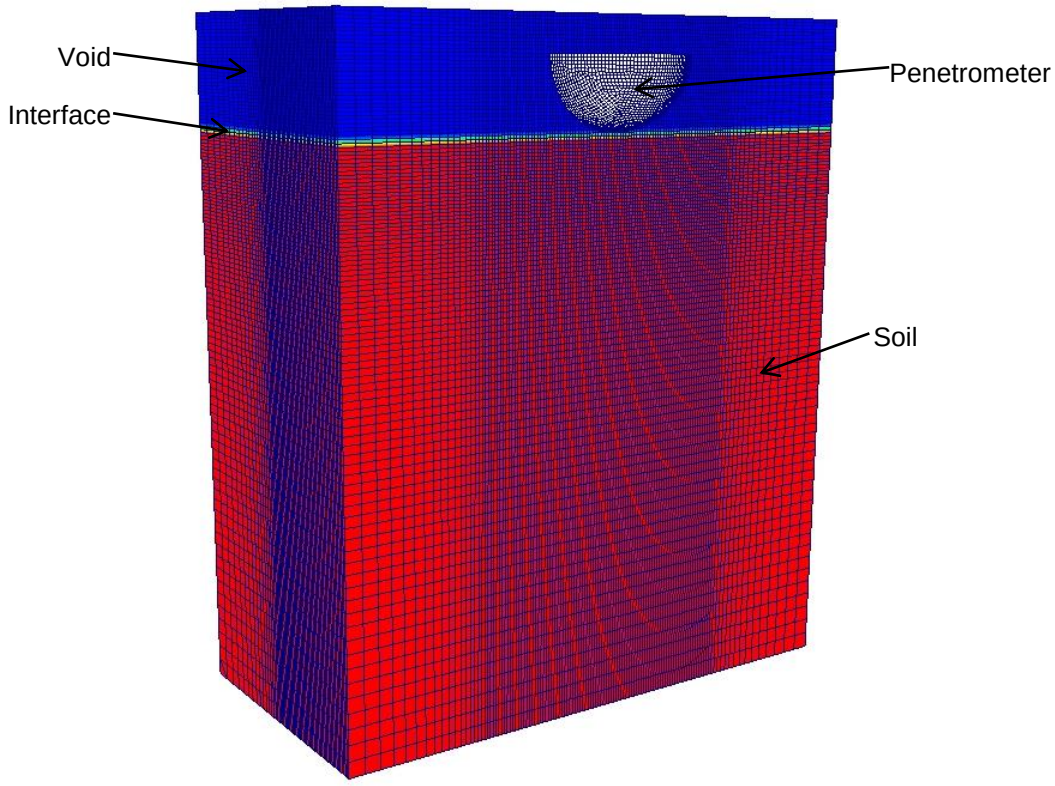


**Figure 62: Finite element mesh showing the penetrometer and the soil and void domains (a slice through the centre of the Euler domain is shown for clarity)**

**Table 5: Convergence test of data set 14 to determine Euler element size**

| | | | | | |
|---|---|---|---|---|---|
| Euler element edge length (m) at point of impact | 0.01 | 0.015 | 0.02 | 0.025 | 0.03 |
| Lagrange element edge length (m) at point of impact | 0.015 | 0.015 | 0.015 | 0.015 | 0.015 |
| Total number of Euler elements in model | 5763576 | 1670400 | 696600 | 347829 | 205200 |
| Total number of Lagrange elements in model | 5167 | 5167 | 5167 | 5167 | 5167 |
| Model penetrometer peak acceleration ($m/s^2$) - filtered as per Chapter 2 Section 3.6 | 13340 | 11740 | 13730 | 13410 | 12440 |
| Error (%) | 5.01 | 7.59 | 8.08 | 5.56 | 2.08 |
| Analysis time | 3 hr 22 min | 51 min | 19 min | 10 min | 6 min |

Additional parameters applied to the soil model were spallation, a hydrostatic preset, cohesive friction, maximum velocity in the Eulerian mesh, and an artificial bulk viscosity. The spallation model defines a constant minimum pressure prior to spallation, with a positive sign convention for compression. If the pressure in an element falls below the minimum pressure, the element will spall and the pressure and yield stress are set to zero. A spallation pressure of negative atmospheric pressure (-101.35 kPa) was assumed in this paper to allow the soil to have a small amount of tensile strength prior to spallation. Soil behaviour also depends on the polynomial equation of state represented by Equation 78 [34], where the pressure is dependent on the bulk modulus, density and specific internal energy of the soil. The specific internal energy of the soil was assumed to be zero; therefore, a small increase in tensile pressure would result in spallation. The hydrostatic preset changes the density of the soil in the gravitational direction, in order to conform to a hydrostatic profile represented by Equation 79. The hydrostatic preset was set to atmospheric pressure (101.35 kPa) at the free surface of

the soil and ensured that an initial compressive pressure state existed in the soil, thereby avoiding spallation with only a small increase in tensile pressure.

In compression ($\mu > 0$): (78)

$$p = a_1\mu + a_2\mu^2 + a_3\mu^3 + \left(b_0 + b_{1\mu} + b_2\mu^2 + b_3\mu^3\right)\rho_o e$$

In tension ($\mu \leq 0$):

$$p = a_1\mu + (b_0 + b_1\mu)\rho_o e$$

where:

$p$ = pressure (Pa)
$a$ = coefficients ($a_1$= bulk modulus (Pa))
$b$ = coefficients
$\mu$ = ($\rho$ / $\rho_o$) -1
$\rho$ = overall material density (kg/m$^3$)
$\rho_o$ = reference density (kg/m$^3$)
$e$ = specific internal energy (J/kg)

$$p = \rho g h \quad (79)$$

where:

$p$ = pressure (Pa)
$\rho$ = density (kg/m$^3$)
$g$ = gravitational acceleration (m/s$^2$)
$h$ = height or depth (m)

Cohesive friction was used to allow for friction and sticking of the soil during tensile conditions at the coupling surface; whereas the Coulomb friction model was used for compressive conditions at the coupling surface. The static friction coefficient, the kinetic friction coefficient, and the exponential

decay coefficient were all assumed to be equal to one for the Coulomb friction law represented by Equation 80. For cohesive friction, the maximum normal tensile stress was assumed to be 80 gigapascals, which allows for tensile stresses at the coupling surface if the maximum normal stress is not exceeded. Additionally, for cohesive friction, a viscous-like friction law was used to specify a friction stress that was linear in the relative tangential velocity direction between the soil and coupling surface as represented by Equation 81. The friction stress was assumed to be 800 kilopascals and the reference velocity was assumed to be 2 metres per second. The assumed values were taken from reference [55] and were by no means assumed to be correct for the soil represented in this study. For simple penetrometer drop tests where the impact was orthogonal, the effect of cohesion was negligible. Cohesion was however introduced in this study because it was found to have a significant effect when impacts occur at oblique angles, which is typical of aircraft crashes. Experimentation would be required to obtain correct cohesive input values.

$$f = f_k + (f_s - f_k).e^{-\beta.v} \tag{80}$$

where:

$f$ = friction coefficient
$f_s$ = static friction coefficient
$f_k$ = kinetic friction coefficient
$\beta$ = exponential decay coefficient
$v$ = relative sliding at the point of contact

$$\tau = \tau_{fric}.min\left(1, \frac{v_{rel.tang}}{v_{ref}}\right) \tag{81}$$

where:

$\tau$ = shear stress (Pa)

$\tau_{fric}$ = friction stress (Pa)

$v_{rel.tang}$ = relative tangential velocity (m/s)

$v_{ref}$ = reference velocity (m/s)

A maximum velocity of 150 metres per second was assumed for the Eulerian soil, which was defined with the VELMAX parameter within MSC Dytran. This parameter was introduced for stability reasons when performing crashworthiness analyses, and had negligible effect on the penetrometer drop test results presented. The maximum velocity parameter was configured to not remove the mass in the Eulerian elements in which the velocity exceeds the maximum specified velocity. Further mention of the VELMAX parameter is made in Chapter 2 Section 5.6 and Chapter 3 Section 5.

The penetrometer drop tests were analysed with and without the addition of an artificial linear bulk viscosity coefficient ($C_L$). This coefficient was introduced to hopefully artificially improve results and was assumed to be equal to one when introduced into the models (by default it was equal to zero). Artificial viscosity, also referred to as artificial dissipation, is used to reduce oscillations typical of second-order approximations in the FEM because in the presence of steep gradients, numerical solutions of flow problems based on central difference approximations (as used in the explicit method) tend to oscillate. An example of where artificial viscosity may be applicable is for supersonic flow problems with shocks [27].

### 2.3.5 Penetrometer numerical model

Each hemispherical penetrometer (as shown in Figure 62) was configured as a rigid body. For accurate geometrical representation, the finite element discretisation consisted of shell elements with 5, 10, and 15 millimetre element edge lengths for data set 1, data sets 2-14, and data sets 13 and 14

respectively. The penetrometer was required to be a closed volume for coupling with the Euler domain.

### 2.3.6 Numerical results and discussion

Comparisons of experimental peak accelerations and numerical peak accelerations are shown in Table 6, with and without the artificial linear bulk viscosity coefficient ($C_L$). The experimental details are repeated in Table 6 to assist in easily identifying any trends or patterns associated with the results. The numerical acceleration results were filtered in Matlab using a low pass digital Butterworth filter with zero phase distortion. The filter order for all data sets was set to 2. The normalised cut-off frequency was set to 0.3 for all data sets except for data set 1, which was set to 0.1. A fast Fourier transform was used to determine the main frequency components, thereby enabling the selection of suitable cut-off frequencies. Refer to Appendix A for further details regarding the low-pass digital Butterworth filter and fast Fourier transform.

Without the artificial linear bulk viscosity coefficient ($C_L = 0$ ), the majority of acceleration results showed good correspondence with the experimental peak acceleration results, except for data sets 9-12. It was noted that the predicted acceleration results for data sets 9-12 showed relatively poor correspondence and were conservative (i.e. over-predicted the peak accelerations). Additionally, these data sets all had the same penetrometer diameter and similar mass. After the artificial linear bulk viscosity coefficient was introduced ($C_L = 1$), the acceleration results for data sets 9-12 improved by up to 62.41% (data set 12). It was noted that whilst these results improved, the accuracy of various other results decreased. This was especially evident from data set 6 where the percentage error increased from 6.36% to 17.37%. It was therefore evident that the artificial linear bulk viscosity coefficient has a significant effect on results. Further investigation of

this coefficient and its effects is required, or preferably, this coefficient should be discarded and the soil definition should be investigated further on a phenomenological level.

**Table 6: Comparison of experimental and numerical peak acceleration results for penetrometer impact into soft soil**

| Data set | Diameter (m) | Mass (kg) | Impact velocity (m/s) | Exp. peak accel. ($m/s^2$) | Num. peak accel. ($m/s^2$) $C_L = 0$ | Error (%) $C_L = 0$ | Num. peak accel. ($m/s^2$) $C_L = 1$ | Error (%) $C_L = 1$ |
|---|---|---|---|---|---|---|---|---|
| 1 | 0.203 | 2.98 | 5.74 | 833.85 | 890.4 | 6.78 | 883.6 | 5.97 |
| 2 | 0.408 | 12.05 | 34.97 | 11722.95 | 10090 | 13.93 | 8714 | 25.67 |
| 3 | 0.408 | 12.05 | 43.15 | 14538.42 | 13610 | 6.39 | 12620 | 13.20 |
| 4 | 0.408 | 12.05 | 44.9 | 16245.36 | 14500 | 10.74 | 14730 | 9.33 |
| 5 | 0.408 | 24.5 | 31.94 | 6023.34 | 5341 | 11.33 | 4781 | 20.63 |
| 6 | 0.408 | 24.5 | 39.42 | 7965.72 | 7459 | 6.36 | 6582 | 17.37 |
| 7 | 0.408 | 24.5 | 45.35 | 9966.96 | 9259 | 7.10 | 8187 | 17.86 |
| 8 | 0.514 | 11.02 | 16.7 | 4905 | 4314 | 12.05 | 3968 | 19.10 |
| 9 | 0.514 | 18.54 | 19.1 | 2943 | 3670 | 24.70 | 3354 | 13.97 |
| 10 | 0.514 | 18.91 | 16.7 | 2060.1 | 2851 | 38.39 | 2712 | 31.64 |
| 11 | 0.514 | 18.91 | 21.8 | 3188.25 | 4465 | 40.05 | 4199 | 31.70 |
| 12 | 0.514 | 18.91 | 25.9 | 5003.1 | 6005 | 20.03 | 5380 | 7.53 |
| 13 | 0.66 | 24.0 | 35 | 10594.8 | 9694 | 8.50 | 10020 | 5.43 |
| 14 | 0.66 | 24.0 | 40 | 12703.95 | 11740 | 7.59 | 12610 | 0.74 |

Typical displacement and velocity plots are shown in Figure 63, which show that there was no appreciable rebound of the penetrometer. This was in agreement with Sareen et al. [51] and Fasanella et al. [67] who showed that drops into soft soil do not exhibit appreciable rebound. The velocity plot also shows that the soil dissipated energy through plastic deformation ("plastic kink" shown in the plot) and that all of the penetrometer's kinetic energy was effectively dissipated. Material fraction iso-surface plots of the displaced soil are shown in Figure 63 and Figure 64. The iso-surface plots, although

essentially qualitative, were comparable to Figure 54 (post-test picture) and show that soil displacement behaviour was reasonable and cratering occurred. Spallation was also observed at high impact loads as is highlighted in Figure 64.

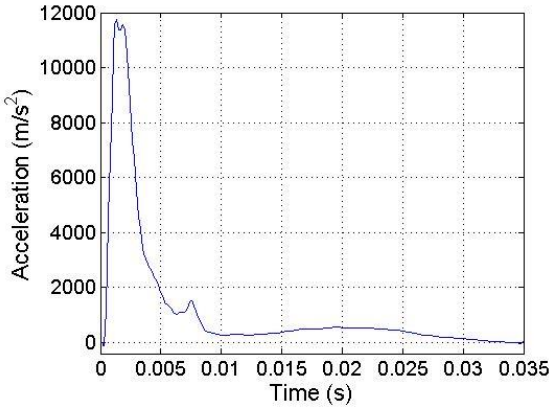


Penetrometer acceleration - time plot

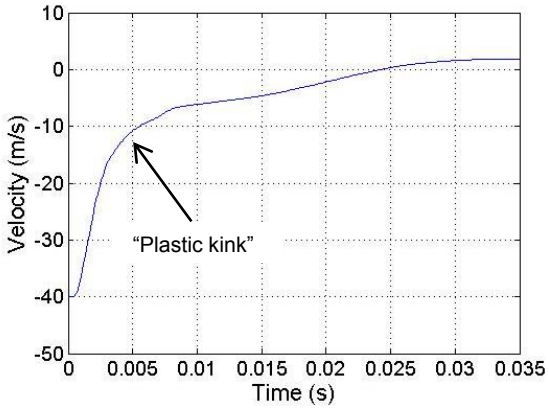


Penetrometer velocity - time plot

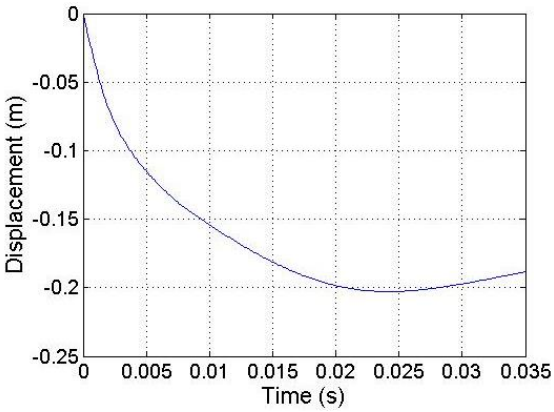


Penetrometer displacement - time plot

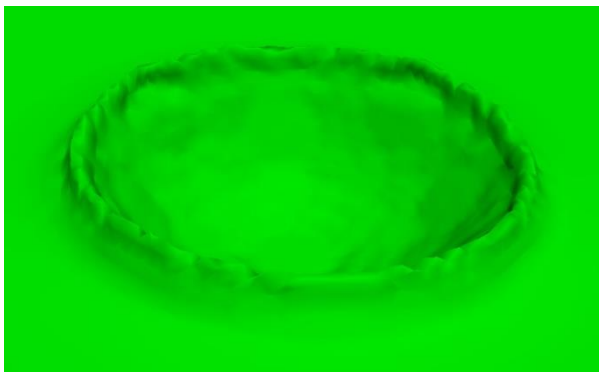

Soil material fraction iso-surface plot

**Figure 63: Numerical results obtained for data set 14, showing the typical response of a penetrometer drop test**

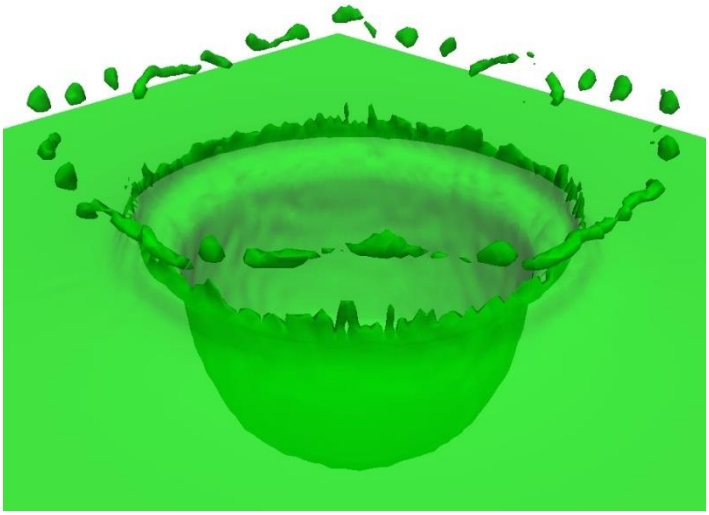

**Figure 64: Soil material fraction iso-surface plot for data set 7, showing cratering and spallation (opacity used for clarity)**

A comparison of experimental and numerical acceleration plots for data sets 2, 4, 13 and 14 is shown in Figure 65. As can be seen, the onset rate of accelerations compared well; however, the drop-off rates differed. The numerical result had a higher drop-off rate than the experimental result, and was the case for all data sets. A hardening effect of the soil as penetration depth increased was not defined, and it is believed that this is the reason for the difference in drop-off rates. Further investigation is required regarding the significance of the difference in drop-off rates for crashworthiness applications as, for example, human tolerance levels depend largely on the duration of acceleration.

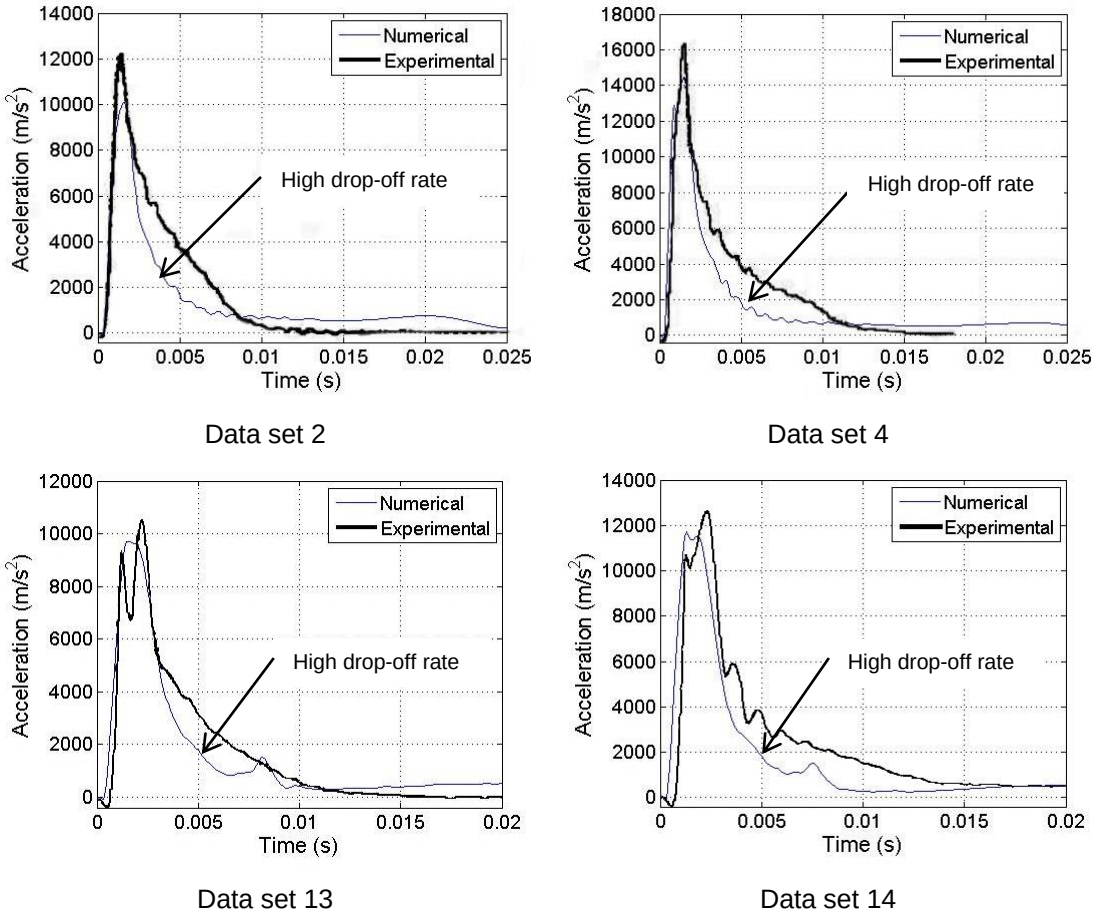


**Figure 65: Experimental [59] and numerical penetrometer acceleration response for data sets 2, 4, 13 and 14 showing typical difference in drop-off rates**

Generally, it is difficult to determine the reason for numerical inaccuracies without further information regarding the drop test methodology, varying soil properties through the depth range, and strain rate effects. For example, the drop test methodology could describe the penetrometer structure. This is important as the energy absorption characteristics of the penetrometer may be significant. Knowledge of the soil properties through the depth range may allow for the inclusion of different layers of soil with varying mechanical properties. According to Nazem et al. [60], “the undrained shear strength of cohesive soils often increases with the rate of straining”. When compared to the Lagrangian-based finite element technique implemented by Fasanella et

al. [59], various advantages were observed with the Eulerian-based finite element technique. Numerical instability was of less concern and no complex contact input parameters were required. Numerical instability with the Lagrangian-based finite element technique is of major concern, especially when using rigid body properties and when large deformations occur.

### 2.3.7 Conclusions

An Eulerian-based finite element technique was implemented for soft soil impact analyses and its effectiveness was determined through correlation of fourteen sets of experimental hemispherical penetrometer drop test results published by Fasanella et al. [59]. The experimental parameters varied were the penetrometer mass, diameter, and impact velocity.

The Eulerian solver was coupled with the Lagrangian solver to enable interaction between the penetrometer (Lagrangian structure) and soil (Eulerian material). A Mohr-Coulomb failure criterion, equivalent to a Tresca (maximum shear stress) failure criterion, was used to describe soil behaviour, whilst the penetrometers were configured as rigid bodies. Penetrometer accelerations were compared with experimental data published by Fasanella et al. [59]. Penetrometer velocity plots, penetrometer displacement plots, and material fraction iso-surface plots of the soil were also investigated to determine model fidelity.

The majority of the penetrometer drop test results showed good correspondence with the experimental peak acceleration results as recorded by Fasanella et al. [59], except for four anomalous results with relatively low impact velocities (i.e. 19.1-25.9 m/s). After the addition of an artificial linear bulk viscosity coefficient, the acceleration results for these four anomalous results improved, whilst the accuracy of various other results with relatively high impact velocities (i.e. 31.94-45.35 m/s) generally decreased (note that

this was the case for the majority of drop tests, not all). It was therefore evident that the artificial linear bulk viscosity coefficient has a significant effect on results. Further investigation of this coefficient and its effects is required, or preferably, this coefficient should be discarded and the soil definition should be investigated further on a phenomenological level. The velocity and displacement plots showed that there was no appreciable rebound and that the soil dissipates energy through plastic deformation. The rebound and deformation responses agreed with previously published literature [51, 67]. The iso-surface plots, although essentially qualitative, showed that soil displacement behaviour was reasonable and cratering occurred. The numerical and experimental acceleration plots showed a difference in drop-off rates. Further investigation is required regarding the significance of the difference in drop-off rates for crashworthiness applications.

Based on the results obtained it was concluded that an Eulerian-based approach to soft soil impact analysis, for crashworthiness applications, is valid. Greater model fidelity may possibly be gained by further investigation of the drop test methodology, viscosity effects, variation of soil mechanical properties through the depth range, and strain rate effects.

## 2.4 Composite materials analysis

### 2.4.1 Introduction

Laminates subjected to various loading conditions may still have a load carrying capacity beyond first-ply failure. An investigation into the performance of the Tsai-Wu failure criterion to capture the onset and progression of failure through the layers of fibre reinforced composite laminates was conducted with the implementation of MSC Dytran. An

impulsively loaded unidirectional composite laminate strip model, similar to the aluminium “Impulsively Loaded Strip” model found in MSC Dytran’s 2012 Example Problem Manual [55], was used for the investigation.

The purpose of such an investigation was ultimately to verify the implementation of the Tsai-Wu failure criterion within MSC Dytran. Since this study focuses on the ability of the Tsai-Wu failure criterion to capture the onset and progression of failure through the laminate layers, assumptions are stated in the text that follows regarding the overall material response and are believed to hold true. These assumptions provide justification for the implementation of the Tsai-Wu failure criterion in aircraft crashworthiness analyses.

### 2.4.2 Failure criterion selection

A Tsai-Wu failure criterion was selected for prediction of deformation and failure response of composite laminates used in this study. Soden et al. [68] quantitatively ranked the Tsai-Wu criterion as one of the five leading failure theories. The other four failure theories, namely Zinoviev, Bogetti, Puck, and Cuntze were not considered as they are currently not implemented within MSC Dytran. The Tsai-Wu criterion assumes linear elastic material properties and reduced matrix stiffness after initial failure. It predicts the onset of failure, but does not explicitly identify the failure mode. Increases in strength and stiffness of laminates may be observed at high strain rates; however were not considered.

Every failure criterion has its strengths and weaknesses; therefore careful consideration of the loading conditions is required when selecting an appropriate failure criterion. It became apparent during this study that the Tsai-Wu failure criterion over-predicts the strength of laminates in the compression-compression quadrant (refer to Figure 16 and Figure 17). As

stated in Chapter 1 Section 5, the majority of aircraft nose down impacts experience a rapid change in aircraft pitch. This change in aircraft pitch produces bending moments in the fuselage, which will result in compressive or tensile stresses along the length of the fuselage. Additional fuselage compressive stresses due to longitudinal impact forces may be added to the bending stresses along the length of the fuselage. It was therefore assumed that the applied stresses are uniaxial (along the length of the fuselage) and a biaxial compression-compression loading condition may be ignored. This assumption was also deemed applicable for the impulsively loaded unidirectional composite laminate strip presented below. The loading conditions for the impulsively loaded unidirectional composite laminate strip are therefore deemed representative of the expected loading conditions for the aircraft's composite fuselage in a crash event. In general, the Tsai-Wu failure criterion accurately predicts the deformation of laminates at low strains, as is expected for fibre-dominated laminates. Laminate deformation was therefore assumed to be reasonably accurate as only fibre-dominated layups were used throughout this study (refer to Figure 18 and Figure 19).

### 2.4.3 Model setup

A symmetric half model was used for the investigation for computational efficiency as shown in Figure 66 and Figure 67. The laminate strip was fully constrained (i.e. all six degrees of freedom constrained) on its left edge, whilst a symmetry constraint (i.e. translation along z-axis and rotation about x and y-axes were constrained) was applied at its right edge. Figure 67 shows the initial velocity distribution applied along the width of the laminate strip.

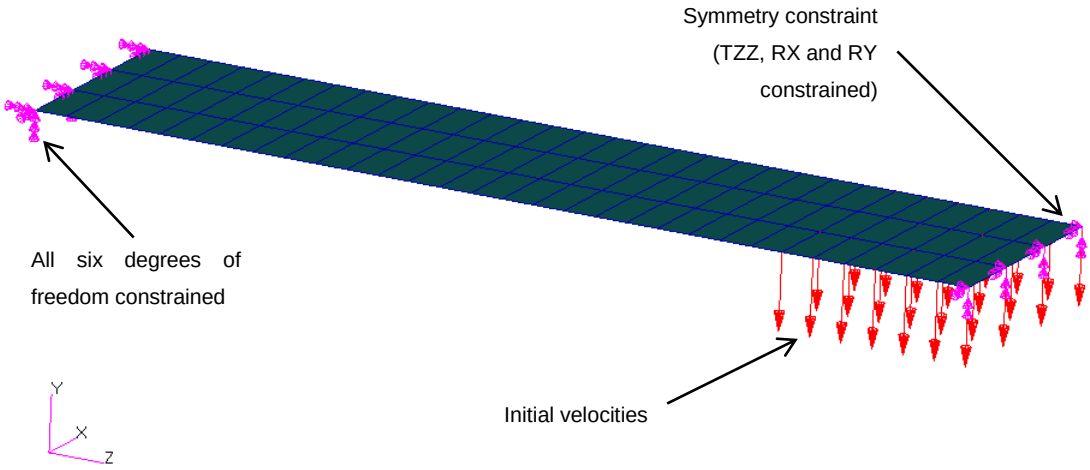


**Figure 66: Impulsively loaded unidirectional composite laminate strip model setup**

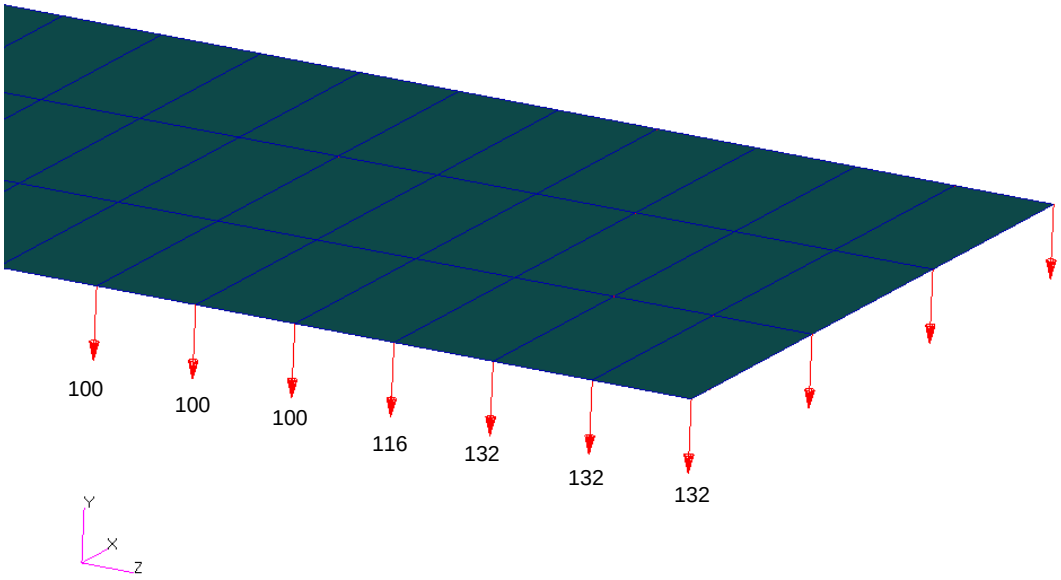


**Figure 67: Impulsively loaded unidirectional composite laminate strip model setup showing the initial velocities (m/s) each applied to the width of the strip (along x-axis)**

Four-node quadrilateral shell elements were used to model the unidirectional composite laminate strip. A Key-Hoff element formulation was assigned to

the shell elements. The PCOMP and PCOMPA cards within MSC Dytran were used to define laminate properties, such as lamina orientation and thickness. The total laminate thickness was 3.176mm and consisted of eight equal thickness laminae. The MAT8 and MAT8A cards within MSC Dytran were used to define the orthotropic material properties and failure properties. The lamina properties used for the investigation are shown in Table 7.

**Table 7: Mechanical properties of unidirectional laminae for the impulsively loaded composite laminate strip model**

| | |
|---|---|
| Density, $\rho$ (kg/m$^3$) | 1540 |
| Longitudinal modulus, $E_{11}$ (GPa) | 118 |
| Transverse modulus, $E_{22}$ (GPa) | 8.2 |
| Poisson's ratio, $\nu_{12}$ | 0.34 |
| Shear modulus, $G_{12}$ (GPa) | 4.07 |
| Shear modulus, $G_{13}$ (GPa) | 4.07 |
| Shear modulus, $G_{23}$ (GPa) | 4.07 |
| Shear strength, $S_{12}$ (MPa) | 83.6 |
| Longitudinal tensile strength, $X_T$ (MPa) | 2459 |
| Longitudinal compressive strength, $X_C$ (MPa) | 1102 |
| Transverse tensile strength, $Y_T$ (MPa) | 500 |
| Transverse compressive strength, $Y_C$ (MPa) | 500 |

The upper layers in this model were numbered one to four and the lower layers were numbered five to eight; however MSC Dytran designates the layers by sequentially numbering them starting from one at the bottom layer. The reason for the upper layer starting with designation one in the model presented here was that the element normal pointed downwards in the negative y-direction (refer to the coordinate system shown in Figure 66).

### 2.4.4 Results and discussion

When a particular failure criterion is satisfied, the material fails and can no longer sustain its loading. In MSC Dytran, the element where the material reaches its failure limit cannot carry stresses anymore. The stress tensor is therefore effectively zero. The element is flagged for failure and is essentially no longer part of the structure [34]. In this study, it was found that the Tsai-Wu failure criterion successfully captured the onset and progression of failure through the layers of the fibre reinforced composite laminate as shown in Figure 68, where it is confirmed that the failed layer stresses are relaxed to zero. All the upper layers (i.e. layers one to four) failed in tension, whilst the lower layers (i.e. layers five to eight) failed in compression. This may not always be the case due to the nature of impulse loading and if multi-directional laminates are to be used. Note that the failure plot shown in Figure 68 does not represent the Tsai-Wu failure indices. A value of one in Figure 68 indicates that failure has not occurred, and zero represents failure. Figure 69 shows a failure fringe plot of layer eight only when progressive failure began to occur at the fully constrained edge. Not all layers had failed at this time (t = 0.151 ms), therefore the elements at the fully constrained edge remained in the analysis. Figure 70 shows a failure fringe plot with all layers selected at a later time (t = 0.229 ms). Here, all layers had failed at the fully constrained edge and the three affected elements were essentially removed from the analysis.

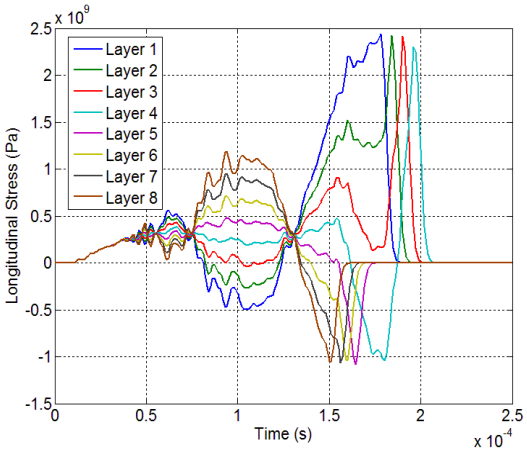


Stress plot in the fibre direction

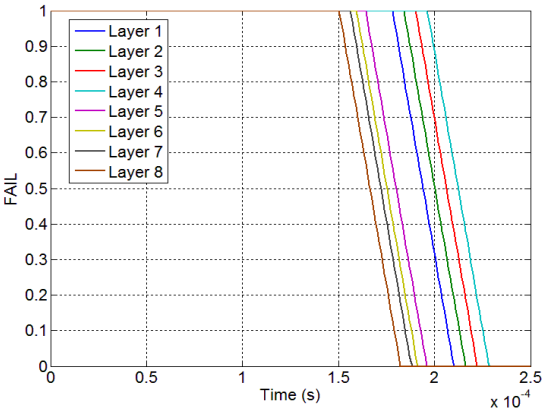


FAIL plot showing progressive failure of the individual laminae

**Figure 68: Impulsively loaded unidirectional composite laminate strip results showing the onset and progression of failure through the laminate layers**

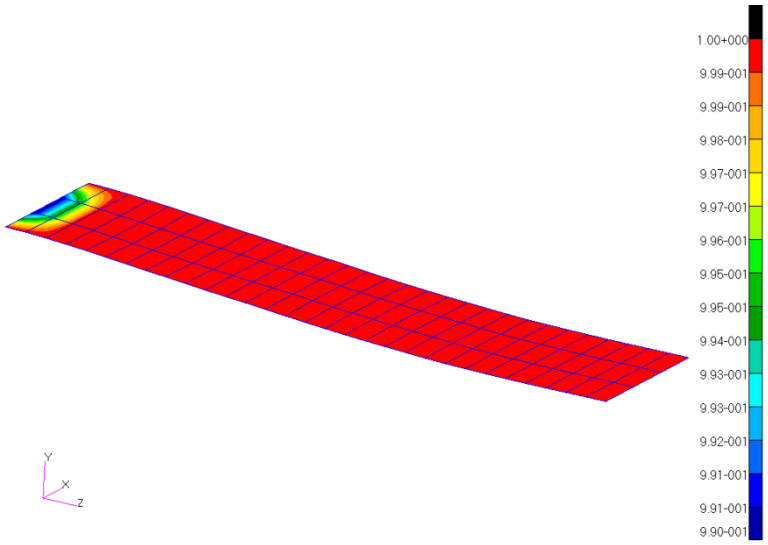


**Figure 69: FAIL fringe plot of sublayer 8 at time = 0.15101 ms**

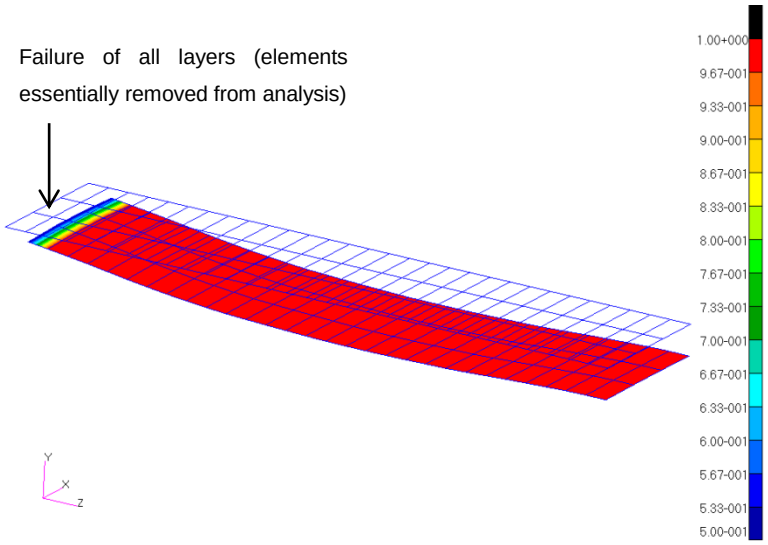


**Figure 70: FAIL fringe plot of laminate at time = 0.22902 ms**

### 2.4.5 Conclusions

An investigation into the performance of the Tsai-Wu failure criterion to capture the onset and progression of failure through the layers of fibre reinforced composite laminates was conducted for an impulsively loaded unidirectional laminate strip model. Investigation of the stress and failure time-history plots revealed that the Tsai-Wu failure criterion successfully captured the onset and progression of failure through the laminate layers.

In general, the Tsai-Wu failure criterion accurately predicts the deformation of laminates at low strains, as is expected for fibre-dominated laminates. Laminate deformation was therefore assumed to be reasonably accurate as only fibre-dominated layups were used throughout this study. It became apparent during this study that the Tsai-Wu failure criterion over-predicts the strength of laminates for biaxial compression-compression loading. During impact, a change in aircraft pitch produces bending moments in the fuselage, which result in compressive or tensile stresses along the length of the fuselage (in addition to fuselage compressive stresses due to longitudinal impact forces). It was therefore assumed that the applied stresses are

uniaxial (along the length of the fuselage) and a biaxial compression-compression loading condition may be ignored. This assumption was also deemed applicable for the impulsively loaded unidirectional composite laminate strip model, thus the loading condition for the unidirectional laminate strip model was deemed representative of the expected loading conditions for the fuselage of the aircraft.

Based on the results obtained and in conjunction with the abovementioned assumptions, the implementation of the Tsai-Wu failure criterion for composite aircraft crashworthiness applications is deemed valid. Note that the Tsai-Wu failure criterion predicts the onset of failure, but does not explicitly identify the failure mode. Strain rate effects were not considered.

## 2.5 Aircraft and impact terrain modelling

### 2.5.1 Introduction

This section discusses the finite element representation of the various components involved in the full-scale crash analysis models presented in Chapter 3. Additionally, the parameters, loads and boundary conditions involved in the analyses are discussed. Where appropriate, the techniques developed at the subcomponent level were implemented. The global coordinate system used in the full-scale analyses was the same as shown in Figure 34, except the positive z-axis points downward as per the ATB model's inertial coordinate system. Simplified finite element model representations of various components were made due to a lack of available information, most notably the stabilisers and wings; however for demonstrative purposes, the presented model was deemed sufficient. The landing gear and door were omitted from the analysis models.

### 2.5.2 Finite element model of the aircraft

For FEA purposes, simplified geometry of the aircraft was used as shown in Figure 71. A slice through the centre of the aircraft is shown to provide some clarity to the construction of the aircraft. The aircraft has an essentially monocoque construction, where the loads are mainly supported through the fibre reinforced composite skin of the aircraft. Finite element representation of the aircraft is shown in Figure 72. Convergence testing was performed for the selection of a suitable global element size for finite element representation of the aircraft structure. The resulting global element edge length selected was 40 millimetres. Refer to Chapter 2 Section 5.3 for details regarding the convergence testing. For the discussions that follow, all materials selected for the finite element representation of the aircraft were assumed due to a lack of available data. Additionally, all four-node quadrilateral shell elements were assigned a Key-Hoff element formulation and all two-node beam elements were assigned a Hughes-Liu element formulation (excluding the seat belt). A Hughes-Liu element formulation is suitable for when partial yielding occurs as would be expected in crash analyses. In comparison, numerical instabilities were encountered with the Belytschko-Schwer element formulation, as it is not suitable for partially yielded material.

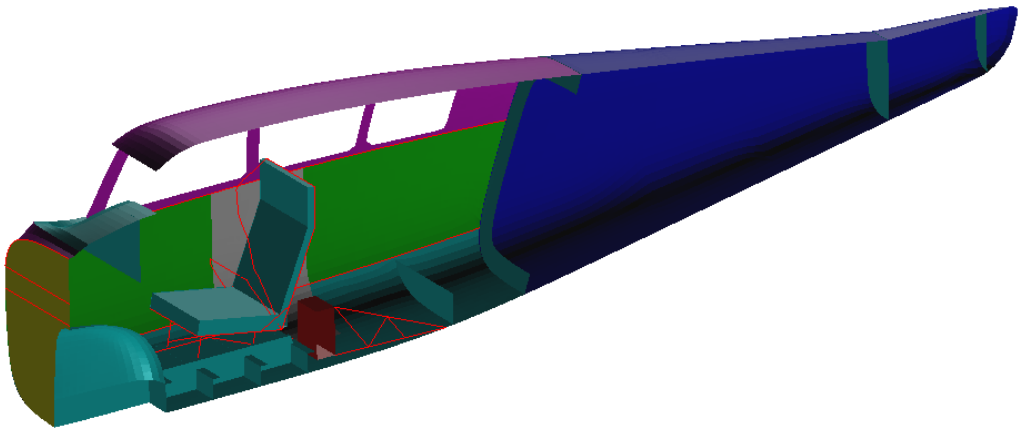

**Figure 71: Half-slice through the aircraft's centre (excluding windows, engine, engine mount, main wing spar, and stabilisers)**

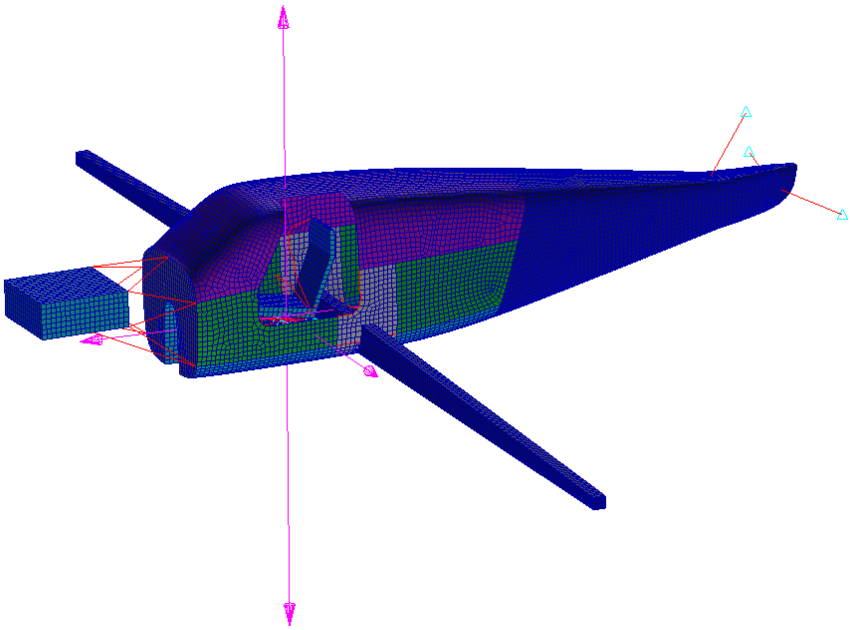

**Figure 72: Finite element representation of the aircraft, including its centre-of-gravity indicated by vectors**

Four-node quadrilateral shell elements were used to model various fibre reinforced composite components as shown in Figure 73, with the technique developed in Chapter 2 Section 4 (i.e. the implementation of the Tsai-Wu failure criterion to capture the onset and progression of failure through the

layers). Table 8 lists these components along with the laminae material, laminae orientation, and laminae thickness assigned in the finite element model. The layups used may not necessarily be realistic but are deemed satisfactory for demonstrative purposes. Figure 74 shows how the various laminates are oriented, which provides a basic modelling check to ensure correct application of the laminates. The vectors shown are aligned with the x-axis of the laminates, which corresponds to a zero degree lamina orientation. The glass fibre reinforced plastic (GFRP) and carbon fibre reinforced plastic (CFRP) mechanical properties for unidirectional laminae assigned to the aircraft are listed in Table 9. The laminates foam core mechanical properties are listed in Table 10, and was represented with an isotropic elastic-plastic material model. An isotropic elastic-plastic material model was deemed sufficient to characterise the foam core, since failure of the GFRP and CFRP laminae occur at relatively low strains, which are typically within the initial linear elastic region of foam.

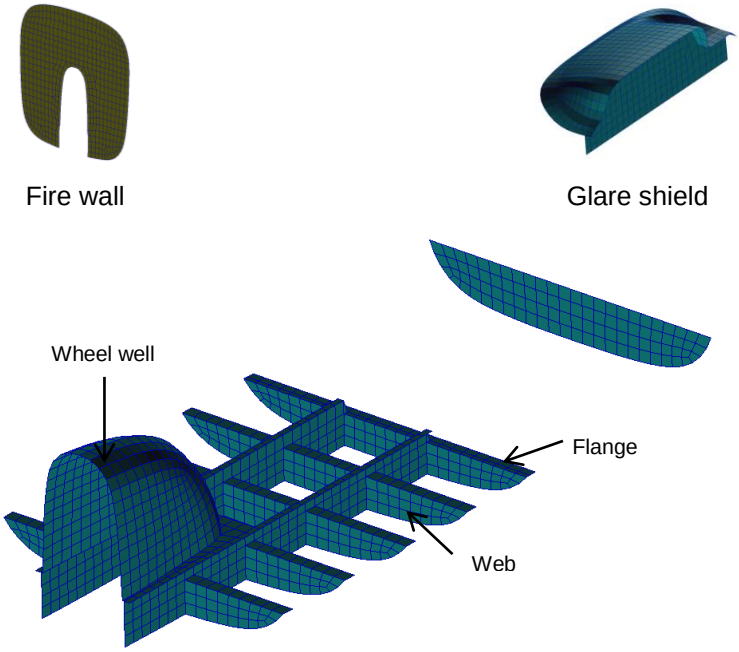


**Figure 73: Finite element representation of various fibre reinforced composite components of the aircraft**

**Table 8: Fibre reinforced composite material layup details**

| Component | Laminae material | Laminae orientation | Laminae thickness (mm) |
|---|---|---|---|
| Fire wall | GFRP | $[0°/90°/45°/-45°/\overline{FC}]_S$ | $[0.625/0.625/0.625/0.625/\bar{5}]_S$ |
| Glare shield | GFRP | $[0°/90°/45°/-45°/\overline{FC}]_S$ | $[0.28/0.28/0.28/0.28/\bar{3}]_S$ |
| Floor structure webs | GFRP | $[0°/90°/45°/-45°/\overline{FC}]_S$ | $[0.2/0.2/1.05/1.05/\overline{10}]_S$ |
| Floor structure flanges | GFRP | $[0°/90°/45°/-45°]_S$ | $[3.25/0.25/0.25/0.25]_S$ |
| Fuselage skin; Bulkheads | GFRP | $[0°/90°/45°/-45°/\overline{FC}]_S$ | $[0.625/0.625/0.625/0.625/\overline{10}]_S$ |
| Bulkhead flange | CFRP | $[0°/90°/45°/-45°]_S$ | $[1.25/0.125/0.125/0.125]_S$ |
| “High strength” fuselage skin | CFRP | $[0°/90°/45°/-45°/\overline{FC}]_S$ | $[1/1/1/1/\bar{7}]_S$ |
| Wheel well | GFRP | $[0°/90°/45°/-45°]_S$ | $[0.375/0.375/0.375/0.375]_S$ |
| Wing joint | CFRP | $[0°/90°/45°/-45°]_S$ | $[2/2/2/2]_S$ |
| Main wing spar sides | CFRP | $[0°/90°/45°/-45°]_S$ | $[0.5/0.5/1/1]_S$ |
| Main wing spar top and bottom | CFRP | $[0°/0°/90°/45°/-45°]_S$ | $[2.125/2.125/0.25/0.25/0.25]_S$ |

Note: FC indicates a foam core (the orientation is not applicable).

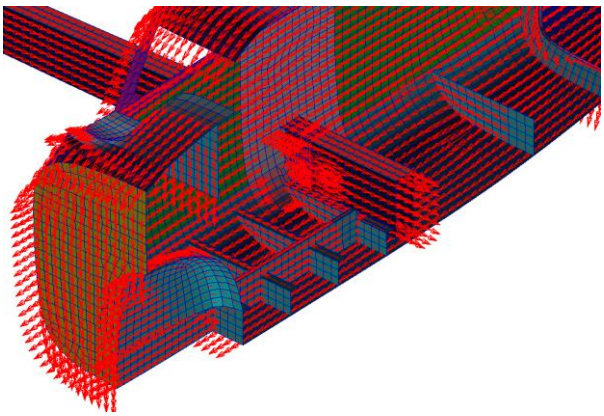

**Figure 74: Aircraft half-section showing orientation vectors for the fibre reinforced composite laminates along the laminates x-axis**

**Table 9: Mechanical properties of unidirectional laminae used in the aircraft model**

| | CFRP [69] | GFRP |
|---|---|---|
| Density, $\rho$ (kg/m$^3$) | 1580 | 2067.4 |
| Longitudinal modulus, $E_{11}$ (GPa) | 126 | 32.3 |
| Transverse modulus, $E_{22}$ (GPa) | 11 | 7.93 |
| Poisson's ratio, $\nu_{12}$ | 0.28 | 0.3 |
| Shear modulus, $G_{12}$ (GPa) | 6.6 | 3.13 |
| Shear modulus, $G_{13}$ (GPa) | 6.6 | 3.13 |
| Shear modulus, $G_{23}$ (GPa) | 3.3 | 1.565 |
| Shear strength, $S_{12}$ (MPa) | 79 | 50 |
| Longitudinal tensile strength, $X_T$ (MPa) | 1950 | 615.73 |
| Longitudinal compressive strength, $X_C$ (MPa) | 1480 | 355 |
| Transverse tensile strength, $Y_T$ (MPa) | 48 | 42 |
| Transverse compressive strength, $Y_C$ (MPa) | 200 | 105 |

**Table 10: Foam core mechanical properties (ElasPlas – DMATEP)**

| | |
|---|---|
| Density, $\rho$ (kg/m$^3$) | 80 |
| Poisson's ratio, $\nu$ | 0.01 |
| Shear modulus, G (MPa) | 30 |
| Yield stress, $\sigma_y$ (kPa) | 950 |
| Maximum plastic strain | 0.2 |

The purpose of the main wing spar finite element model was to approximately represent the inertia effects of the wings, as the mass of the wings will contribute to the loads that must be supported by the cabin structure. The main wing spar was modelled as a "box" type structure, with an extended length (approximately equal to a full wing span of 10.4 metres), and taper on the upper surface to better approximate an assumed triangular wing mass distribution including a 100 percent fuel load as shown in Figure 73. The density of the CFRP was increased to 21813.6 kilograms per cubic metre to acquire a total wing mass of 955 kilograms, which composed of a total fuel mass of 460 kilograms and total structural wing mass of 495

kilograms. Note that increasing the density as discussed has negative implications on the structural behaviour of the main wing spar; however the behaviour of this component is not of concern. The only requirement is that the inertia effects are represented as previously stated.

Connection of the main wing spar to the fuselage of the aircraft was assumed to be done through a hinge type connection each side of the aircraft and a centrally located brace. Finite element representation of a hinge type connection is shown in Figure 75, where both the pin and sleeve were modelled with four-node quadrilateral shell elements. Both the pin and sleeve were assigned rigid properties as it was assumed that they would not experience failure. The pin was connected to the side walls of the wing joint and the sleeve was connected to the side walls of the main wing spar by equivalencing (merging of nodal points that are close together) the nodal points. Contact between the sleeve and pin was defined to provide support for the main wing spar and to allow rotation of the sleeve about the pin.

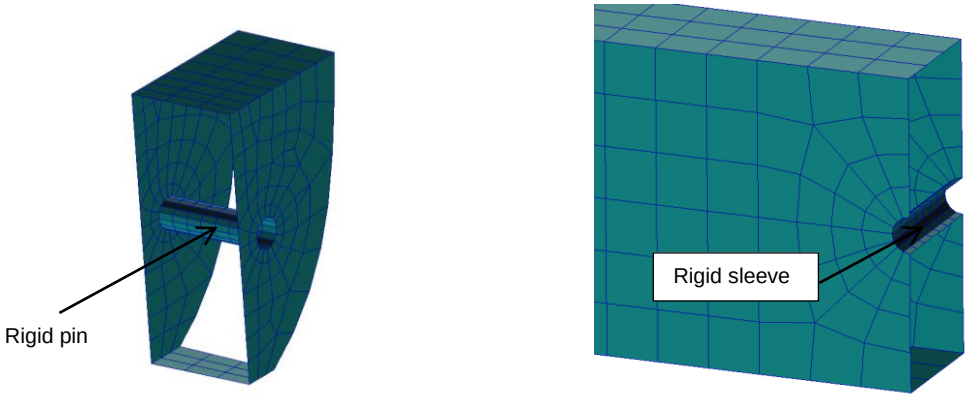


Wing joint Section through main wing spar

**Figure 75: Finite element representation of the wing joint rigid pin and main wing spar rigid sleeve (half-slice)**

The purpose of the centrally located brace was to limit the deflection of the main wing spar at its centre. Finite element representation of the brace is shown in Figure 76, which was modelled with four-node quadrilateral shell

elements and two-node beam elements. The shell elements “wrap around” the main wing spar and contact was defined between the shell elements of the brace and the shell elements of the main wing spar. Rigid body elements (RBE2s), with all six degrees of freedom coupled, were used to represent fastening of the brace to the aircraft’s fuselage. Both the shell and beam elements were assigned an isotropic elastic-plastic material model with a von Mises yield model. AISI 4130 steel material properties were defined as per Table 11. The shell elements were assigned a thickness of two millimetres, whilst the beam elements were assigned a tubular cross-section with an outer and inner diameter of 25.4 and 22.91 millimetres respectively.

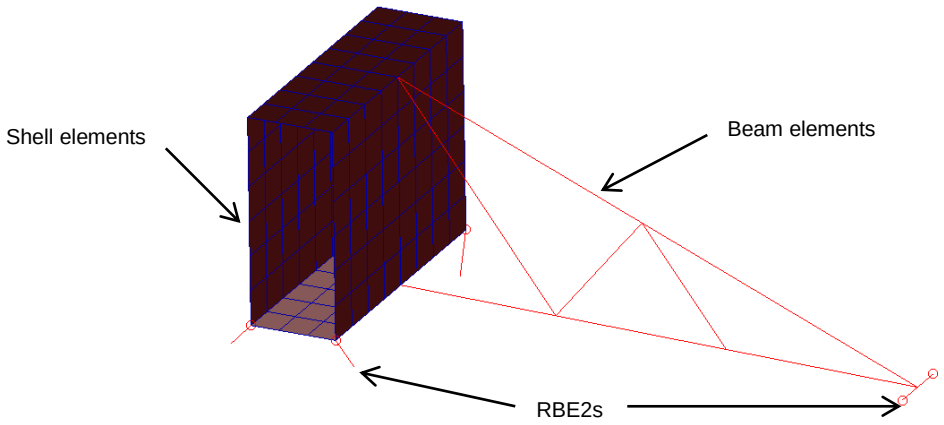


**Figure 76: Finite element representation of the main wing spar brace**

**Table 11: Mechanical properties representative of isotropic elastic-plastic (DMATEP) materials**

| | AISI 4130 | 1050 H14 | 2024 T351 | 7075 T6 | "Compressive CFRP" | PMMA |
|---|---|---|---|---|---|---|
| Density, $\rho$ (kg/m$^3$) | 7850 | 2705 | 2780 | 2800 | 1580 | 1220 |
| Elastic modulus, E (GPa) | 205 | 69 | 73.1 | 72 | 126 | 3.8 |
| Poisson's ratio, $\nu$ | 0.29 | 0.33 | 0.33 | 0.33 | 0.28 | 0.4 |
| Yield stress, $\sigma_y$ (MPa) | 435 | 103 | 324 | 480 | 1480 | 72.4 |
| Maximum plastic strain | 0.255 | 0.1 | 0.2 | 0.11 | 0.01175 | 0.019 |

Simplified finite element representations of the vertical and horizontal stabilisers were created with two-node beam elements and point masses located at the stabilisers' centre-of-gravity, as shown in Figure 77. The purpose of the simplified stabiliser finite element models was to approximately represent the inertia effects of the stabilisers, as the stabiliser masses will contribute to the loads that must be supported by the cabin structure. To represent bonded connections between the bulkheads and stabilisers, the nodal points of the stabilisers and bulkheads were equivalenced. The point mass for the vertical stabiliser was 40.42 kilograms and the point mass for each horizontal stabiliser was 31.16 kilograms. The beam elements were assigned an isotropic elastic-plastic material model with a von Mises yield model. 2024 T351 aluminium material properties were defined as per Table 11. An I-beam cross-section was defined for the beam elements with an overall height and width of 50 millimetres and a constant thickness of five millimetres. The vertical stabiliser was oriented to take bending loads in the x-direction, whilst the horizontal stabilisers were oriented to take bending loads in the z-direction (refer to Figure 34 for reference coordinate system).

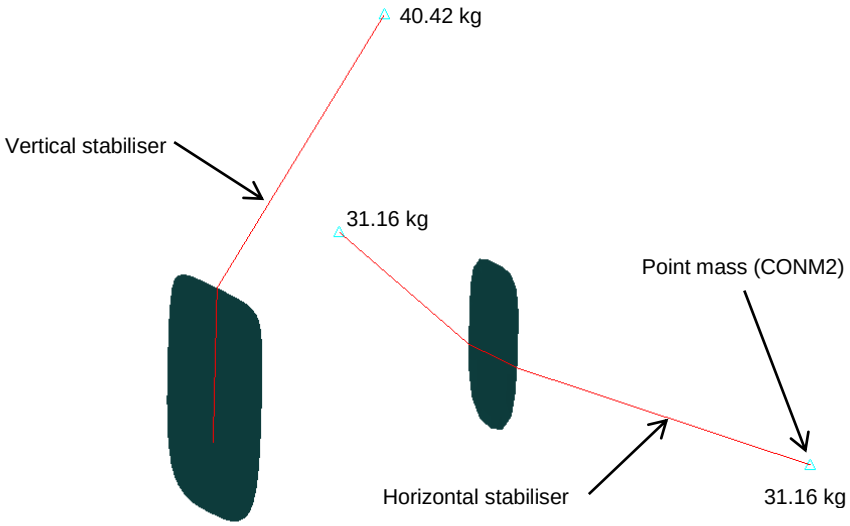


**Figure 77: Finite element representation of the rear bulkheads and vertical and horizontal stabilisers (elements excluded for clarity)**

A simplified finite element representation of the engine was deemed sufficient for analysis as shown in Figure 78. The engine was modelled with four-node quadrilateral shell elements and was assigned rigid properties with a mass of 146 kilograms.

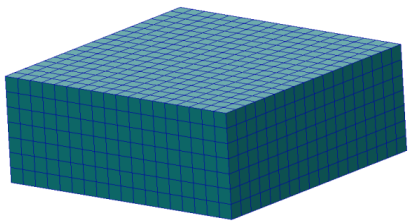

**Figure 78: Finite element representation of the engine**

Two-node beam elements were used to represent simplified finite element models of the engine mount frame, fire wall stiffeners, and fuselage skin stiffeners as shown in Figure 79. To represent bonded connections, the fire wall stiffeners nodal points and fuselage skin stiffeners nodal points were equivalenced to the fire wall and fuselage skin respectively. The nodal points

at the connection points of the engine mount frame to the fire wall stiffeners and fuselage skin stiffeners were equivalenced to transfer the loading of the engine to the aircraft's structure. Four corner nodal points of the engine's rear face were equivalenced to the engine mount frame along with two nodal points on the bottom face of the engine to represent connection points. The beam elements were assigned an isotropic elastic-plastic material model, where the engine mount frame was assigned a von Mises yield model whilst the fire wall stiffeners and fuselage skin stiffeners were assigned a bilinear yield model. AISI 4130 steel material was defined for the engine mount frame and material "compressive CFRP" was defined for the fire wall stiffeners and fuselage skin stiffeners as per Table 11. An example of a fibre reinforced composite stiffener with a trapezoidal cross-section is shown in Figure 80. A simplified finite element representation of a similar stiffener construction with beam elements and an isotropic elastic-plastic material model required assumptions to be made regarding the loading conditions, material properties, and failure. It was assumed the stiffeners will be subjected to mainly compressive loading, and therefore fail due to compression. The compressive lamina material properties for CFRP (refer to Table 9) were therefore assigned, and the material was thus named "compressive CFRP". The engine mount frame was assigned a tubular cross-section with an outer diameter of 25.4 millimetres and an inner diameter of 22.91 millimetres. The fuselage skin stiffeners and fire wall stiffeners were assigned channel cross-sections. The channels for the fire wall stiffeners were assigned a cross-sectional height and width of 20 millimetres. The channels for the fuselage skin stiffeners were assigned a cross-sectional height of 40 millimetres and width of 20 millimetres. All channel cross-sections were assigned a constant thickness of two millimetres.

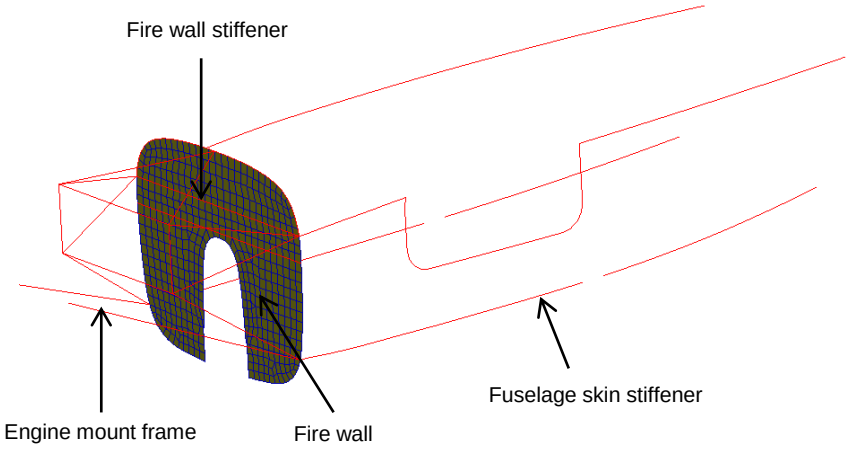


**Figure 79: Finite element representation of the fire wall, engine mount frame, and fuselage skin stiffeners**

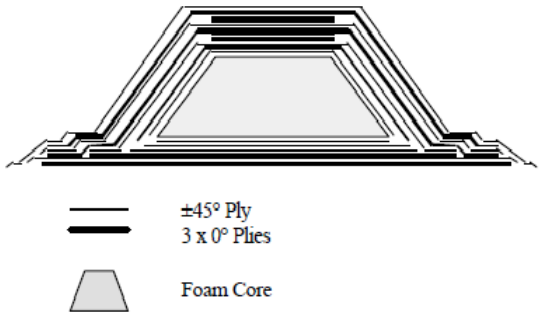


**Figure 80: Stiffener cross-section and layup schedule [70]**

Finite element representation of the aircraft windows are shown in Figure 81 and were modelled using four-node quadrilateral shell elements. A perfect connection of the windows to the fuselage was assumed for the purposes of analysis, therefore the nodal points of the windows were equivalenced to the nodal points of the fuselage. The shell elements were assigned an isotropic elastic-plastic material model with a bilinear yield model. A polymethyl methacrylate (PMMA) material was defined for the windows with typical mechanical properties listed in Table 11. The windows were all assigned a thickness of three millimetres.

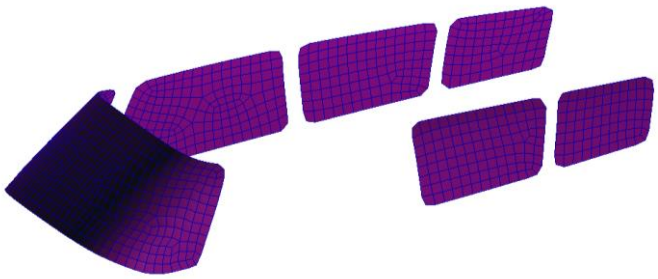

**Figure 81: Finite element representation of the aircraft windows**

Figure 82 shows details of a simple finite element model used to represent the aircraft's seat within a full-scale crash analysis model. It consisted of a seat pan and frame structure, seat foam, and seat legs structure. The seat pan was modelled with four-node quadrilateral shell elements, whilst the seat pan frame and seat legs were modelled with two-node beam elements. The seat pan, seat pan frame structure, and seat legs structure were all assigned isotropic elastic-plastic material models with a von Mises yield model. The seat pan was assigned 1050 H14 aluminium material properties (refer to Table 11) and a thickness of 1.5 millimetres. Both the seat pan frame and seat legs structures were assigned AISI 4130 steel material properties (refer to Table 11) with tubular cross-sections. The seat pan's frame was assigned an outer diameter of 15.875 millimetres and an inner diameter of 14.097 millimetres. The cross members of the seat legs were assigned with the same cross-section as the seat pan's frame, along with the beam elements connecting the lower seat pan to the seat legs. The shell element nodal points of the seat pan were connected to the beam element nodal points of the seat legs with the use of RBE2s, which had all six degrees of freedom coupled to represent a fastened or "welded" connection as can be seen in Figure 82. The remaining tubes of the seat legs were assigned with an outer diameter of 22.225 millimetres and an inner diameter of 19.736 millimetres. The seat foam (polypropylene) was represented using eight-node solid hexahedral elements with a FOAM2 material model implemented within MSC Dytran. The thickness of the seat foam was approximately 80 millimetres for

the seat bottom and 40 millimetres for the seat back. The FOAM2 material model was used to define isotropic elastic foam properties where Poisson's ratio is effectively zero. It may also define a nonlinear hysteresis response for unloading and includes strain-rate dependency [34, 54], although strain-rate dependency was not included in this study. The shell element nodal points for the seat pan have six degrees of freedom (translational and rotational), whereas the solid element nodal points for the seat foam have three degrees of freedom (translational only). A kinematic join entry (KJOIN) within MSC Dytran was used to connect the rotational degrees of freedom of the shell elements with the solid elements. The kinematic join acts as a locally inserted stiff element between nodal points. The nodal points already assigned with RBE2s may not be included in the kinematic join. The use of the kinematic join entry assumes that the seat foam is permanently bonded to the seat pan.

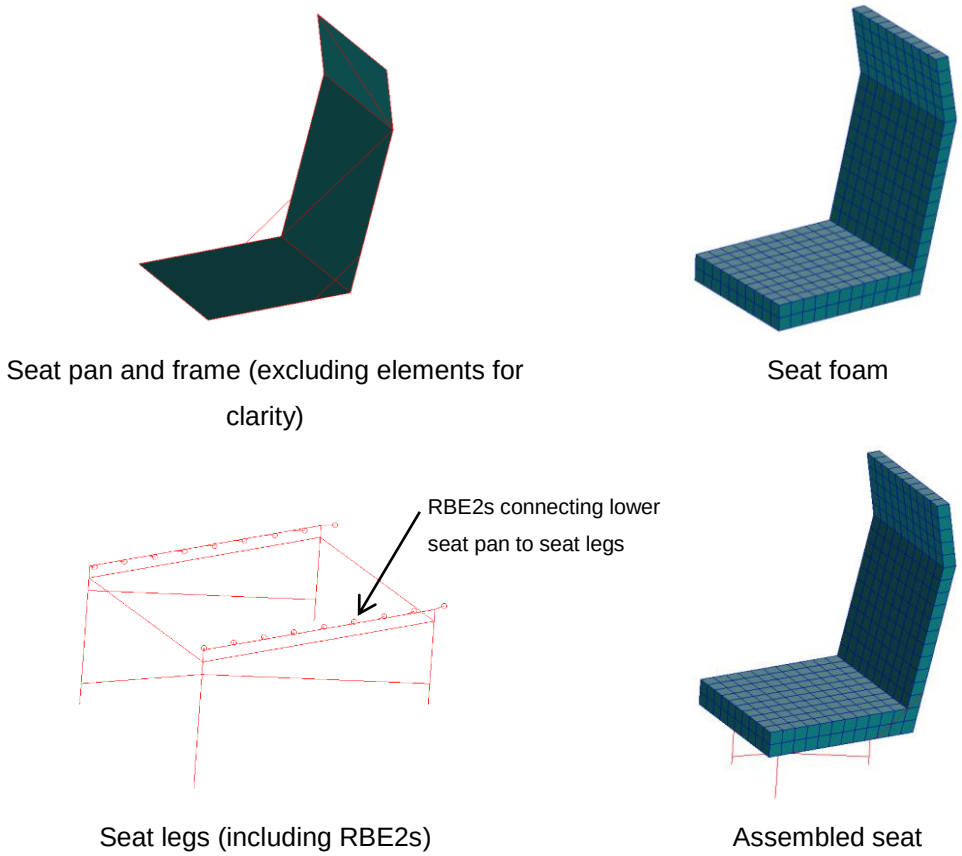


**Figure 82: Finite element representation of the aircraft seat**

The mechanical and stress-strain (or pressure versus crush factor within MSC Dytran) properties for the seat foam (polypropylene) model used in analyses are shown in Table 12 and Table 13, respectively. The mechanical and stress-strain properties were acquired from the work performed by Zhang et al. [71] and Landervik and Larsson [72], where experimental results of polypropylene foam subjected to uniaxial compression are presented as shown in Figure 83. A very crude approximation of the foam's experimental stress-strain graph was made as shown in Figure 83 (graphical representation of Table 13); however was deemed satisfactory for demonstrative purposes. The experimental data selected for model input corresponds to a quasi-static loading condition of strain rate $1.6x10^{-3}$ per second as the effects of high strain rate loading were excluded for this study. The bulk modulus of 450 megapascals was approximated based on the maximum slope of the stress-strain response for numerical stability reasons, and also agrees with the value input by Landervik and Larsson [72]. Figure 84 shows further details regarding the stress-strain behaviour of a foam material exhibiting a tensile cut-off stress, an exponential unloading curve, and a large "bottoming-out" stress. A large "bottoming-out" stress of 1500 kilopascals at a strain of 0.85 was input to ensure that for large strains, the element is prevented from deforming into an extremely small volume or negative volume. Small element volumes may significantly reduce analysis time increments and negative element volumes may cause analyses to prematurely terminate. A tensile cut-off stress of negative 200 kilopascals was assumed to provide strength in tension. An energy dissipation factor of 0.8 was chosen because polypropylene foams experienced only 20 percent permanent strain after being unloaded from 80 percent applied strain in the work by Zhang et al. [71]. An exponential unloading curve was assumed. Note that validation of the FOAM2 material model is still required.

**Table 12: Seat foam mechanical properties (FOAM2)**

| | |
|---|---|
| Density, ρ (kg/m$^3$) | 49 |
| Bulk modulus, K (MPa) | 450 |
| Cut-off stress (kPa) | -200 |
| Energy dissipation factor | 0.8 |

**Table 13: Seat foam stress-strain data**

| Strain | Stress (kPa) |
|---|---|
| 0 | 0 |
| 0.2125 | 213.04 |
| 0.425 | 301.58 |
| 0.6375 | 406.97 |
| 0.85 | 1500 |

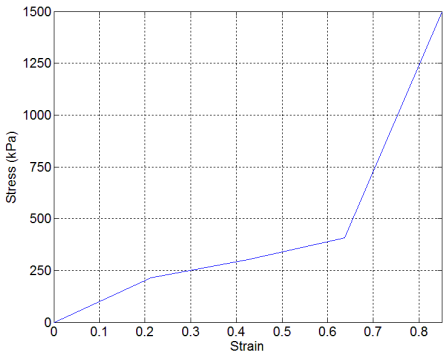


Model input (8x10$^{-5}$ m/s cross-head rate corresponding to a strain rate of 1.6x10$^{-3}$)

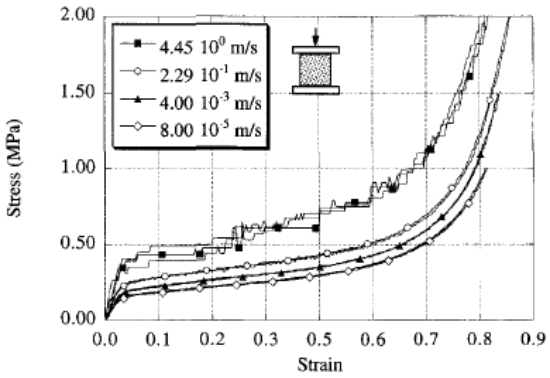


Experimental [71]

**Figure 83: Experimental stress-strain response of polypropylene foam subjected to uniaxial compression with different strain rates, along with the approximation for model input corresponding to loading at 8x10$^{-5}$ m/s (1.6x10$^{-3}$ per second strain rate)**

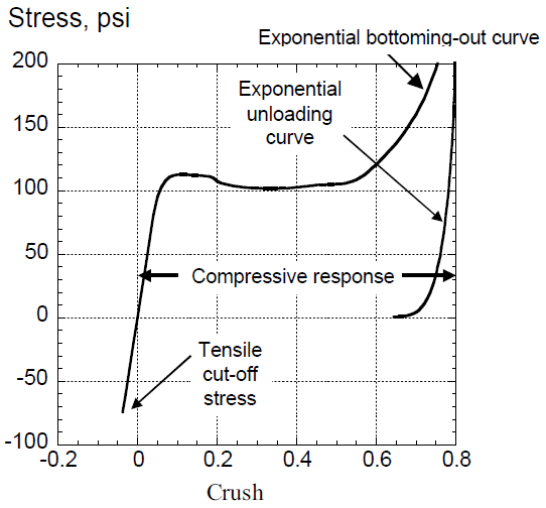


**Figure 84: Stress versus volumetric crush for a foam material exhibiting a tensile cut-off stress, an exponential unloading curve, and a large exponential bottoming-out stress [41]**

In order to justify selection of the FOAM2 material model, the general behaviour of low density polymeric foams needs to be understood. Low density polymeric foams are of interest in crashworthiness analysis due to their excellent impact energy absorbing capability and are commonly used in seat cushion applications. For differing loading conditions, transitions of failure mode and deformation are observed. Foams may behave ductile in compression and brittle in shear and tension [71]. The following discussions focus on the compressive behaviour of polymeric foams, as the compressive behaviour is of most interest in crashworthiness applications. Some examples of synthetic polymers are polystyrene, polyethylene, polyurethane and polypropylene.

According to experiments performed by Zhang et al. [71], the polymeric foam materials under their study all exhibited isotropy. Figure 85 describes typical compressive deformation of foams with the use of three zones, where the convention for compressive stress is positive. Zone one represents an initial linear (ideal approximation) elastic region caused from cell wall bending. Zone two represents a plateau caused from cell wall buckling parallel to the

loading axis [73]. Zone three represents densification or compaction due to the cell walls crushing together. The energy absorbing capability of polymeric foams is derived from their ability to maintain a nearly constant stress value whilst undergoing large deformations under compression as shown in zone two. For open cell foams, gas exits the foam through open pores or channels, and elastic behaviour is observed. For closed cell foams, the gas pressure may increase enough to permanently rupture the cell walls (unless the material is strong enough), which may lead to plastic behaviour after zone one. Polymeric foams may therefore be categorized as either rigid (elastic-plastic) or flexible (elastic), depending on the post loading behaviour [71]. The experimental work performed by Zhang et al. [71] revealed that polystyrene foams are rigid (crushable with no resilience), polyurethane foams are flexible (full but retarded resilience), and polypropylene foams are semi-rigid. The polypropylene foams experienced 20 percent permanent strain after having been unloaded from 80 percent applied strain. The experiments also revealed that the foam specimens underwent macroscopic uniform deformation without observable bulging and distortion, resulting in a negligible Poisson's effect when subjected to uniaxial compression. This also implies a negligible difference between engineering and true stress due to a negligible change in cross-sectional area. Additional observations made in the experimental work were that polymers are sensitive to changes in temperature and strain rates; however were not considered in this study.

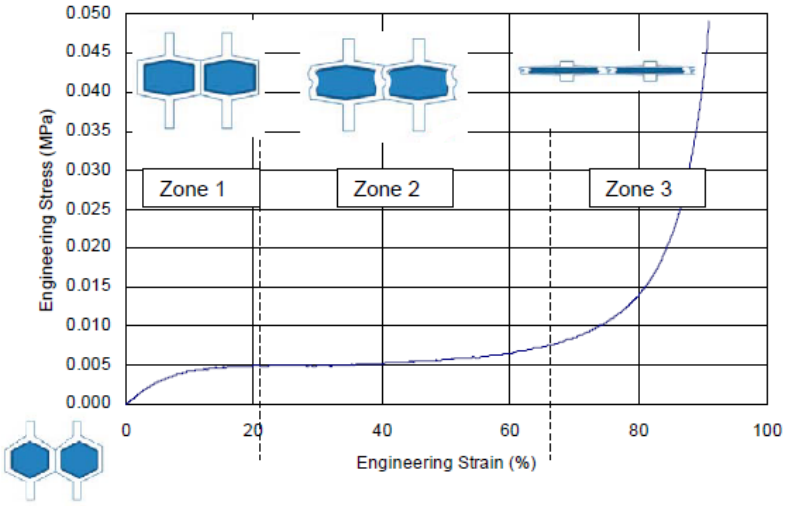


**Figure 85: Typical compressive deformation zones observed in foams [73, 74]**

Finite element representation of the two seat rails and the floor board is shown in Figure 86, along with the floor structure, seat, and seat belt. The seat rails were modelled with two-node beam elements, whilst the floor board was modelled with four-node quadrilateral elements. Both the floor board and seat rails were assigned with an isotropic elastic-plastic material model and a von Mises yield model. An I-beam cross-section with 7075 T6 aluminium material properties (refer to Table 11) was assigned to the seat rails. The I-beams had an overall height and width of 20 millimetres, a constant thickness of two millimetres, and had a neutral axis offset of ten millimetres in order for the I-beams to effectively sit on top of the floor board. The floor board was assigned 1050 H14 aluminium material properties as shown in Table 11 with a thickness of two millimetres. The nodal points of the seat rail beam elements were equivalenced to the nodal points of the floor structure's flanges to represent a fastened connection. RBE2s with all six degrees of freedom coupled were used to "fasten" the floor board to the flanges of the floor structure.

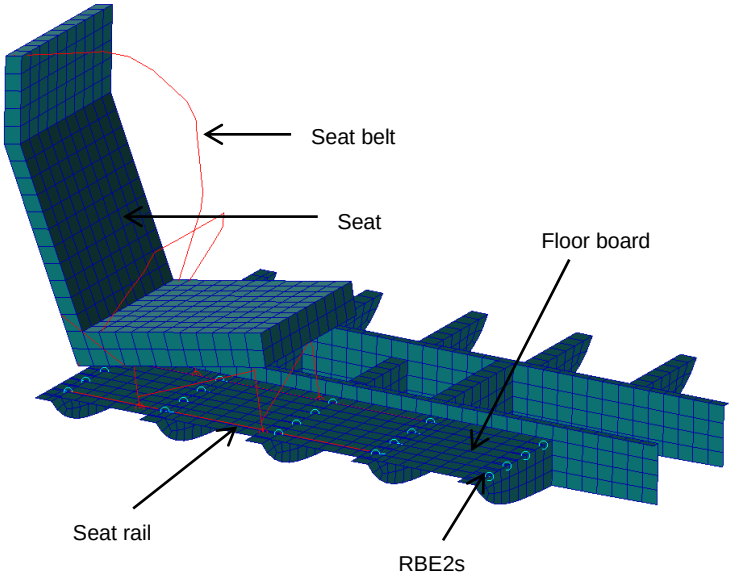


**Figure 86: Finite element representation of the aircraft's floor structure, floor board, and seat**

Finite element representation of the aircraft's mass and its centre-of-gravity were checked and appeared reasonable (refer to Figure 72 for the position of the centre-of-gravity). Note that the mass and centre-of-gravity calculations excluded the engine mass and all beam elements due to software limitations in MSC Patran. The calculated mass of the aircraft was 1607 kilograms and the engine mass assigned was 146 kilograms. These two figures add up to 1753 kilograms (still excluding the beam elements), which tends to approximately agree with the maximum take-off weight of a typical light aircraft. The mass of all beam elements were assumed negligible.

### 2.5.3 Convergence test

Determination of an optimum global element size (i.e. element edge length) for finite element representation of the aircraft structure presented in this study, required convergence testing too be performed. More specifically, h-convergence testing (refer to Chapter 1 Section 2.3) was performed where

convergence of the finite element solutions is achieved by increasing the number of elements within the domain (body of interest). Convergence testing of the entire aircraft would be too time consuming, therefore finite element representation of only a portion of the aircraft's floor structure was chosen for convergence testing as the response of the floor structure in a crash event is critical to occupant survivability. Four different global element edge lengths were used for convergence testing. The first finite element model used an element edge length of 10 millimetres, resulting in a total of 12036 elements used to represent the domain (refer to Figure 87). The second finite element model used an element edge length of 20 millimetres, resulting in a total of 2958 elements used to represent the domain. The third finite element model used an element edge length of 40 millimetres, resulting in a total of 884 elements used to represent the domain. The fourth finite element model used an element edge length of 60 millimetres, resulting in a total of 406 elements used to represent the domain. A summary of the finite element models used for convergence testing is given in Table 14. For simplification purposes, an isotropic linear elastic material model was defined, a material failure model was not assigned, and a single material thickness of 12.5 millimetres was assigned to all components. The material properties are shown in Table 15, which are similar to the unidirectional laminae properties of GFRP along the *1-axis* (principal material coordinate system) as shown in Chapter 2 Section 5.2, Table 9.

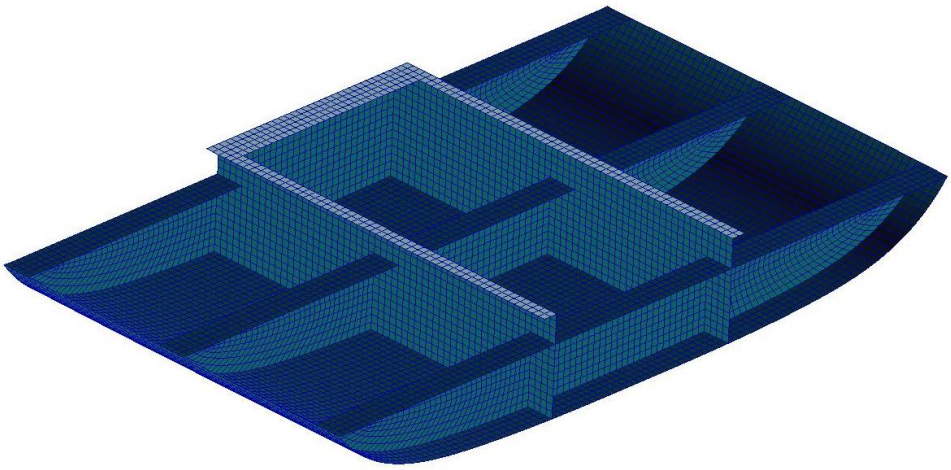

**Figure 87: Finite element representation of the floor structure (10 millimetre element edge length)**

**Table 14: Summary of finite element (FE) models used for convergence testing**

| FE model ID | Element edge length (mm) | Total number of elements |
|---|---|---|
| 1 | 10 | 12036 |
| 2 | 20 | 2958 |
| 3 | 30 | 884 |
| 4 | 40 | 406 |

**Table 15: Isotropic linear elastic material properties of the floor structure used for convergence testing**

| | |
|---|---|
| Elastic modulus, E (GPa) | 32.23 |
| Poisson's ratio, $\nu$ | 0.3 |
| Density, $\rho$ (kg/m$^3$) | 2067.4 |

Three types of analyses were used for convergence testing; namely normal modes, linear static, and dynamic analyses. The normal modes analyses were used to determine whether the stiffness and mass characteristics of the

finite element models were comparable. The linear static analyses were used to determine convergence of the displacement and von Mises stress results. Dynamic analyses were performed to determine how analysis run-times are affected by changes in element size. An increase in the number of elements results in an increase in accuracy; however the time taken for the analysis to complete may be impractical. In the discussions that follow, the convergence test results of finite element model 1 are used as a basis for comparison as this model uses the most elements to represent the domain, and is therefore deemed to be the most accurate model.

MSC Nastran was used to perform the normal modes analyses to determine the natural frequencies of each finite element model and to inspect the corresponding mode shapes. The natural frequencies corresponding to their respective mode shapes are listed in Table 16. Note that the first six mode shapes are rigid body modes (corresponding to three translational and three rotational degrees-of-freedom) as the structure is unconstrained. The natural frequency corresponding to each rigid body mode is zero Hertz. For a single degree-of-freedom spring-mass system, the natural frequency is [75]:

$$f_n = \frac{1}{2\pi}\sqrt{\frac{k}{m}} \tag{82}$$

where:

$f_n$ = natural frequency
$k$ = spring stiffness
$m$ = mass

As can be seen by the above equation, the natural frequency of the system can be manipulated by varying the mass and / or the stiffness. Although the above equation is for a simple system, the same principal holds for real and

complex systems. The maximum percentage difference is 1.06 percent when comparing the natural frequencies listed in Table 16 to the natural frequencies of finite element model 1. The stiffness and mass characteristics of all the models are therefore deemed acceptable.

**Table 16: Natural frequencies for the normal modes analyses**

| FE model ID | Natural frequencies for the corresponding mode shapes in Hertz (Hz) | | | |
|---|---|---|---|---|
| | Mode 7 | Mode 8 | Mode 9 | Mode 10 |
| 1 | 75.814 | 419.37 | 466.27 | 534.98 |
| 2 | 76.109 | 419.64 | 466.71 | 533.99 |
| 3 | 76.628 | 418.84 | 467.14 | 534.4 |
| 4 | 76.207 | 418.01 | 465.66 | 534.13 |

In simple terms, a mode shape (eigenvector) is the shape at which a structure oscillates within, where each mode shape corresponds to a specific natural frequency. For example, the mode shapes (excluding rigid body modes) for finite element model 1 and finite element model 3 are shown in Figure 88 and Figure 89 respectively. The fringe plots represent the eigenvectors with arbitrary magnitude (not displacement). Visual inspection of the mode shapes for each finite element model reveals that the mode shapes are all reasonably comparable to that of finite element model 1.

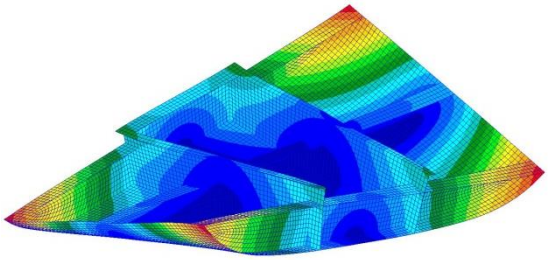

Mode shape 7

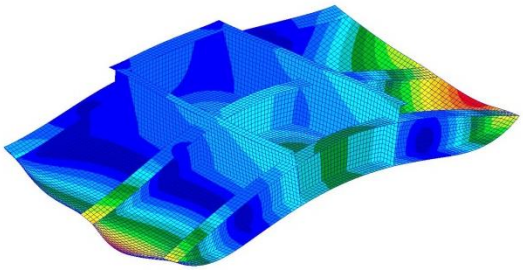

Mode shape 8

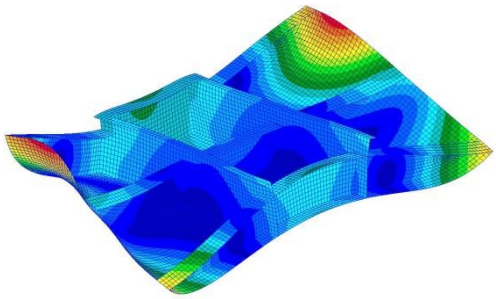

Mode shape 9

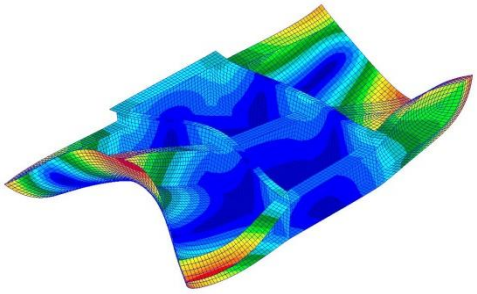

Mode shape 10

**Figure 88: Mode shapes for finite element model 1**

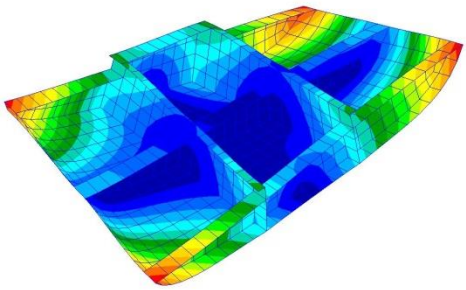

Mode shape 7

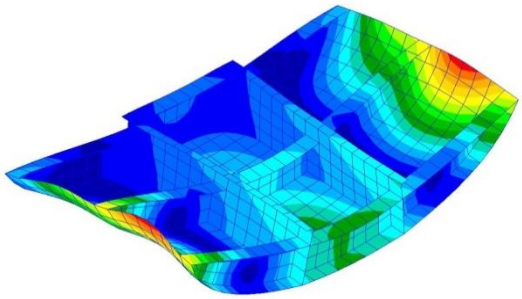

Mode shape 8

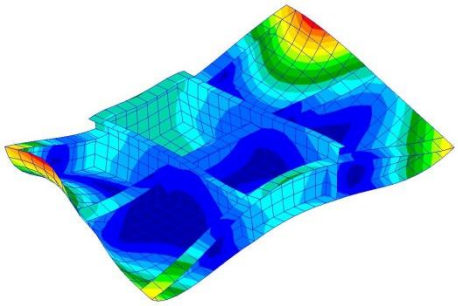

Mode shape 9

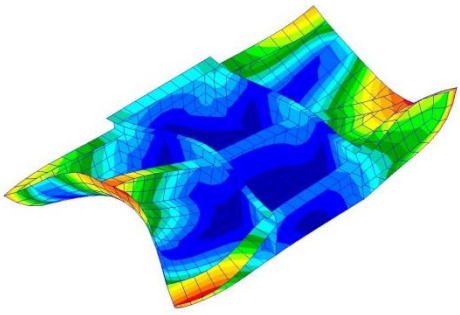

Mode shape 10

**Figure 89: Mode shapes for finite element model 3**

MSC Nastran was also used to perform the linear static analyses. As mentioned in Chapter 1 Section 5, impacts into soft soil introduces distributed loading into the fuselage skin. Additionally, a change in aircraft pitch produces bending moments in the fuselage. In order to represent similar loading conditions to those expected in a crash event, the floor structure was unconstrained and a pressure of five megapascals was applied to a portion of the floor structure as shown in Figure 90. In order to perform an analysis of an unconstrained structure in a static analysis, the inertia relief option in MSC Nastran is required. A typical and relevant application of inertia relief includes modelling of aircraft in flight. The inertia relief option calculates the rigid body loads required to counterbalance the applied loads. The rigid body loads are distributed over the finite element structure so that the sum of the applied forces and the sum of the moments equals zero. This “restraint” allows for a static analysis to be performed on a deformable structure. MSC Nastran has two types of inertia relief, a conventional (manual) type and an automatic type. The automatic type is recommended for finite element models with six rigid body modes, as is the case for unconstrained structures. For this type, MSC Nastran requires PARAM,INREL,-2 as an entry in the input file. Further details of inertia relief can be found in reference [76] and reference [77].

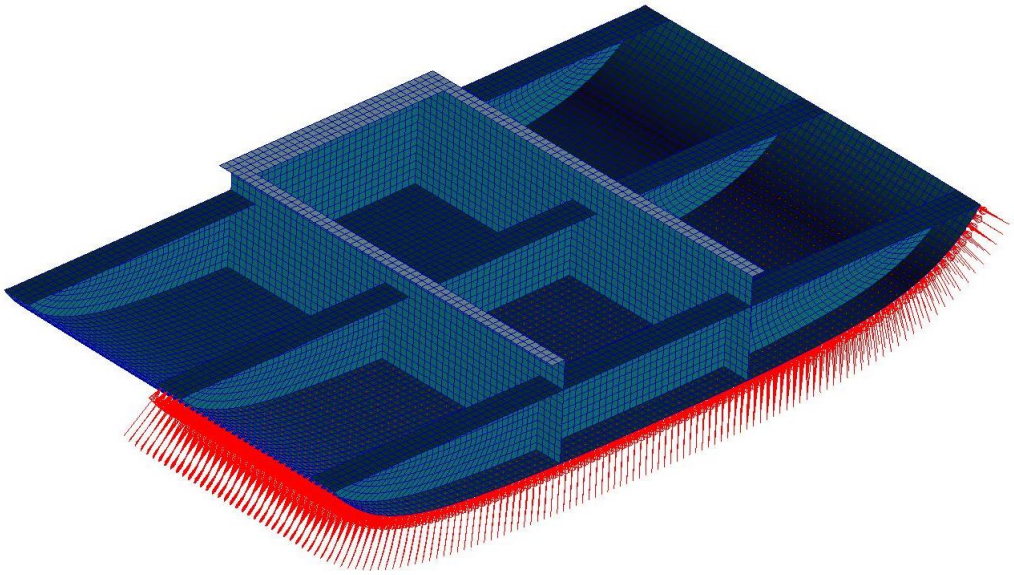

**Figure 90: Vectors representing the pressure loading applied to finite element model 1**

Figure 91 and Figure 92 graph the maximum von Mises and maximum displacement results of the linear static analyses respectively. Figure 93, Figure 94, Figure 95, and Figure 96 present displacement and von Mises stress fringe plots for finite element model 1 and finite element model 3. As indicated in Figure 91 and Figure 92, both the displacement and von Mises stress results converge to the results of finite element model 1 as the mesh is refined. The percentage error of the displacement and von Mises results relative to finite element model 1 are shown in Table 17. The percentage difference for finite element model 4 is relatively large compared to the other models, and is therefore not considered for use.

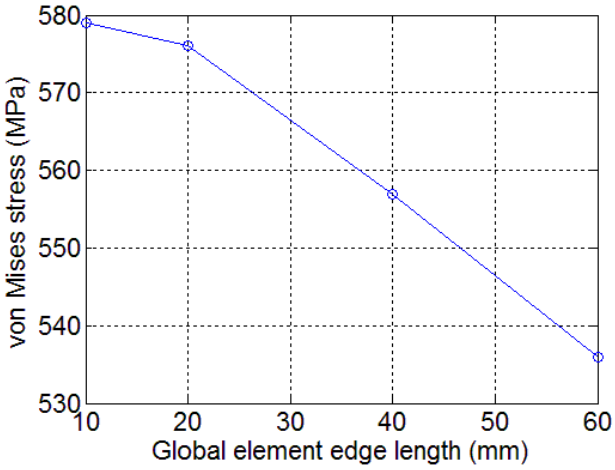


**Figure 91: Graph showing the maximum von Mises stress (Pa) results for the linear static analyses**

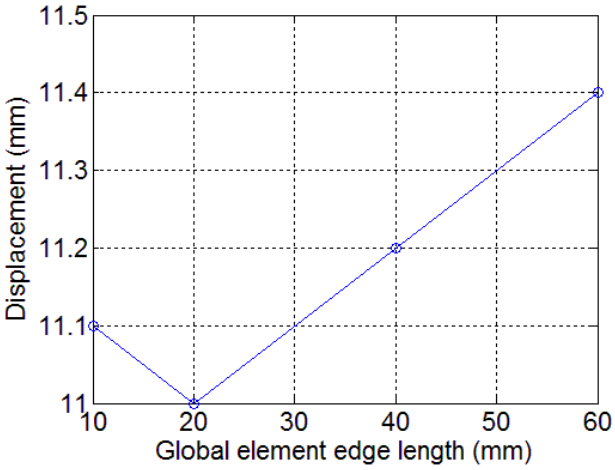


**Figure 92: Graph showing the maximum displacement (m) results for the linear static analyses**

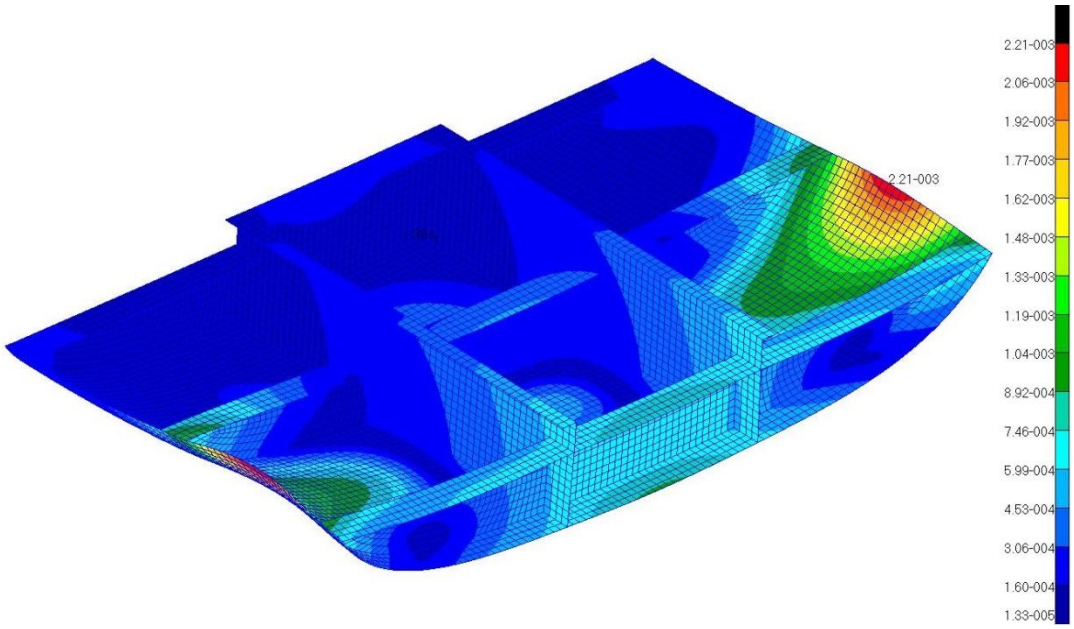


**Figure 93: Displacement (m) plot for a linear static analysis of finite element model 1**

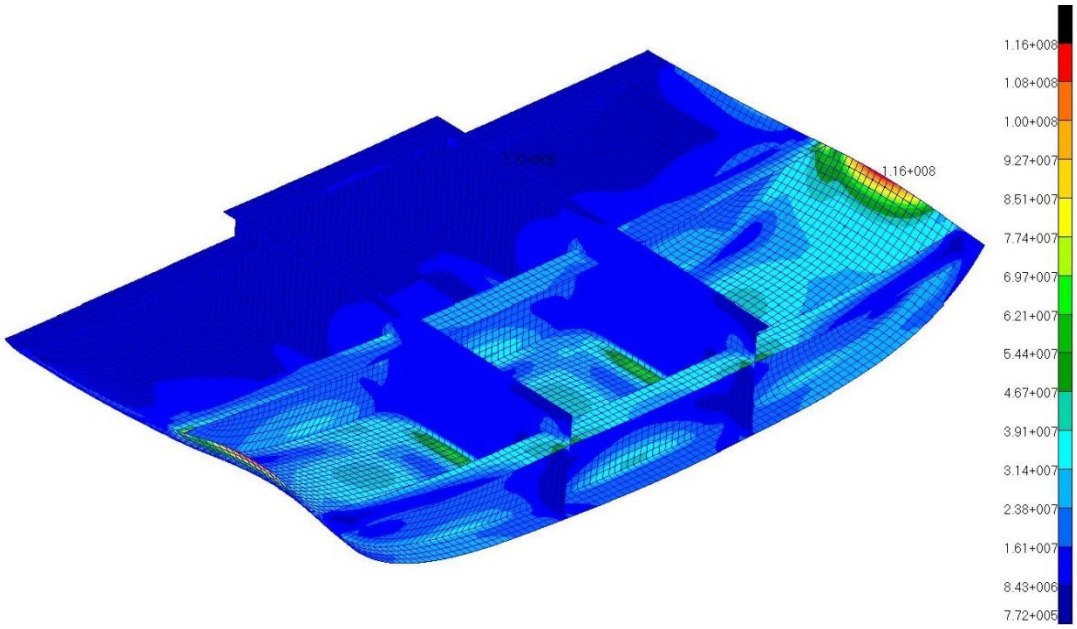


**Figure 94: von Mises stress (Pa) plot for a linear static analysis of finite element model 1**

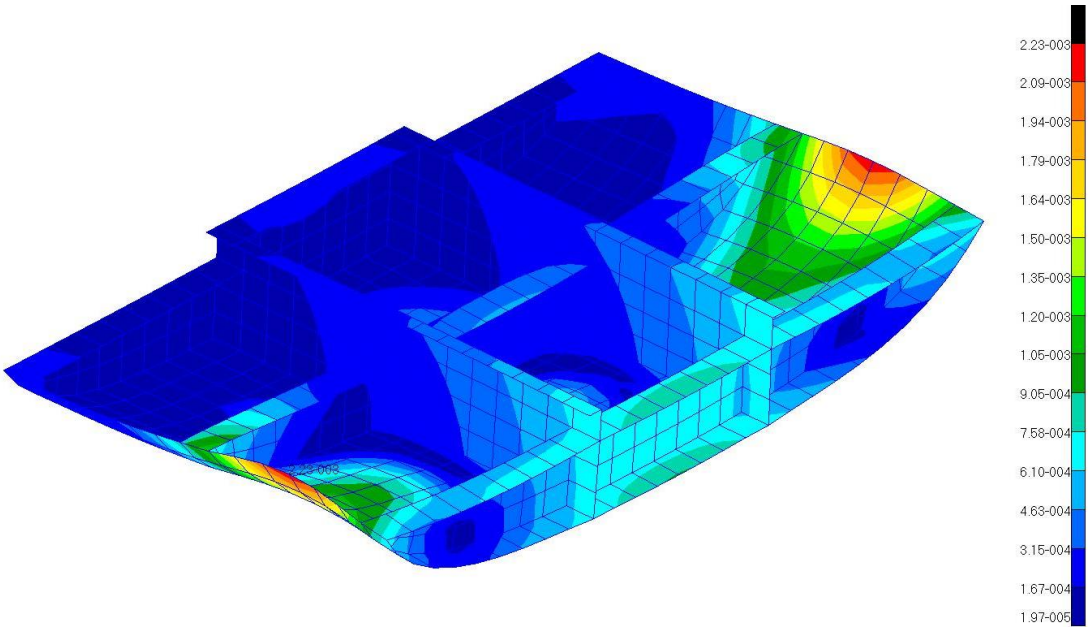


**Figure 95: Displacement (m) plot for a linear static analysis of finite element model 3**

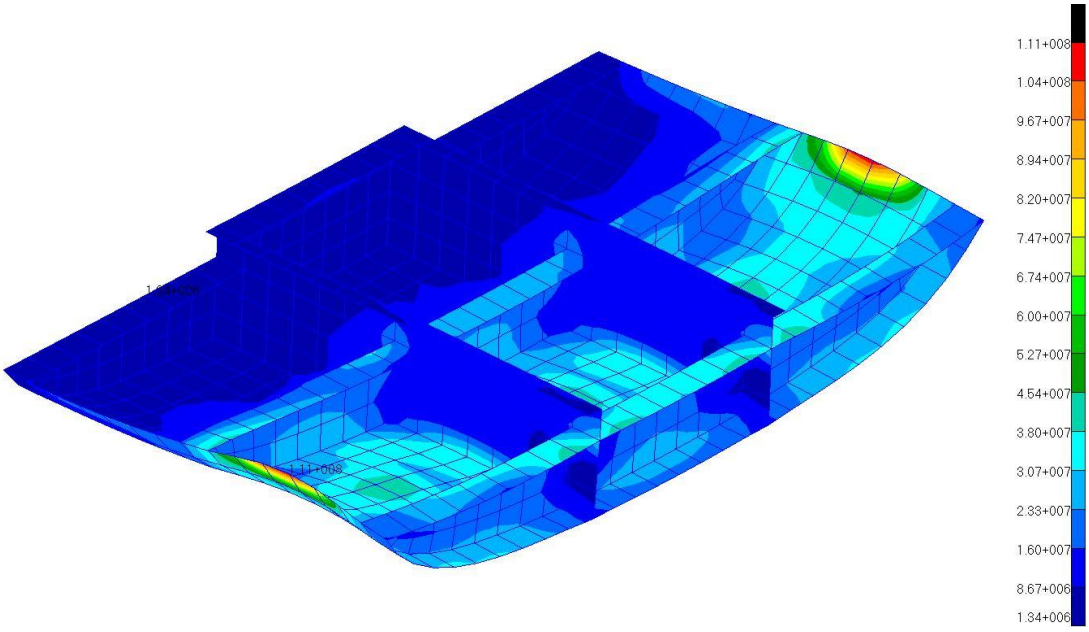


**Figure 96: von Mises stress (Pa) plot for a linear static analysis of finite element model 3**

**Table 17: Percentage error of finite element models relative to the displacement and von Mises stress results of the finite element model 1**

| FE model ID | Percentage error relative to FE model 1 | |
|---|---|---|
| | Displacement results | von Mises results |
| 1 | 0 | 0 |
| 2 | 0.9 | 0.52 |
| 3 | 0.89 | 3.8 |
| 4 | 2.63 | 7.43 |

Dynamic analyses were performed with MSC Dytran to determine how analysis run-times are affected by changes in element size. In addition to a change in the number of calculations required, a change in element size also affects the time-step required (refer to Equation 59 in Chapter 1 Section 2.5). Note that due to geometrical constraints, the elements in a particular finite element model are highly unlikely to all be exactly the same size. A vertical initial velocity of 8.52 metres per second was applied to all nodal points of the finite element models, and a rigid planar wall was defined as an impact surface. The analysis end time was set to 0.1 seconds. Table 18 shows the multiples by which the analysis run-times increased between each finite element model used for convergence testing. For example, the use of finite element model 1 is expected to multiply the required analysis run-time by 41.86 when compared to finite element model 4. This highlights the need to consider both accuracy and analysis run-time when selecting an appropriate element size.

**Table 18: Matrix indicating multiples by which analysis times are expected to increase with a decrease in element size, and therefore increase in the number of elements in MSC Dytran**

| FE model ID ⟶ / ↓ | 1 | 2 | 3 | 4 |
|---|---|---|---|---|
| 1 | 1 | 7.71 | 30.84 | 41.86 |
| 2 | | 1 | 4 | 5.43 |
| 3 | | | 1 | 1.36 |
| 4 | | | | 1 |

Ultimately, finite element model 3 was deemed to have an acceptable accuracy, along with a reasonable analysis run-time. A global element edge length of 40 millimetres was therefore selected for use in the final crashworthiness analyses presented in this study. Analysis run-time was a major deciding factor in the selection of an appropriate element edge length, as a smaller element edge length results in a significant increase in analysis run-time as previously shown in Table 18.

### 2.5.4 Terrain

Aircraft and occupant response to impact with two types of terrains were investigated for the crashworthiness analyses in this study. The first terrain was rigid and modelled with four-node quadrilateral shell elements as shown in Figure 97. The shell elements were assigned rigid properties and all nodal points were fully constrained.

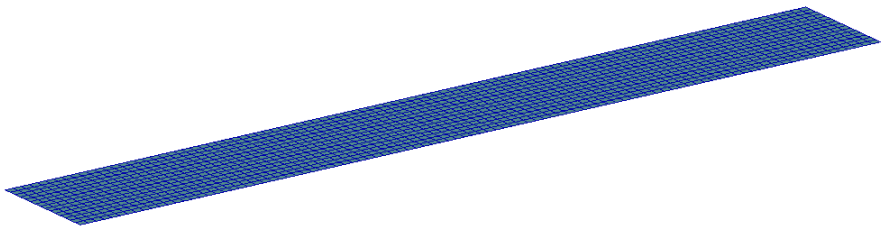

**Figure 97: Finite element representation of the rigid terrain**

The second terrain was soft soil and was modelled with eight-node solid hexahedral Euler elements. The modelling approach and material definitions used in Chapter 2 Section 3 were implemented in the development of the soft soil terrain described here. Figure 98 shows a slice through the centre of the Euler domain indicating the void and soil regions, and the use of graded meshes within MSC Dytran. For computational efficiency, graded meshes allow a fine mesh to be “glued” into a coarse mesh. As stated in Chapter 2 Section 3.4, it is recommended that the Euler element edge length be approximately equal to the Lagrange element edge length, which was approximately 40 millimetres in this study. The use of graded meshes was used to satisfy this recommendation at the expected areas of interaction between Lagrangian and Eulerian solvers. The surrounding coarse mesh allows for the flow and spallation of soft soil without effecting analysis results.

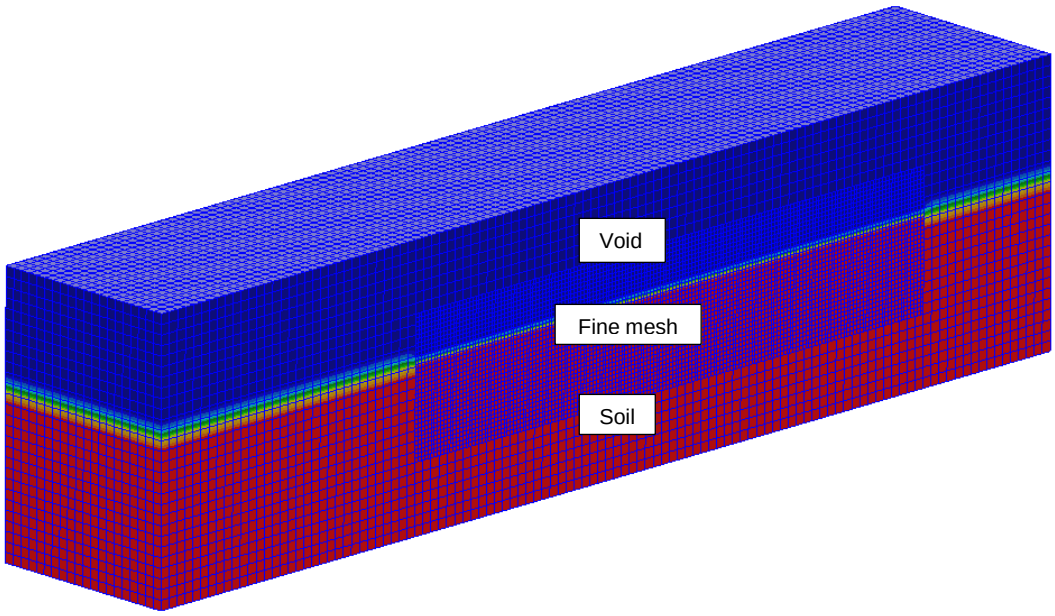


**Figure 98: Slice through the centre of the Euler domain showing the void and soil regions, and graded mesh**

### 2.5.5 Coupling surface

The coupling surface used to define the interaction between Lagrangian and Eulerian solvers is shown in Figure 99. MSC Dytran requires that the coupling surface form a closed volume, therefore dummy shell elements were used to close any holes in the coupling surface, such as the door area. Dummy shell elements have no associated stiffness and do not take part in structural calculations; therefore the shape of the dummy shell elements does not matter. It is recommended that no internal nodal points be created when using dummy shell elements as they will not move (they are not connected to structural elements). The use of internal nodal points may lead to negative volumes since the structural nodal points may move significantly beyond the internal stationary nodal points, thus causing premature termination of the analysis. Refer to Figure 100 for clarity with regards to meshing with dummy shell elements.

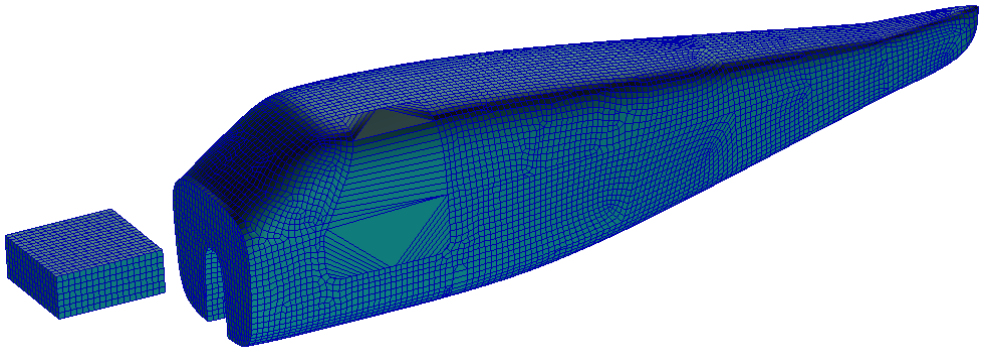

**Figure 99: Aircraft coupling surface**

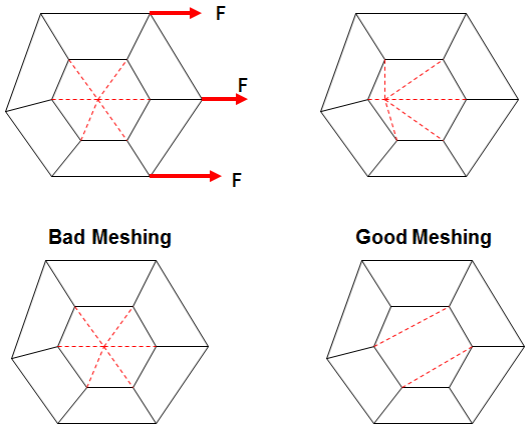


**Figure 100: Meshing with dummy shell elements**

### 2.5.6 Parameters, loads and boundary conditions

The finite element modelling techniques discussed at the subcomponent levels were implemented in the full-scale crashworthiness analyses; however additional features were required for successful full-scale analyses.

The NZEROVEL parameter within MSC Dytran was activated in the soft soil terrain analyses to set the velocity of a nodal point to zero if all the attached elements have failed (effectively the nodal point is fully constrained). This parameter applies to Lagrangian elements only and was used to limit

coupling surface deformation. When the coupling surface fails, the COUP1FL parameter was used to define the outflow of material (i.e. outflow of soil) into the coupling surface volume by specifying surrounding variables. The surrounding variable defined was the density of air for numerical stability reasons, where the density of air was assigned a value of 1.29 kilograms per cubic metre.

A maximum velocity of 150 metres per second was assumed for the Eulerian soil, which was defined with the VELMAX parameter within MSC Dytran. Without this parameter, the full-scale crash analyses always prematurely terminated, therefore this parameter was introduced for stability reasons when performing crashworthiness analyses. The maximum velocity parameter was configured to not remove the mass in the Eulerian elements in which the velocity exceeds the maximum specified velocity. Further details regarding the VELMAX parameter and its effects on the energies of the Euler material can be found in Chapter 3 Section 5.

Adaptive master-slave contact (refer to the MSC Dytran Reference Manual [54]) was used to define contact between various components of the aircraft finite element model as summarised in Table 19; however was not necessary for contact definitions where failure was not assigned to the materials (e.g. contact between two rigid components such as contact nine requires only the standard master-slave contact definition). Slave nodal point (de)activation METHOD1 was assigned to ensure the slaves nodal points will be deactivated in the contact definition once all connected elements have failed. This is especially important when using the NZEROVEL parameter to prevent contact of the occupant with a “constrained” nodal point. Some of the various entries used in the CONTACT cards for the full-scale analyses are listed in Table 20. All friction coefficients were assumed due to a lack of experimental data. A shell thickness and gap of zero millimetres was important especially for contact nine, because the rigid sleeves and pins were modelled with the same diameters.

**Table 19: Components defining master segments and slave nodal points for contact definitions**

| Contact ID | Master segments | Slave nodal points |
|---|---|---|
| 1 | Main wing spar brace | Main wing spar |
| 2 | Floor board | Lower fuselage skin, floor structure |
| 3 | Mid / side fuselage skin | Seat foam |
| 4 | Seat pan | Lower fuselage skin, floor structure |
| 5 | Mid / side fuselage skin | Seat pan |
| 6 | Glare shield | Front window |
| 7 | Wing joint side surfaces | Main wing spar side surfaces |
| 8 | Wing joint upper and lower surfaces | Main wing spar upper and lower surfaces |
| 9 | Rigid sleeve (wing joint) | Rigid pin (main wing spar) |
| 10 | *Rigid terrain | Engine |
| 11 | *Rigid terrain | Fuselage skin, fire wall, floor structure, wheel well, bulkheads, wing joints |
| 12 | Occupant (ATB model) | Seat belt |
| 13 | Seat foam back | Occupant (ATB model) |
| 14 | Seat foam bottom | Occupant (ATB model) |
| 15 | Glare shield | Occupant (ATB model) |
| 16 | Fuselage skin, floor board, windows | Occupant (ATB model) |

*Note: For crash scenarios one, two and three only (refer to Chapter 3 Section 1).

**Table 20: Various CONTACT card entries used for the full-scale crash analyses**

| Contact ID | FACT | WEIGHT | THICK | FS | FK | EXP | GAP (mm) |
|---|---|---|---|---|---|---|---|
| 1 | 0.1 | BOTH | 0 | 1 | 1 | 1 | 0 |
| 2 | 0.1 | BOTH | 0 | 0 | 0 | 0 | 0 |
| 3 | 0.1 | BOTH | 0 | 0 | 0 | 0 | 0 |
| 4 | 0.1 | BOTH | 0 | 0 | 0 | 0 | 0 |
| 5 | 0.1 | BOTH | 0 | 0 | 0 | 0 | 0 |
| 6 | 0.1 | BOTH | 0 | 0 | 0 | 0 | 0 |
| 7 | 0.1 | BOTH | 0 | 1 | 1 | 1 | 0 |
| 8 | 0.1 | BOTH | 0 | 1 | 1 | 1 | 0 |
| 9 | 0.1 | NONE | 0 | 0 | 0 | 0 | 0 |
| 10 | 0.1 | NONE | 0 | 1 | 1 | 1 | 0.01 |
| 11 | 0.1 | SLAVE | 0 | 1 | 1 | 1 | 0.01 |
| 12 | 0.1 | SLAVE | 1 | 1 | 1 | 1 | 0 |
| 13 | 0.01 | MASTER | 1 | 0.62 | 0.62 | 1 | 0.002 |
| 14 | 0.01 | MASTER | 1 | 0.62 | 0.62 | 1 | 0.002 |
| 15 | 0.01 | MASTER | 1 | 0.62 | 0.62 | 1 | 0.002 |
| 16 | 0.01 | MASTER | 1 | 0.62 | 0.62 | 1 | 0.002 |

where:
FACT = contact force scale factor
WEIGHT = mass-weighting factor
THICK = shell thickness scale factor
GAP = Artificial contact thickness
FS = static coefficient of friction
FK = kinetic coefficient of friction
EXP = exponential decay coefficient

Refer to the MSC Dytran Reference Manual [54] for further details.

Initial velocities required for each crash scenario investigated (refer to Chapter 3 Section 1) were applied to all nodal points of the aircraft. The initial velocities required for the occupants were defined by editing the ATB input files (refer to Figure 48).

# CHAPTER 3: FULL-SCALE MODEL RESULTS AND DISCUSSION

## 3.1 Introduction

Crashworthiness analysis results for six different crash scenarios are presented in this chapter. Three crash scenarios were demonstrated with a rigid impact terrain and three with a soft soil impact terrain with varying aircraft impact and pitch angles. Although unlikely in a typical crash scenario, the yaw and roll angles were set to zero degrees for all scenarios. The resultant initial velocity of the aircraft was based on a typical clean stall speed of a four-seater general aviation aircraft, being approximately 64 knots (i.e. 32.92 metres per second). A summary of each crash scenario is shown in Table 21.

**Table 21: Summary of demonstrated crash scenarios**

| Scenario | Terrain | $v_R$ (m/s) | $v_V$ (m/s) | $v_H$ (m/s) | Impact angle (degrees)* | Pitch angle (degrees)* |
|---|---|---|---|---|---|---|
| 1 | Rigid | 32.92 | 2.87 | 32.79 | 5 | -5 |
| 2 | Rigid | 32.92 | 5.72 | 32.42 | 10 | -10 |
| 3 | Rigid | 32.92 | 8.52 | 31.80 | 15 | -15 |
| 4 | Soft soil | 32.92 | 2.87 | 32.79 | 5 | -5 |
| 5 | Soft soil | 32.92 | 5.72 | 32.42 | 10 | -10 |
| 6 | Soft soil | 32.92 | 8.52 | 31.80 | 15 | -15 |

Notation:

v = velocity

Subscripts R, V, and H refer to resultant, vertical, and horizontal respectively.

* Note: Impact and pitch angles reference system according to Figure 34.

All six scenarios successfully reached the set analysis end time of 0.18 seconds without the occurrence of numerical instabilities or error. A DELL Precision T7500 computer with two Intel(R) Xeon(R) X5687 (3.6 GHz) central processing units, and 48 gigabytes random-access memory, was used for analyses. The analysis run-time was approximately 2 hours 40 minutes each for crash scenarios one to three. The analysis run-time was approximately eight days (192 hours) each for crash scenarios four to six, with the fastest analysis run-time being approximately 172 hours.

Results for the shoulder harness force, force between the pelvis and lumbar spine, and head injury criterion were filtered in MATLAB using a low-pass digital Butterworth filter with zero-phase distortion. The normalised cut-off frequency and filter order were set to 0.2 and 2 respectively for crash scenarios two, three and six. The normalised cut-off frequency and filter order were set to 0.1 and 2 respectively for crash scenarios one, four and five. The fast Fourier transform was used to determine the main frequency components, thereby enabling the selection of suitable cut-off frequencies. Refer to Appendix A for further details regarding the low-pass digital Butterworth filter and fast Fourier transform.

The main wing spar was omitted from the time sequence and failure fringe plots presented below as it was only included in the analyses to represent the inertia effects of the wings. The main wing spar failed in the vicinity of the wing joints for all crash scenarios due to the high decelerations experienced during impact. An example of the main wing spar failure is shown in Figure 101. In the work performed by Bossak and Kaczkowski [4], failure of the wing spar was also observed for the crash analysis of a composite light aircraft. Additionally, Terry et al. [52] performed experiments of “crashworthy” small composite airframes impacting into hard and soft soil terrains, where main wing spar failure was also observed for impacts into both terrains. The omission of the main wing spar also assisted in presenting clearer results.

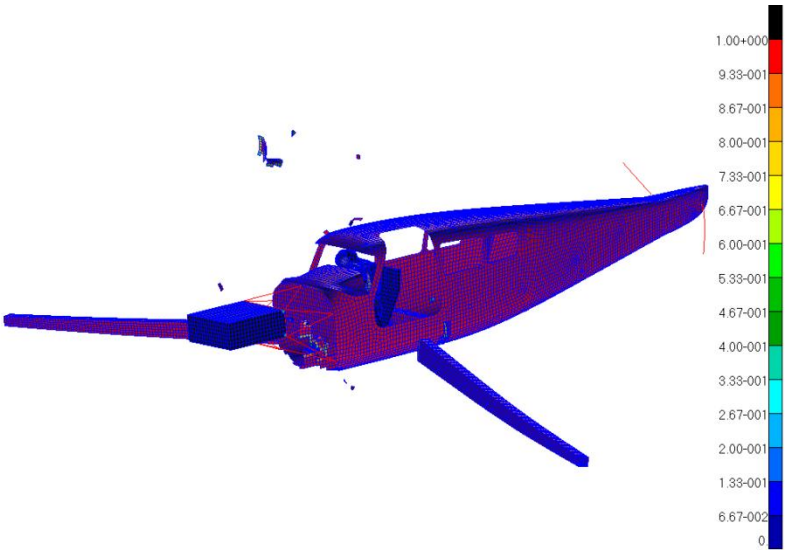


**Figure 101: Crash scenario 5 at time 0.13 seconds, showing failure of the main wing spar**

## 3.2 Rigid terrain impacts

Time sequence pictures for crash scenarios one, two and three (rigid terrain impacts) are shown in Figure 102, Figure 105 and Figure 108 respectively. These figures indicate a sliding impact and show positive pitching of the aircraft. If the analysis end time were to be extended, tail slap-down may possibly occur depending on the failure response of the fuselage.

Failure fringe plots showing initial and final structural failure of the fuselage for crash scenarios one, two and three are shown in Figure 103, Figure 106 and Figure 109 respectively. As can be seen, initial failure occurred locally at the point of contact with the impact terrain, and concentrated loading was introduced into the stiffest parts of the aircraft structure. Additionally, an increase in aircraft impact and pitch angles resulted in an increase of structural failure. This can be seen for crash scenarios two and three where the floor structure significantly fragmented and the seat no longer had any attachment points.

Figure 104, Figure 107, and Figure 110 show the occupant results for crash scenarios one, two and three respectively. The results presented here for crashworthiness assessment are the shoulder harness force, compressive force between the pelvis and lumbar spine, and the head injury criterion. Although the occupant results may all be within the survivable limits defined in Chapter 1 Section 4, it must be noted that significant damage to the floor structure occurred for crash scenarios two and three, resulting in seat detachment. Seat detachment significantly compromises occupant survivability. Additionally, the occupant results presented here may not be suitable for certification purposes as per FAR 23.562 subpart B (refer to Chapter 1 Section 4) as the 50$^{th}$ percentile adult male Hybrid III was used for analyses, not the recommended Hybrid II or FAA Hybrid III.

**Crash scenario 1**

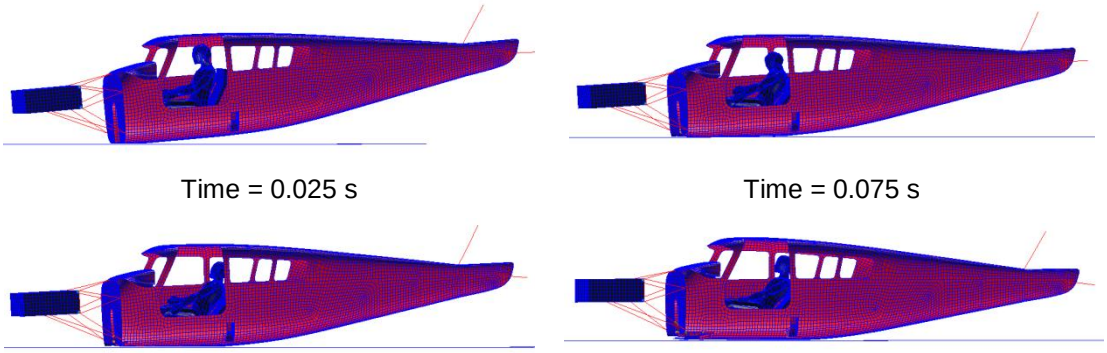


**Figure 102: Time sequence for crash scenario 1**

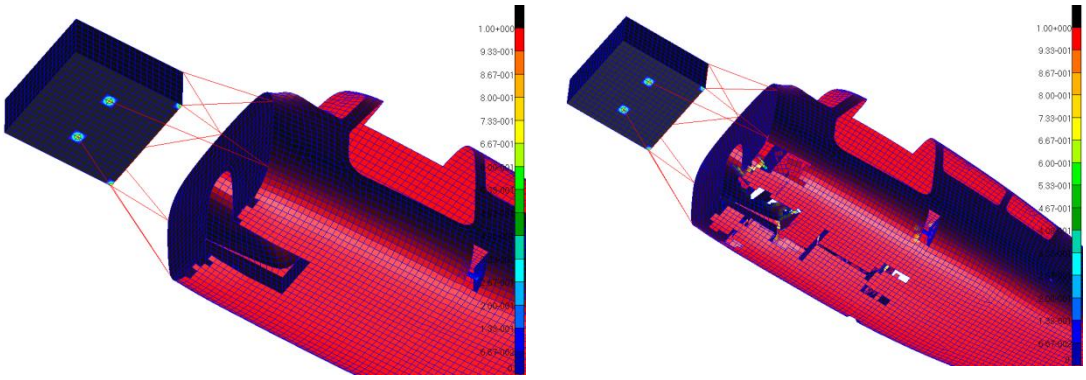

Time = 0.025 s  Time = 0.18 s

**Figure 103: Failure fringe plot for crash scenario 1, showing initial and final structural failure**

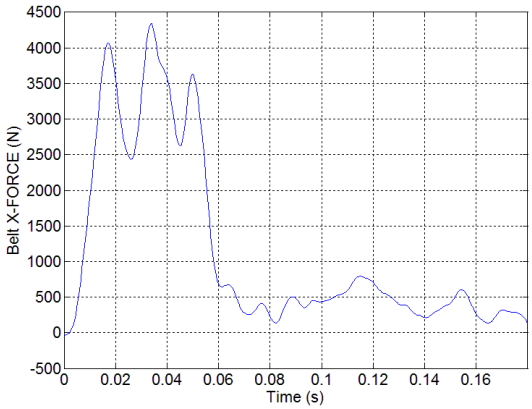


Shoulder harness force

(peak force = 4338 N)

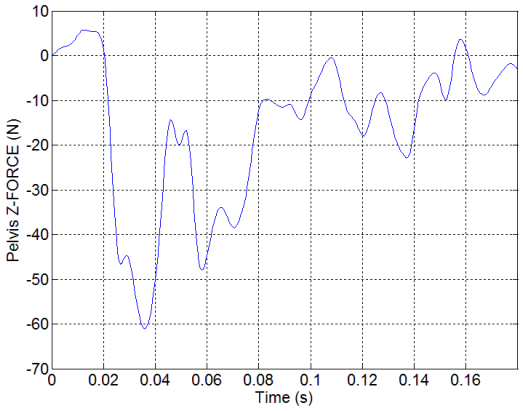


Force between pelvis and lumbar spine

(peak force = -61.17 N)

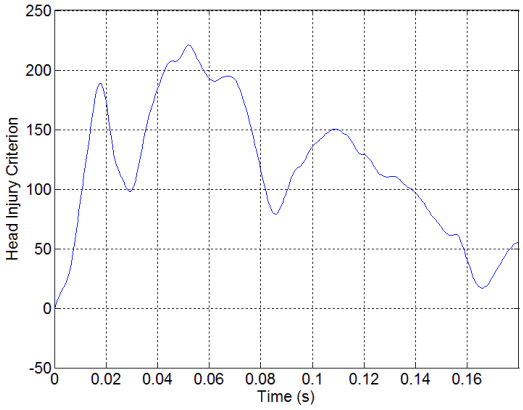


Head Injury Criterion (peak HIC = 220.9)

**Figure 104: Occupant results for crash scenario 1**

**Crash scenario 2**

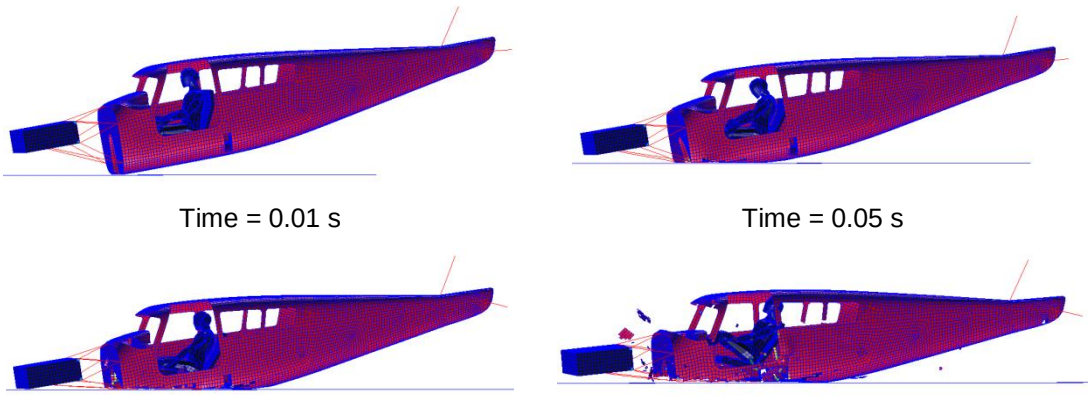

Time = 0.01 s | Time = 0.05 s

Time = 0.1 s | Time = 0.18 s

**Figure 105: Time sequence for crash scenario 2**

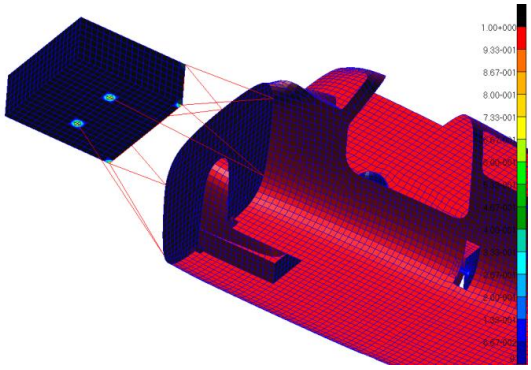

Time = 0.01 s

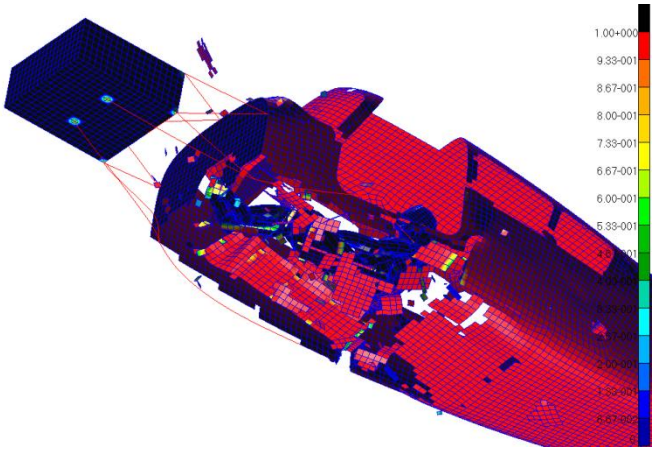

Time = 0.18 s

**Figure 106: Failure fringe plot for crash scenario 2, showing initial and final structural failure**

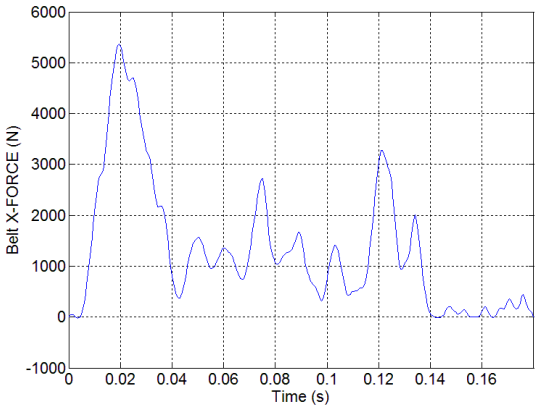


Shoulder harness force

(peak force = 5366 N)

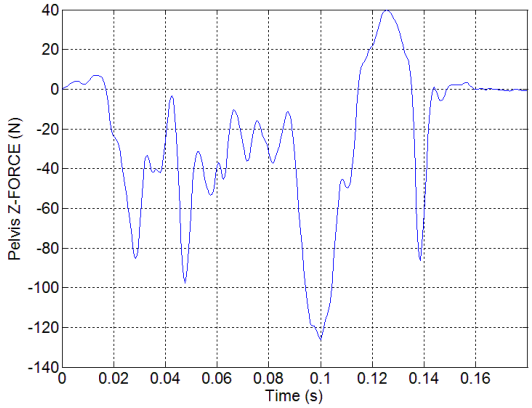


Force between pelvis and lumbar spine

(peak force = -126.1 N)

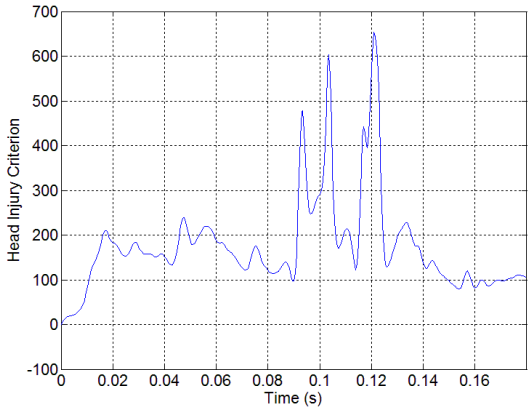


Head Injury Criterion (peak HIC = 653.9)

**Figure 107: Occupant results for crash scenario 2**

**Crash scenario 3**

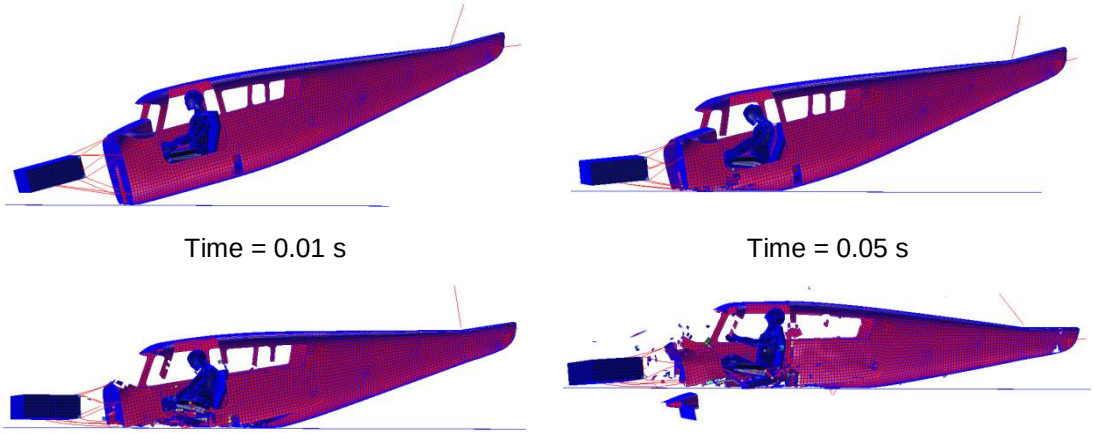

Time = 0.01 s | Time = 0.05 s

Time = 0.1 s | Time = 0.18 s

**Figure 108: Time sequence for crash scenario 3**

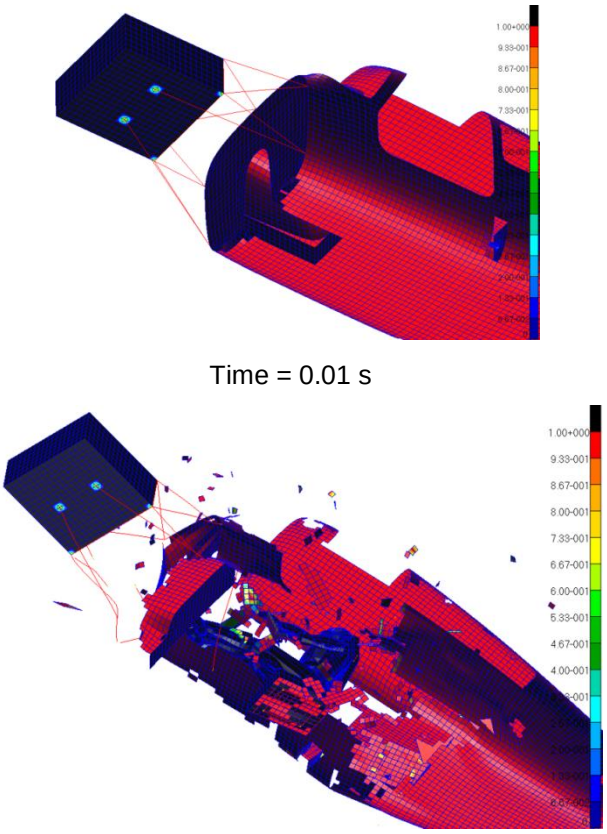

Time = 0.01 s

Time = 0.18 s

**Figure 109: Failure fringe plot for crash scenario 3, showing initial and final structural failure**

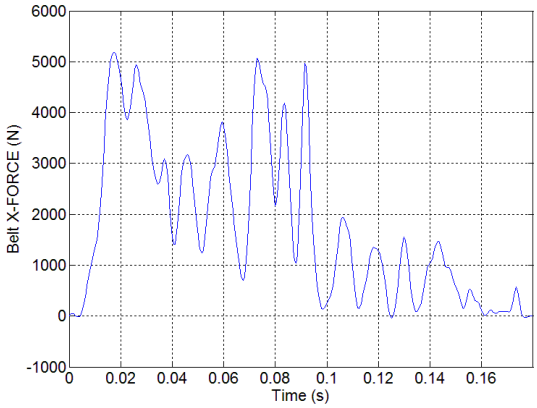


Shoulder harness force

(peak force = 5188 N)

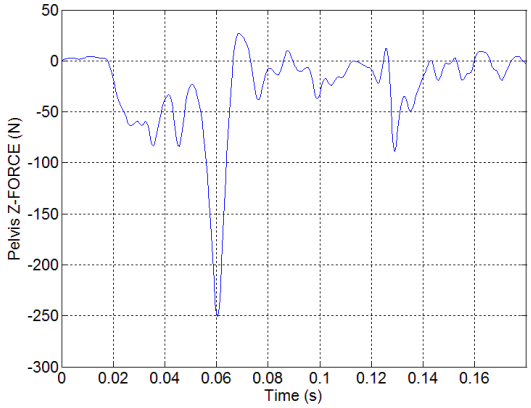


Force between pelvis and lumbar spine

(peak force = -250.5 N)

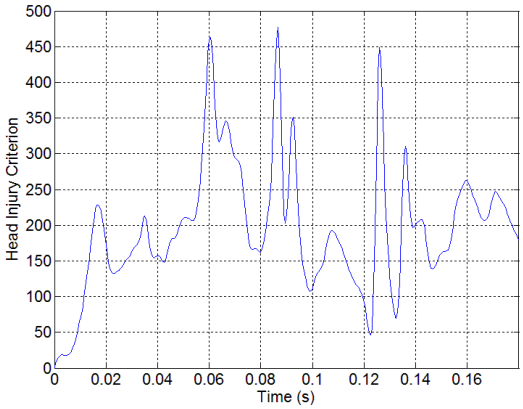


Head Injury Criterion (peak HIC = 477.2)

**Figure 110: Occupant results for crash scenario 3**

## 3.3 Soft soil impacts

Time sequence pictures for crash scenarios four, five and six (soft soil terrain impacts) are shown in Figure 111, Figure 114 and Figure 117 respectively. The pictures in the left column of the figures were post processed in MSC Patran and exclude the soft soil, whereas the pictures in the right column were post processed in Paraview and include material fraction iso-surface plots of the soft soil. These figures indicate digging in of the aircraft fuselage into the soft soil, resulting in negative pitching and high deceleration forces.

Failure fringe plots showing initial and final structural failure of the fuselage for crash scenarios four, five and six are shown in Figure 112, Figure 115 and Figure 118 respectively. Initial failure occurred on the firewall for all three crash scenarios due to the pressure applied by the soft soil. The final failure results for all three crash scenarios show relatively minor damage to the fuselage skin at the front underside of the fuselage and the floor structure. Significant damage to the wheel well was observed for crash scenarios five and six, and seat detachment was observed for crash scenario six only due to high deceleration forces. Once again, seat detachment significantly compromises occupant survivability. It is noted that the wheel well damage may be reduced by inclusion of the landing gear structure, which may possibly reinforce the surrounding area of the wheel well. The failure fringe plots indicate that distributed loading was introduced into the fuselage skin, which is supported by the observation that failure did not occur along the webs of the floor structure (unlike for the rigid terrain impacts).

Figure 113, Figure 116 and Figure 119 show the occupant results for crash scenarios four, five and six respectively. The results presented here for crashworthiness assessment are the shoulder harness force, compressive force between the pelvis and lumbar spine, and the head injury criterion. Once again, the occupant results presented here may not be suitable for certification purposes as per FAR 23.562 subpart B (refer to Chapter 1 Section 4) as the $50^{th}$ percentile adult male Hybrid III was used for analyses, not the recommended Hybrid II or FAA Hybrid III.

**Crash scenario 4**

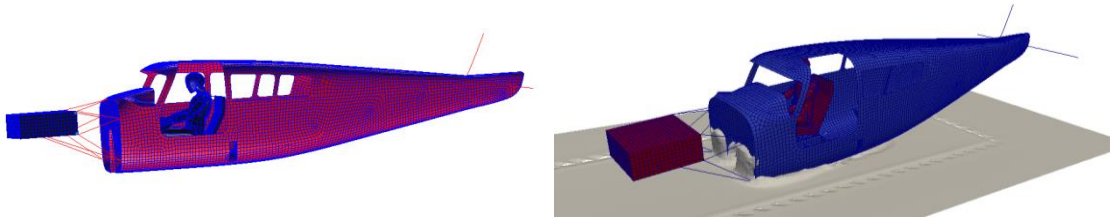

Time = 0.065 s

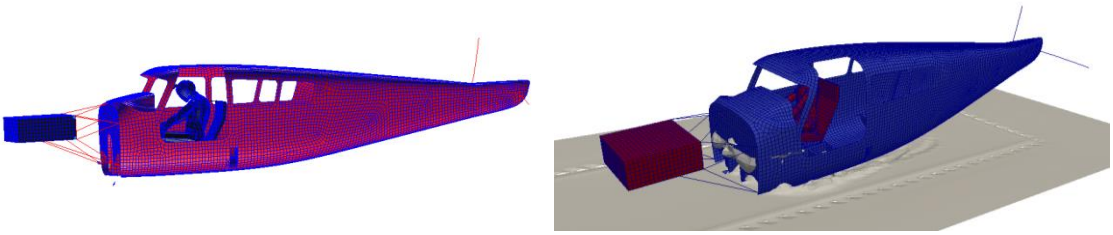

Time = 0.1 s

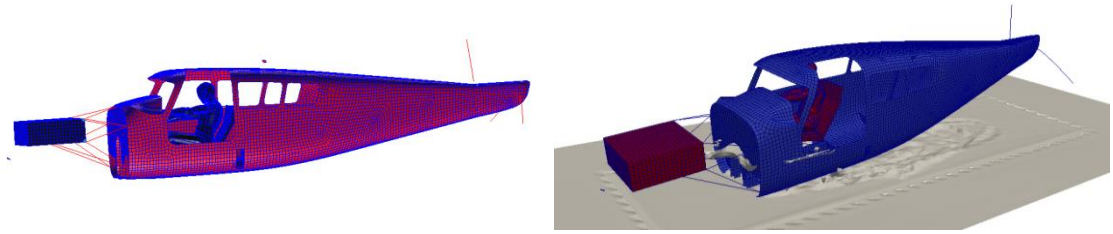

Time = 0.15 s

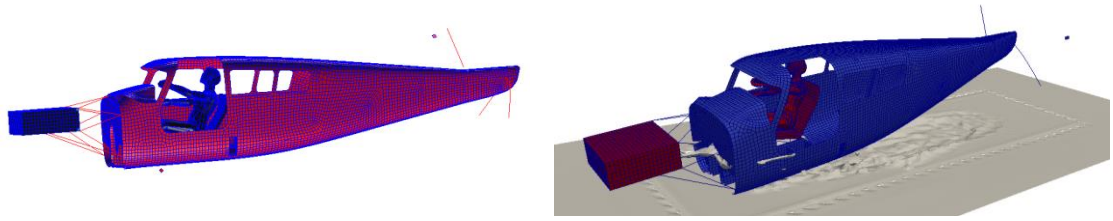

Time = 0.18 s

**Figure 111: Time sequence for crash scenario 4**

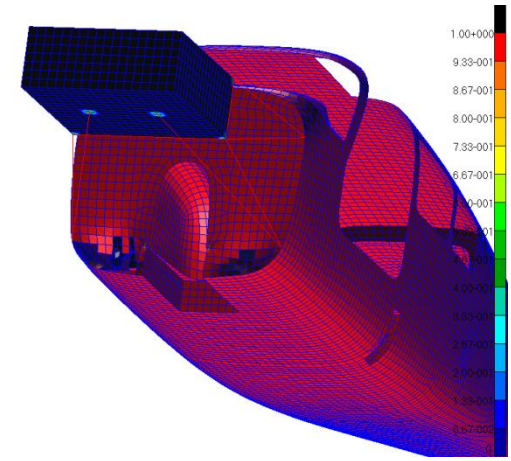


Time = 0.065 s

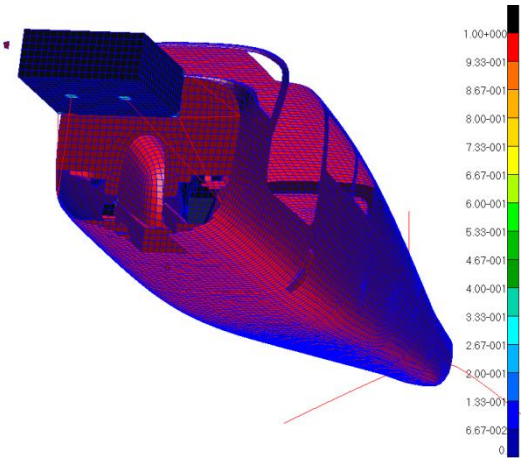


Time = 0.18 s

**Figure 112: Failure fringe plot for crash scenario 4, showing initial and final structural failure**

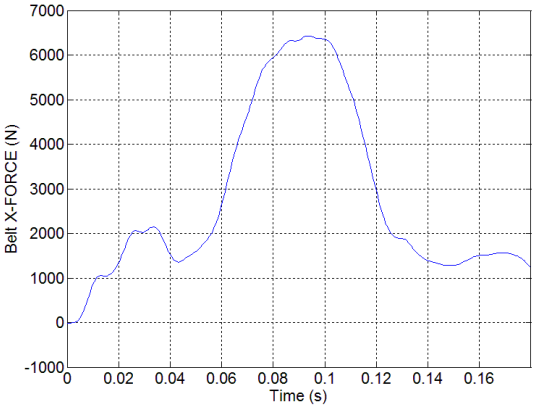


Shoulder harness force

(peak force = 6426 N)

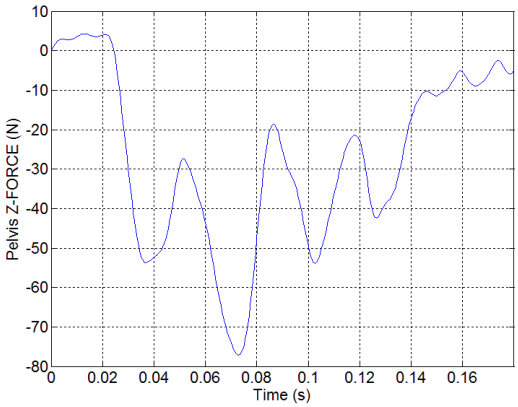


Force between pelvis and lumbar spine

(peak force = -11.12 N)

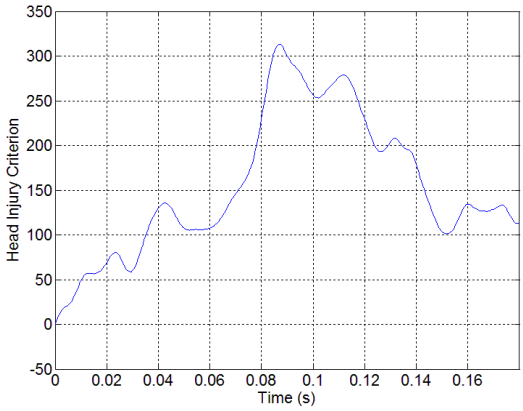


Head Injury Criterion (peak HIC = 313.2)

**Figure 113: Occupant results for crash scenario 4**

**Crash scenario 5**

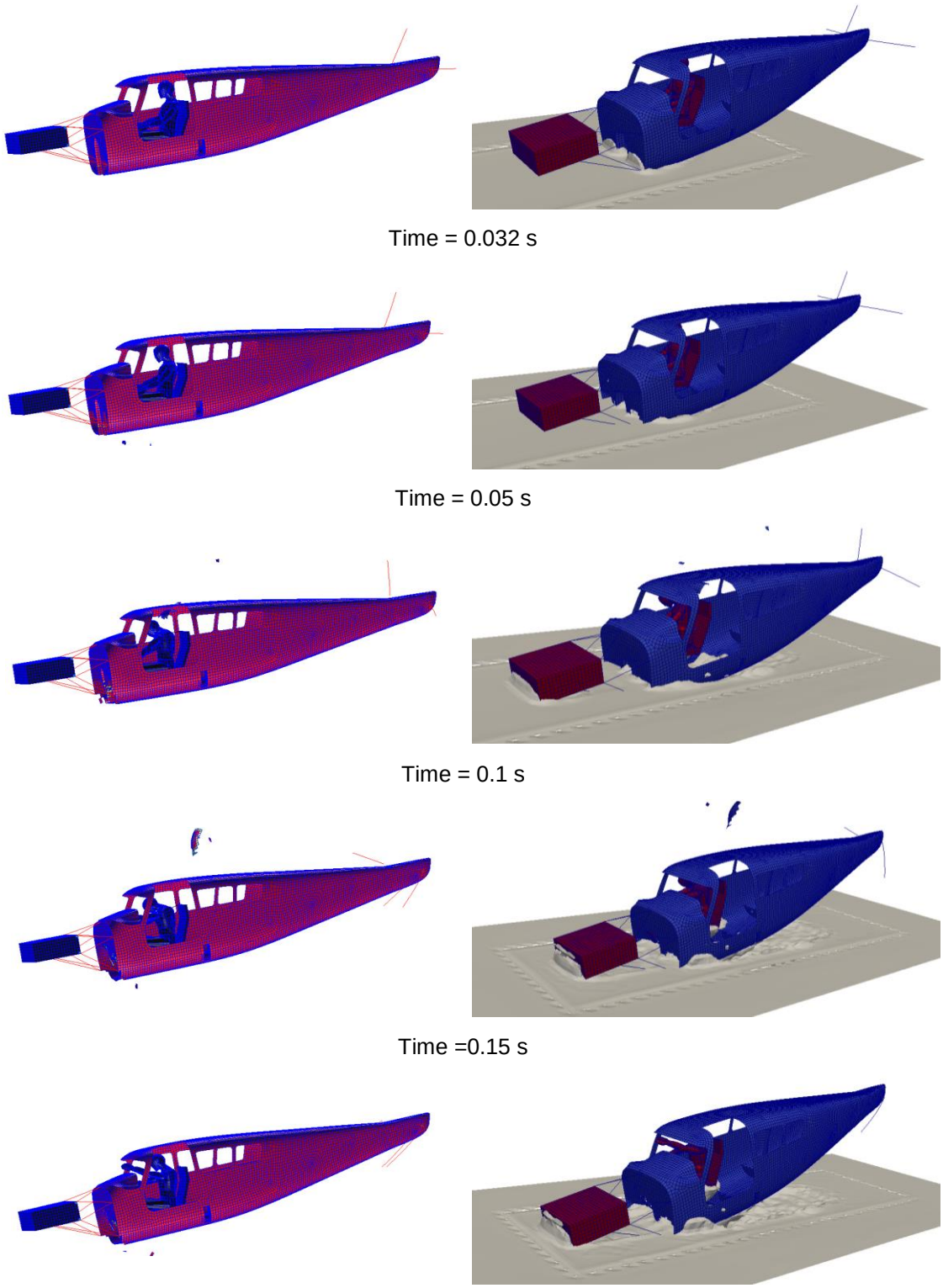


**Figure 114: Time sequence for crash scenario 5**

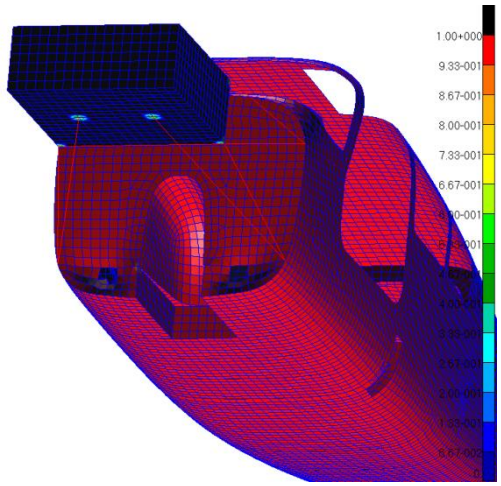


Time = 0.032 s

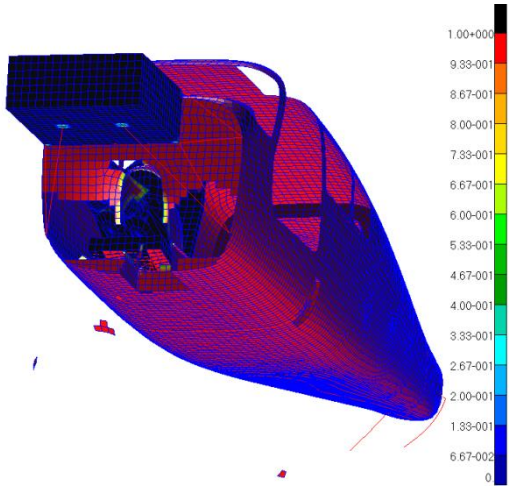


Time = 0.18 s

**Figure 115: Failure fringe plot for crash scenario 5, showing initial and final structural failure**

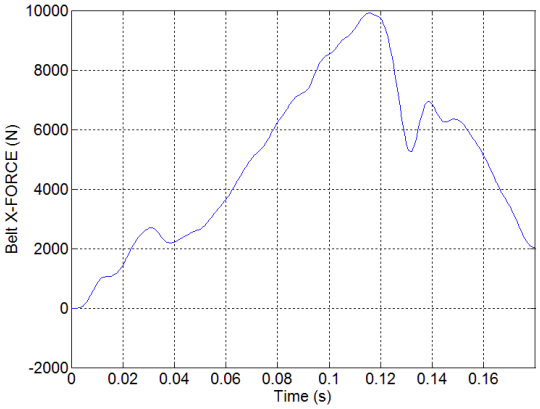


Shoulder harness force

(peak force = 9907 N)

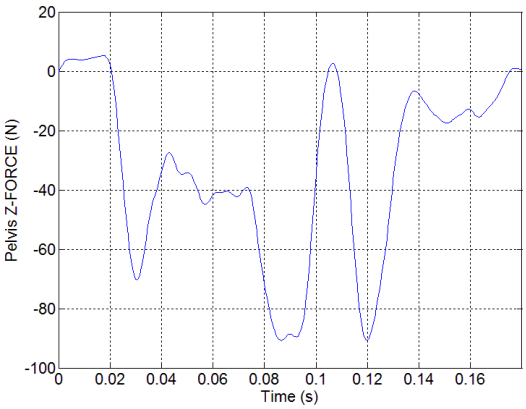


Force between pelvis and lumbar spine

(peak force = -90.84 N)

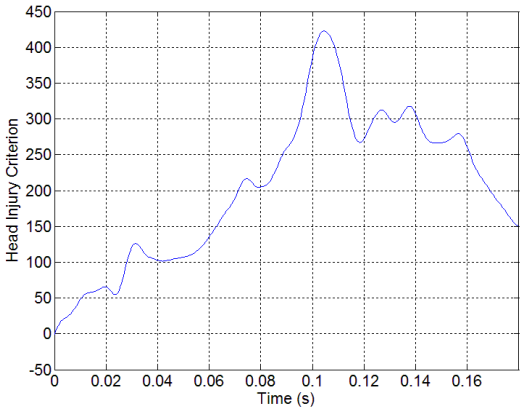


Head Injury Criterion (peak HIC = 422.7)

**Figure 116: Occupant results for crash scenario 5**

## Crash scenario 6

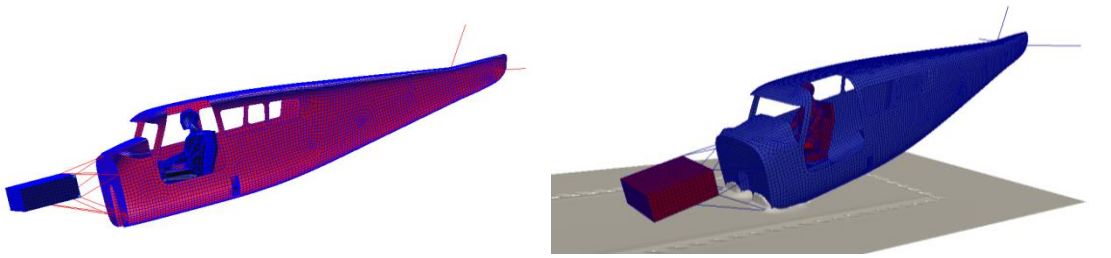

Time = 0.025 s

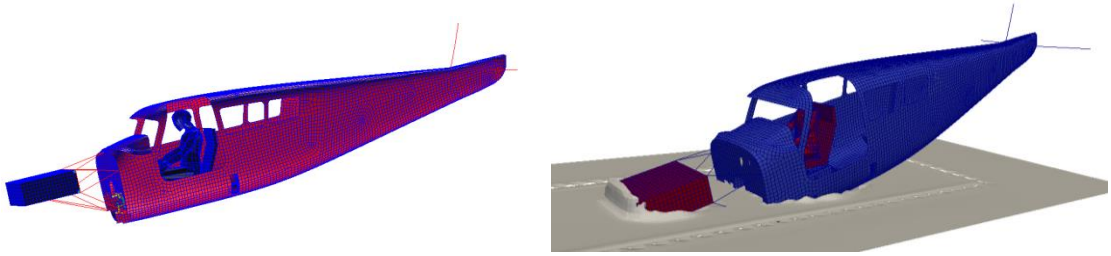

Time = 0.05 s

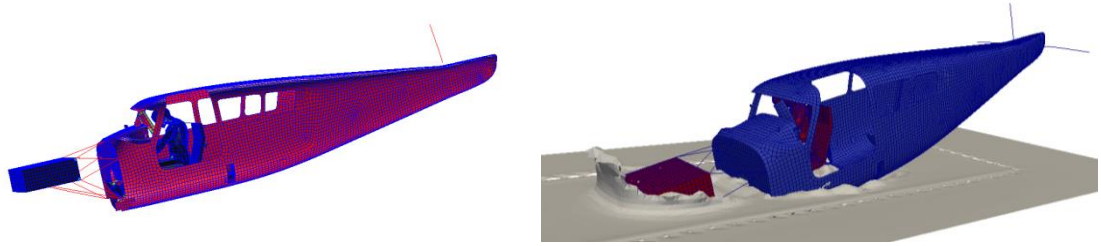

Time = 0.075 s

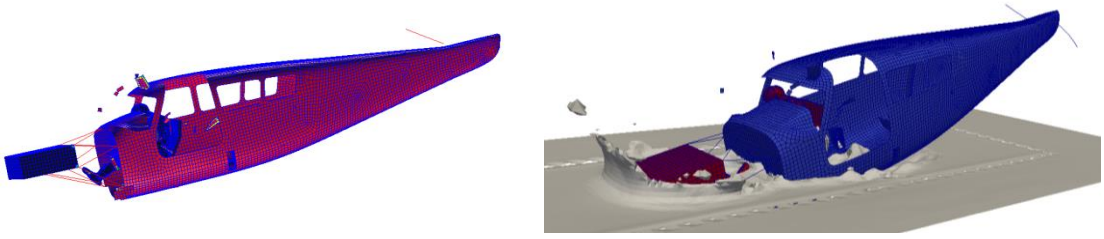

Time = 0.1 s

**Figure 117: Time sequence for crash scenario 6**

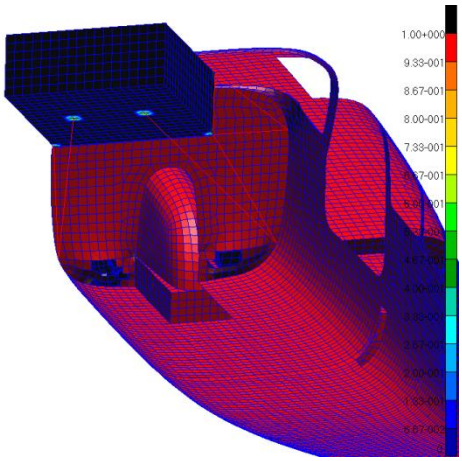


Time = 0.025 s

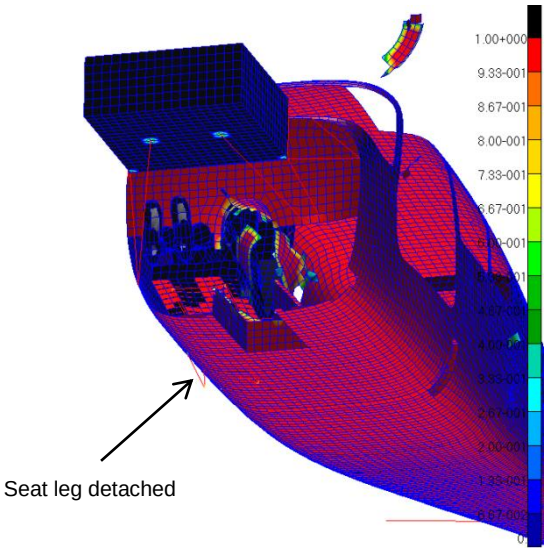


Time = 0.1 s

**Figure 118: Failure fringe plot for crash scenario 6, showing initial and final structural failure**

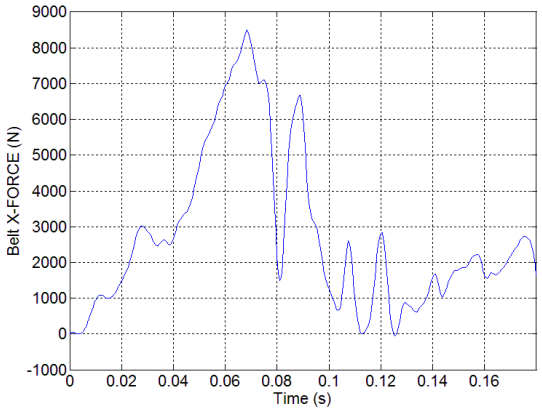


Shoulder harness force

(peak force = 8492 N)

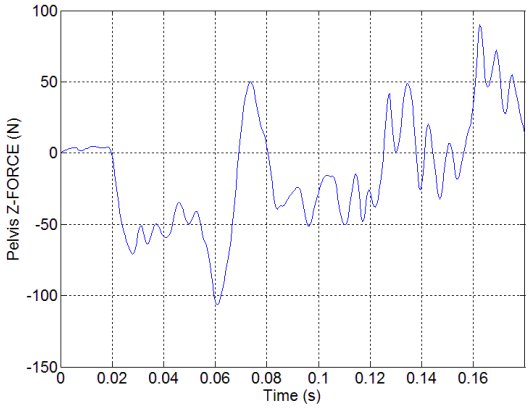


Force between pelvis and lumbar spine

(peak force = -106.1 N)

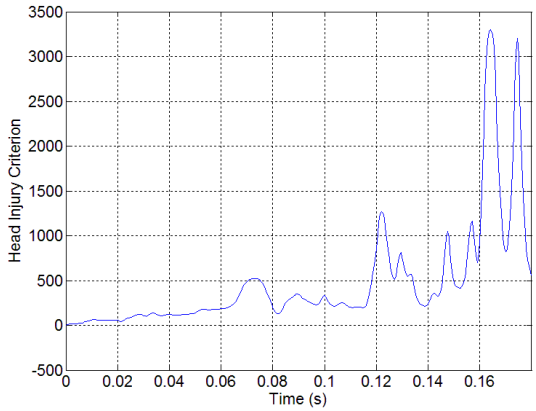


Head Injury Criterion (peak HIC = 3300)

**Figure 119: Occupant results for crash scenario 6**

## 3.4 Discussion of occupant results

The peak head injury criterion results and shoulder harness forces were greater for the impacts into soft soil when compared to impacts into rigid terrain, except for crash scenario five where the head injury criterion was lower. These greater results were expected as impacts into soft terrains typically produce high aircraft decelerations in the longitudinal direction and stop the aircraft abruptly due to digging in of the aircraft into the soft terrain. The head injury criterion result for crash scenario two may be higher than in crash scenario five due to seat detachment in crash scenario two, which may result in impact of the occupant with the aircraft structure. The significantly

large head injury criterion result for crash scenario six may also be a result of impact with the aircraft structure after seat detachment. For all impacts into soft soil, the force between the pelvis and lumbar spine was lower when compared to impacts into rigid terrain. This result was expected as high aircraft decelerations in the vertical direction are typical of impacts into hard terrains.

## 3.5 Energies of the Euler material

The kinetic, internal, and distortional energies of the Euler material (i.e. soft soil) are presented as a quality check for the impact analyses into soft soil. Figure 120 presents the energy results for crash scenarios four, five and six; with the maximum velocity of the Eulerian mesh set to 150 meters per second and was configured to not remove the mass in the Eulerian elements in which the velocity exceeds the maximum specified velocity (i.e. PARAM,VELMAX,150,NO). These energy results correspond to the analysis results presented in Chapter 3 Section 3. The kinetic and distortional energies appear to be reasonable; however sudden increases in internal energy are observed for crash scenarios four, five and six.

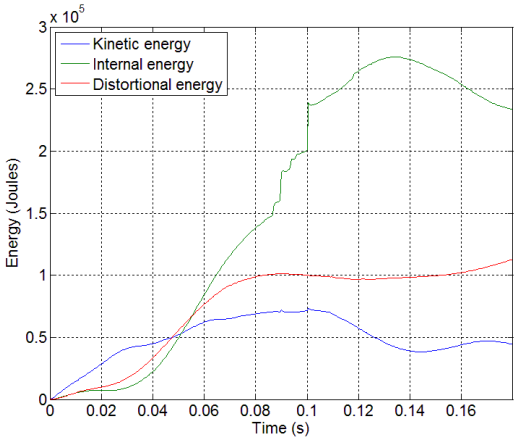


Crash scenario 4

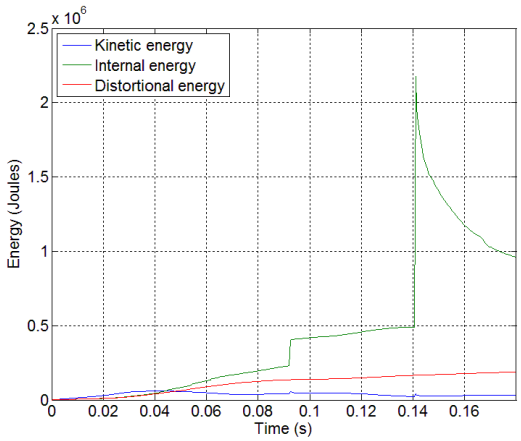


Crash scenario 5

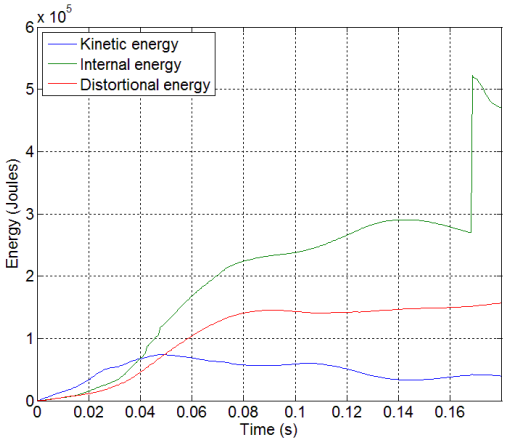


Crash scenario 6

**Figure 120: Euler energies for PARAM,VELMAX,150,NO**

The maximum velocity of the Eulerian mesh was varied to investigate its effect on the energies of the Euler material, as it was previously noticed (refer to Chapter 2 Section 5.6) that this parameter has a significant effect on analysis stability. Figure 121 presents the energy results for crash scenarios five and six, with the maximum velocity of the Eulerian mesh set to 75 meters per second and was configured to not remove the mass in the Eulerian elements in which the velocity exceeds the maximum specified velocity (i.e. PARAM,VELMAX,75,NO). The magnitudes of the sudden increases in internal energy are significantly reduced when compared with the results presented in Figure 120.

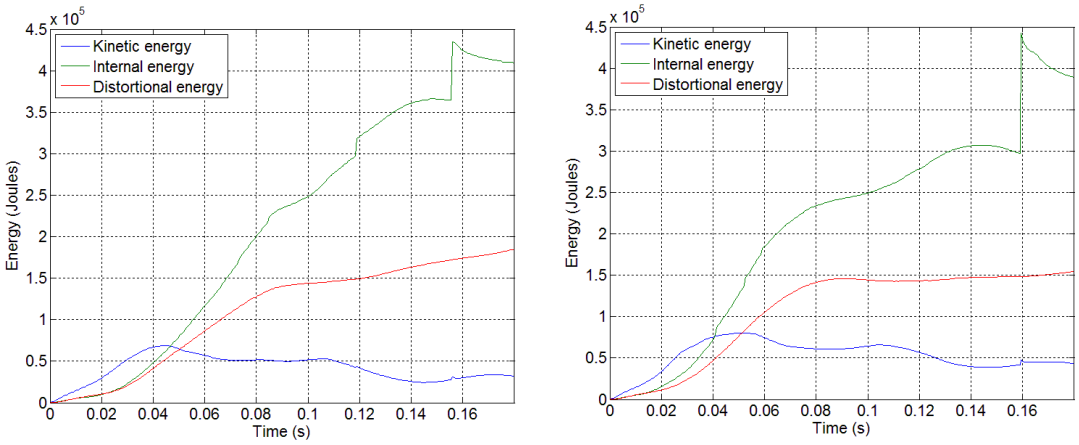


Crash scenario 5 Crash scenario 6

**Figure 121: Euler energies for PARAM,VELMAX,75,NO**

Figure 122 presents the energy results for crash scenarios five and six, with the maximum velocity of the Eulerian mesh set to 50 meters per second and was configured to not remove the mass in the Eulerian elements in which the velocity exceeds the maximum specified velocity (i.e. PARAM,VELMAX,50,NO). Sudden increases in internal energy occur significantly earlier in time when compared to Figure 121; however the maximum values are similar.

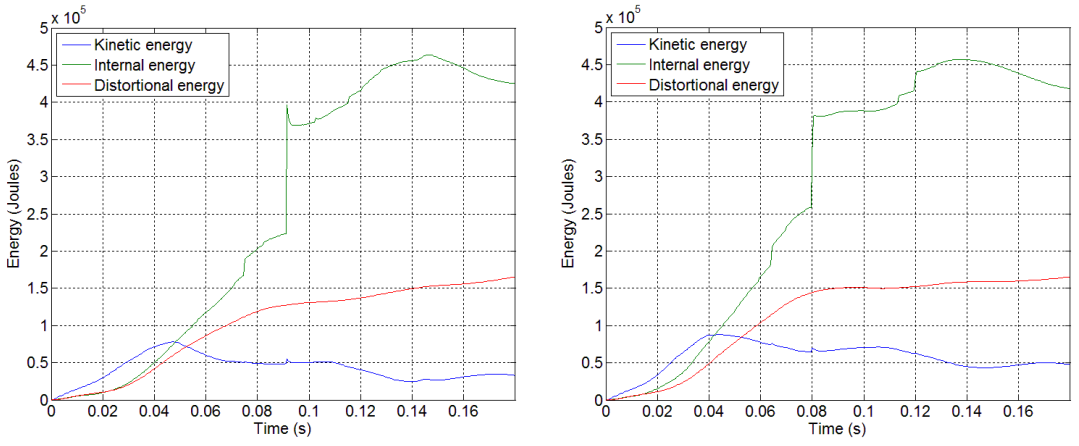


Crash scenario 5 Crash scenario 6

**Figure 122: Euler energies for PARAM,VELMAX,50,NO**

The energy results for crash scenario four were not presented in Figure 121 and Figure 122 as it was deemed unnecessary because the sudden increases in internal energy for crash scenarios five and six were relatively large when compared to crash scenario four.

Two additional analyses were performed for crash scenario five to determine the effect of configuring the maximum velocity in the Eulerian mesh parameter to remove the mass in the Eulerian elements in which the velocity exceeds the maximum specified velocity. The energy results are shown in Figure 123 for the maximum velocity in the Eulerian mesh set to 150 and 75 metres per second. The energies experience no sudden increases for a maximum velocity of 150 metres per second and when the mass in the Eulerian elements is removed; however a small sudden increase in internal energy still exists for a maximum velocity of 75 metres per second.

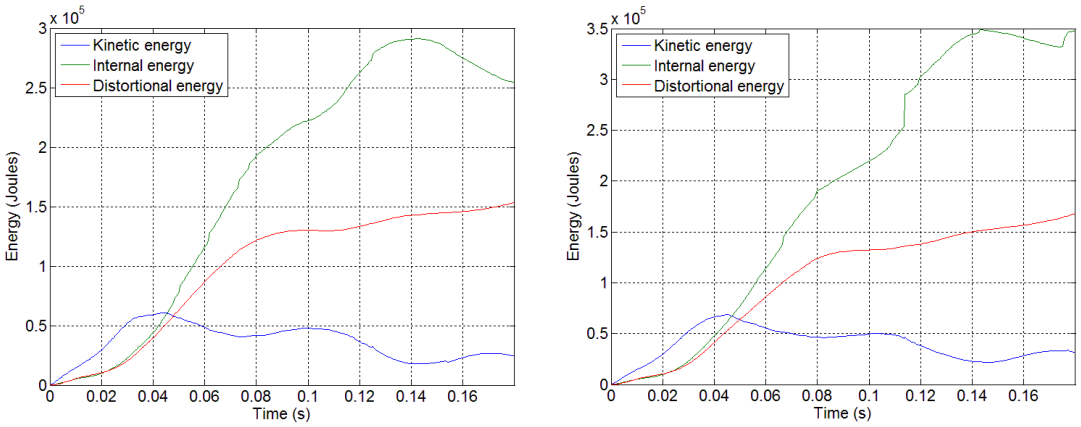


PARAM,VELMAX,150,YES PARAM,VELMAX,75,YES

**Figure 123: Energies for crash scenario five, showing the effect of mass removal in Eulerian elements in which the velocity exceeds the maximum specified velocity**

Internal energy consists of both hydrostatic and deviatoric stress components, whilst distortional energy consists of a deviatoric stress component only. In combination with the fact that the sudden increase in

internal energy occurs sometime after impact and failure of the aircraft structure, the sudden increase in internal energy is therefore believed to be due to the compression (hydrostatic component) of the Euler material, since the distortional energy appears to be reasonable. The time-delay is believed to allow for a pressure build-up of the Euler material prior to the sudden increase in internal energy. Additionally, the maximum velocity of the Eulerian mesh parameter manipulates the pressure calculation, and would therefore have an effect on the internal energy as previously shown.

Still, the specific reason(s) for the sudden increases in internal energy requires further investigation. Although the sudden increase in internal energy exists (except for PARAM,VELMAX,150,YES in Figure 123), it is currently believed that the analyses are reasonable as the phenomenon occurs sometime after initial impact and failure of the aircraft structure. Additionally, negligible differences in the overall response of the aircraft structure and occupant were observed with varying the maximum velocity of the Eulerian mesh and whether the mass in the Eulerian elements in which the velocity exceeds the maximum specified velocity is removed or not.

# CHAPTER 4: CONCLUSIONS AND FUTURE WORK

An explicit nonlinear dynamic finite element based methodology was successfully developed and implemented for investigating the crashworthiness of a small lightweight fibre reinforced composite aircraft with occupants, thus satisfying the primary aim of this study. The aircraft was analysed as it crashed into soft soil and the FEA software MSC Dytran was selected for this purpose. A “building block” approach was used to develop accurate numerical modelling techniques prior to the implementation of the full-scale crash analyses. Once the blocks produced satisfactory results in themselves, they were then integrated in order to achieve the abovementioned aim. The sub-components (or blocks) were the occupant (viz, FEA of the human bodies’ response to impact), (FEA of) soft soil impact and (FEA of) fibre reinforced plastic composite structures.

The technique required to examine the dynamic response of an occupant with MSC Dytran, integrated with the Articulated Total Body (ATB) model, was demonstrated through the analysis of a sled test. The 50$^{th}$ percentile adult male (occupant of average height and mass) Hybrid III anthropomorphic test device (ATD) was used to replicate the human body response in the sled test. The ATB model was used to numerically represent the ATD. The numerical results were found to be comparable to the experimental results found in the literature. Damage to biological tissue could not be predicted as the ATB model implemented in this study consists of rigid ellipsoids and is therefore non-deformable. Additionally, representation of the 50$^{th}$ percentile adult male Hybrid II ATD is recommended for future analyses as it satisfies the certification requirements of Federal Aviation Regulation (FAR) 23.562 subpart C for emergency landing dynamic conditions, unlike for the 50$^{th}$ percentile adult male Hybrid III ATD used in this study. This is because the compression load between the pelvis and lumbar spine resulting from vertical impacts is certifiable for the Hybrid II ATD, not the Hybrid III.

The Federal Aviation Administration (FAA) Hybrid III may also be used for certification purposes; however it is currently not available in MSC Dytran. Although the Hybrid III ATD may not be certifiable according to FAR 23.562 subpart C, the technique required to implement the various ATDs within MSC Dytran remains the same.

An Eulerian-based finite element technique was implemented for soft soil impact analyses, and its effectiveness was determined through correlation of experimental penetrometer drop test results published by Fasanella et al. [59]. Based on the results obtained it was concluded that an Eulerian-based approach to soft soil impact analysis, for crashworthiness applications, is valid. Greater model fidelity may possibly be gained by further investigation of the drop test methodology, viscosity effects, variation of soil mechanical properties through the depth range, and strain rate effects.

An investigation into the performance of the Tsai-Wu failure criterion to capture the onset and progression of failure through the layers of fibre reinforced composite laminates was conducted for an impulsively loaded unidirectional laminate strip model. Investigation of the stress and failure time-history plots revealed that the Tsai-Wu failure criterion successfully captured the onset and progression of failure through the laminate layers. In general, the Tsai-Wu failure criterion accurately predicts the deformation of laminates at low strains, as is expected for fibre-dominated laminates. Laminate deformation was therefore assumed to be reasonably accurate as only fibre-dominated layups were used throughout this study. It became apparent during this study that the Tsai-Wu failure criterion over-predicts the strength of laminates for biaxial compression-compression loading. During impact, a change in aircraft pitch produces bending moments in the fuselage, which result in compressive or tensile stresses along the length of the fuselage (in addition to fuselage compressive stresses due to longitudinal impact forces). It was therefore assumed that the applied stresses are uniaxial (along the length of the fuselage) and a biaxial compression-

compression loading condition may be ignored. This assumption was also deemed applicable for the impulsively loaded unidirectional composite laminate strip model, thus the loading condition for the unidirectional laminate strip model was deemed representative of the expected loading conditions for the fuselage of the aircraft. Based on the results obtained and in conjunction with the abovementioned assumptions, the implementation of the Tsai-Wu failure criterion for composite aircraft crashworthiness applications is deemed valid. Note that the Tsai-Wu failure criterion predicts the onset of failure, but does not explicitly identify the failure mode. Strain rate effects were not considered.

Impacts into rigid and soft soil terrains with varying aircraft impact and pitch angles were investigated, revealing different responses. Impacts into soft terrains typically produce high aircraft decelerations in the longitudinal direction and stop the aircraft abruptly due to digging in of the aircraft into the soft terrain, whereas impacts into hard / rigid terrains typically produce high aircraft decelerations in the vertical direction. All scenarios successfully reached the set analysis end time of 0.18 seconds without the occurrence of numerical instabilities or error. The results obtained from the crash analyses provide an indication of the forces transmitted to the occupant through the seat and restraint system, and the aircraft's ability to provide a survivable volume throughout the crash event.

Typical limitations encountered in previously published works were overcome with the techniques presented in this study. The aircrafts' laminate layup schedule was explicitly defined in MSC Dytran, thereby eliminating the inherent inaccuracies of using isotropic models to approximate laminated composite materials. The aircraft was assigned both horizontal and vertical velocity components instead of only a vertical component, which increased the model accuracy. Numerical instabilities, due to element distortion of the terrain when using a Lagrangian approach, were eliminated with the use of an Eulerian soft soil model (Eulerian techniques are typically used to model

fluids where large deformations occur, which is a characteristic of crash analyses). Structural failure was successfully implemented by coupling Lagrangian and Eulerian solvers. The ATB model allowed for the real-time interactions between the occupant and aircraft to be investigated, unlike previously where analyses of the occupant were performed in separate local models using accelerations derived from the global analyses results.

It is acknowledged that there are aspects of this study that may require future work. For example, the level of detail may be increased in the analysis models for the wings, stabilisers and longitudinal skin stiffeners. Representation of the foam model for the aircraft seat may be validated. Model fidelity of the penetrometer drop tests into soft soil may be improved by investigation of the drop test methodology, viscosity effects, variation of soil mechanical properties through the depth range, and strain rate effects. Additionally, experiments may be required to determine accurate inputs for the soft soil model, such as for the cohesive friction parameter and spallation pressure. The reason for sudden increases in internal energy of the Euler material (i.e. soft soil) may require further investigation. Further validation of the composite material model may be performed by comparing experimental and numerical results of various strength tests. Investigation of strain rate effects on composite materials may be performed to increase model accuracy. The introduction of a deformable occupant may be useful in determining damage to biological tissue. Crashworthiness concepts may be introduced into the design of the aircraft structure based on the results obtained, and the effectiveness of these concepts may be investigated with the analysis methodology presented in this study. Examples of crashworthiness concepts include the use of a non-scoop fire wall and an energy absorbing subfloor structure. A non-scoop fire wall would be designed to pitch positively out of a crater created by a nose-down impact into soft terrain, thereby increasing the stopping time and reducing longitudinal decelerations. An energy absorbing subfloor structure would be designed to decrease the vertical decelerations transferred to the occupants.

As can be seen above, there are many aspects of this study that may require future work; however the primary aim for this study was successfully satisfied.

## REFERENCES


[1] J. W. Coltman, C. Van Ingen, N. B. Johnson, and R. E. Zimmerman, "Aircraft crash survival design guide volume II - Aircraft design crash impact conditions and human tolerance," DTIC, Rep. AD-A218 435, Dec. 1989.

[2] A. E. Stockwell, "Simulation of an impact test of the all-composite Lear Fan aircraft," NASA Langley Research Center, Hampton, VA, Rep. NASA/CR-2002-211458, Oct. 2002.

[3] M. Mališ and J. Šplíchal, "The sailplane cockpit structure during emergency landing condition," in *25th International Congress of the Aeronautical Sciences*, Hamburg, Germany, 2006.

[4] M. Bossak and J. Kaczkowski, "Global/local analysis of composite light aircraft crash landing," *Computers & Structures,* vol. 81, pp. 503-514, 2003.

[5] C. W. Clarke and Y. Shen, "The development of a rotorcraft water-impact analysis methodology," in *AHS/SAFE Crashworthiness Specialists' Meeting on Crash Safety Challenges and Innovative Solutions*, Phoenix, AZ, USA, 1998, pp. 23-27.

[6] G. Wittlin, M. Smith, A. Sareen, and M. Richards, "Airframe water impact analysis using a combined MSC/Dytran-DRI/KRASH approach," in *American Helicopter Society 53rd Annual Forum*, Virginia Beach, Virginia, 1997, pp. 1138-1150.

[7] E. L. Fasanella, K. E. Jackson, C. E. Sparks, and A. K. Sareen, "Water impact test and simulation of a composite energy absorbing

fuselage section," in *American Helicopter Society 59th Annual Forum*, Phoenix, AZ, USA, 2003.

[8] I. M. Daniel and O. Ishai, *Engineering mechanics of composite materials*. New York: Oxford University Press, 1994.

[9] L. P. Kollar and G. S. Springer, *Mechanics of composite structures*. New York: Cambridge University Press, 2003.

[10] F. C. Campbell, *Structural composite materials*. Russel Township, OH: ASM International, 2010.

[11] C. T. Herakovich, *Mechanics of fibrous composites*. New York: John Wiley & Sons, 1998.

[12] C. Kassapoglou, *Design and analysis of composite structures with applications to aerospace structures*, 2nd ed. Chichester, UK: John Wiley & Sons, 2013.

[13] *ASM handbook vol. 21 - composites*, ASM International, 2001.

[14] R. Khandan, S. Noroozi, P. Sewell, and J. Vinney, "The development of laminated composite plate theories: a review," *Journal of Materials Science,* vol. 47, pp. 5901-5910, 2012.

[15] H.-T. Thai and D.-H. Choi, "A simple first-order shear deformation theory for laminated composite plates," *Composite Structures,* vol. 106, pp. 754-763, 2013.

[16] S.-E. Kim, H.-T. Thai, and J. Lee, "A two variable refined plate theory for laminated composite plates," *Composite Structures,* vol. 89, pp. 197-205, 2009.

[17] W. Hufenbach, R. Gottwald, B. Grüber, M. Lepper, and B. Zhou, "Stress concentration analysis of thick-walled laminate composites with a loaded circular cut-out by using a first-order shear deformation theory," *Composites Science and Technology,* vol. 68, pp. 2238-2244, 2008.

[18] T.-K. Nguyen, K. Sab, and G. Bonnet, "First-order shear deformation plate models for functionally graded materials," *Composite Structures,* vol. 83, pp. 25-36, 2008.

[19] J. N. Reddy, *Mechanics of laminated composite plates and shells: theory and analysis*, 2nd ed. Boca Raton, FL: CRC press, 2004.

[20] S. W. Key and C. C. Hoff, "An improved constant membrane and bending stress shell element for explicit transient dynamics," *Computer Methods in Applied Mechanics and Engineering,* vol. 124, pp. 33-47, 1995.

[21] M. Walker and R. E. Smith, "A technique for the multiobjective optimisation of laminated composite structures using genetic algorithms and finite element analysis," *Composite Structures,* vol. 62, pp. 123-128, 2003.

[22] Y. Y. Wang, K. Y. Lam, and G. R. Liu, "Bending analysis of classical symmetric laminated composite plates by the strip element method," *Mechanics of Composite Materials and Structures,* vol. 7, pp. 225-247, 2000.

[23] M. J. Hinton, A. S. Kaddour, and P. D. Soden, "A comparison of the predictive capabilities of current failure theories for composite laminates, judged against experimental evidence," *Composites Science and Technology,* vol. 62, pp. 1725-1797, 2002.

[24] K.-S. Liu and S. W. Tsai, "A progressive quadratic failure criterion for a laminate," *Composites Science and Technology,* vol. 58, pp. 1023-1032, 1998.

[25] V. Las, R. Zemcík, T. Kroupa, and R. Kottner, "Failure prediction of composite materials," *Bulletin of Applied Mechanics,* vol. 4, pp. 81-87, 2008.

[26] A. Puck and H. Schürmann, "Failure analysis of FRP laminates by means of physically based phenomenological models," *Composites Science and Technology,* vol. 58, pp. 1045-1067, 1998.

[27] K. Huebner, T. G. Byrom, and E. A. Thornton, *The finite element method for engineers*, 3rd ed. New York: Wiley, 1995.

[28] C. S. Desai and T. Kundu, *Introductory finite element method*. Boca Raton, FL: CRC Press, 2001.

[29] J. N. Reddy, *An introduction to nonlinear finite element analysis*. Oxford, England: Oxford University Press, 2004.

[30] S. S. Rao, *The finite element method in engineering*, 3rd ed. Boston, MA: Butterworth-Heinemann, 1999.

[31] S. R. Wu and L. Gu, *Introduction to the explicit finite element method for nonlinear transient dynamics*. Hoboken, NJ: John Wiley & Sons, 2012.

[32] D. S. Burnett, *Finite element analysis: from concepts to applications*. Reading, MA: Addison-Wesley, 1987.

[33] J. N. Reddy, *An introduction to the finite element method*, 2nd ed. New York: McGraw-Hill, 1993.

[34] *MSC/Dytran theory manual*, MSC Software Corporation, Santa Ana, CA, USA, 2012.

[35] T. Belytschko, J. I. Lin, and C.-S. Tsay, "Explicit algorithms for the nonlinear dynamics of shells," *Computer Methods in Applied Mechanics and Engineering,* vol. 42, pp. 225-251, 1984.

[36] *LS-DYNA theory manual*, Livermore software technology corporation, Livermore, CA, 2006.

[37] D. P. Flanagan and T. Belytschko, "A uniform strain hexahedron and quadrilateral with orthogonal hourglass control," *International Journal for Numerical Methods in Engineering,* vol. 17, pp. 679-706, 1981.

[38] E. Stein, R. de Borst, and T. J. R. Hughes, *Encyclopedia of computational mechanics*. UK: John Wiley, 2004.

[39] *MSC/Dytran user's guide*, MSC Software Corporation, Santa Ana, CA, USA, 2012.

[40] N. K. Birnbaum, N. J. Francis, and B. I. Gerber, "Coupled techniques for the simulation of fluid-structure and impact problems," *Computer Assisted Mechanics and Engineering Sciences,* vol. 6, pp. 295-311, 1999.

[41] E. L. Fasanella and K. E. Jackson, "Best practices for crash modeling and simulation," NASA Langley Research Center, Hampton, VA, USA, Rep. NASA/TM-2002-211944, Oct. 2002.

[42] T. R. Hurley and J. M. Vandenburg, "Small airplane crashworthiness design guide," AGATE, Rep. AGATE-WP3.4-034043-036, Apr. 2002.

[43] H. J. Mertz, "Anthropomorphic test devices," in *Accidental Injury: Biomechanics and Prevention*, A. M. Nahum and J. W. Melvin, Eds., 1 ed New York: Springer, 1993, pp. 66-84.

[44] J. A. Pellettiere, D. Moorcroft, and G. Olivares, "Anthropomorphic test dummy lumbar load variation," in *22nd Enhanced Safety of Vehicles Conference*, Washington, DC 2011.

[45] M. Polanco and J. D. Littell, "Vertical drop testing and simulation of anthropomorphic test devices," in *American Helicopter Society 67th Annual Forum*, Virginia Beach, VA, 2011.

[46] "Anthropomorphic dummies for crash and escape system testing," AGARD, Neuilly-Sur-Seine, France, Rep. AGARD-AR-330, Jul. 1996.

[47] D. F. Shanahan, "Human tolerance and crash survivability," in *Pathological Aspects and Associated Biodynamics in Aircraft Accident Investigation*, Madrid, Spain, 2004.

[48] *Airworthiness Standards: Normal, Utility, Acrobattic, and Commuter Category Airplanes*, FAR Part 23, 1991.

[49] H. W. Henn, "Crash tests and the head injury criterion," *Teaching Mathematics and its Applications,* vol. 17, pp. 162-170, 1998.

[50] J. W. Coltman and S. M. Arndt, "The naval aircraft crash environment: aircrew survivability and aircraft structural response," DTIC, Rep. AD-A204 825, Sep. 1988.

[51] A. K. Sareen, E. Fasanella, C. Sparks, K. Jackson, and B. R. Mullins Jr, "Comparison of hard surface and soft soil impact performance of a crashworthy composite fuselage concept," in *American Helicopter Society 58th Annual Forum*, Montreal, Canada, 2002, pp. 1973-1983.

[52] J. E. Terry, S. J. Hooper, and M. Nicholson, "Design and test of an improved crashworthiness small composite airframe," NASA Langley Research Center, Hampton, VA, Rep. NASA/CR-2002-211774, Aug. 2002.

[53] H. Cheng, A. L. Rizer, and L. A. Obergefell, "Articulated total body model version V user's manual," United States Air Force Research Laboratory, Wright-Patterson AFB, OH, USA, Rep. AFRL-HE-WP-TR-1998-0015, Feb. 1998.

[54] *MSC/Dytran reference manual*, MSC Software Corporation, Santa Ana, CA, USA, 2012.

[55] *MSC/Dytran example problem manual*, MSC Software Corporation, Santa Ana, CA, USA, 2012.

[56] S. W. Gong, H. P. Lee, and C. Lu, "Computational simulation of the human head response to non-contact impact," *Computers & Structures,* vol. 86, pp. 758-770, 2008.

[57] T.-L. Teng, F.-A. Chang, Y.-S. Liu, and C.-P. Peng, "Analysis of dynamic response of vehicle occupant in frontal crash using multibody dynamics method," *Mathematical and Computer Modelling,* vol. 48, pp. 1724-1736, 2008.

[58] E. L. Fasanella and K. E. Jackson, "Impact testing and simulation of a crashworthy composite fuselage section with energy-absorbing seats and dummies," NASA Langley Research Center, Hampton, VA, Rep. NASA/TM-2002-211731, Jun. 2002.

[59] E. L. Fasanella, Y. Jones, N. F. Knight Jr, and S. Kellas, "Low velocity earth-penetration test and analysis," in *42nd*

*AIAA/ASME/ASCE/AHS/ASC Structures, Structural Dynamics, and Materials Conference and Exhibit*, Seattle, WA, 2001, pp. 1494-1503.

[60] M. Nazem, J. P. Carter, D. W. Airey, and S. H. Chow, "Dynamic analysis of a smooth penetrometer free-falling into uniform clay," *Géotechnique,* vol. 62, pp. 893-905, 2012.

[61] A. S. Seetamsetti, "Comparison of finite element analysis of impact on water and soil using Lagrangian, ALE, and SPH approaches and airframe impact applications," M.S. thesis, Dept. Mech. Eng., Wichita State Univ., Wichita, KS, 2012.

[62] D. Wulfsohn, B. A. Adams, and D. G. Fredlund, "Triaxial testing of unsaturated agricultural soils," *Journal of Agricultural Engineering Research,* vol. 69, pp. 317-330, 1998.

[63] R. F. Craig, *Soil mechanics*, 6th ed. London, England: E & FN Spon, 1997.

[64] J. F. Labuz and A. Zang, "Mohr–Coulomb failure criterion," *Rock Mechanics and Rock Engineering,* vol. 45, pp. 975-979, 2012.

[65] S. van Asselen, E. Stouthamer, and T. h. W. J. van Asch, "Effects of peat compaction on delta evolution: a review on processes, responses, measuring and modeling," *Earth-Science Reviews,* vol. 92, pp. 35-51, 2009.

[66] R. G. Budynas, *Advanced strength and applied stress analysis*, 2nd ed. Boston, MA: McGraw-Hill, 1999.

[67] E. L. Fasanella, K. E. Jackson, K. H. Lyle, C. E. Sparks, and A. K. Sareen, "Multi-terrain impact testing and simulation of a composite

energy absorbing fuselage section," in *American Helicopter Society 60th Annual Forum*, Baltimore, MD, 2004.

[68] P. D. Soden, A. S. Kaddour, and M. J. Hinton, "Recommendations for designers and researchers resulting from the world-wide failure exercise," *Composites Science and Technology,* vol. 64, pp. 589-604, 2004.

[69] P. D. Soden, M. J. Hinton, and A. S. Kaddour, "Lamina properties, lay-up configurations and loading conditions for a range of fibre-reinforced composite laminates," *Composites Science and Technology,* vol. 58, pp. 1011-1022, 1998.

[70] S. Hooper, M. Henderson, and W. Seneviratne, "Design and construction of a crashworthy composite airframe," AGATE, Rep. AGATE-WP3.4-034026-089 Rev. A, Mar. 2002.

[71] J. Zhang, N. Kikuchi, V. Li, A. Yee, and G. Nusholtz, "Constitutive modeling of polymeric foam material subjected to dynamic crash loading," *International Journal of Impact Engineering,* vol. 21, pp. 369-386, 1998.

[72] M. Landervik and R. Larsson, "Modeling of large inelastic deformations of foams with respect to the point of compaction," *European Journal of Mechanics A/Solids,* vol. 27, pp. 234-246, 2008.

[73] S. Basu, "Quasi-static and dynamic compression behavior of flexible cellular material," Agilent Technologies, 2012.

[74] B. Croop and H. Lobo, "Selecting material models for the simulation of foams in LS-DYNA," in *7th European LS-DYNA Conference*, Salzburg, Austria, 2009.

[75] *MSC/Nastran dynamic analysis user's guide*, MSC Software Corporation, Santa Ana, CA, USA, 2011.

[76] L. Liao, "A study of inertia relief analysis," in *52nd AIAA/ASME/ASCE/AHS/ASC Structures, Structural Dynamics and Materials Conference*, Denver, CO, 2011.

[77] *MSC/Nastran linear static analysis user's guide*, MSC Software Corporation, Santa Ana, CA, USA, 2011.

# APPENDIX A: LOW-PASS DIGITAL BUTTERWORTH FILTER AND FAST FOURIER TRANSFORM DETAILS

High frequency noise is typically associated with crash analysis time-history plots. An example of a possible cause of high frequency noise in numerical analyses may be due to the contact algorithm where forces are continuously applied to separate the contact surfaces. In order to decrease the high frequency noise, a low-pass Butterworth digital filter with zero-phase distortion in Matlab was used to process time-history data where stated. Typical Matlab code for this filter is shown in Figure 124. The fast Fourier transform in Matlab was used to determine the cut-off frequency for the low-pass Butterworth digital filter. Typical Matlab code for the fast Fourier transform is shown in Figure 125.

```
%Create vectors by copying and pasting data
Time=[PASTE DATA HERE];
DATA=[PASTE DATA HERE];
X=DATA;

%Filter order
N=2;
%Filter cut-off frequency (normalised)
Wn=0.3;

%Low-pass Butterworth digital filter
[B,A]=BUTTER(N,Wn,'low');
%Zero-phase forward & reverse digital filtering
Y=FILTFILT(B,A,X);
%Plot data (original and filtered)
plot(Time,Y,Time,X),grid on;
set(gca,'FontSize',16);
xlim ([min(Time) max(Time)]);
xlabel('Time (s)','fontsize',16);
ylabel('DATA','fontsize',16);
%legend('original data','filtered data',1)
```

**Figure 124: Typical low-pass Butterworth digital filter code in Matlab with zero-phase distortion**

```
%Create vector by copy and pasting data
DATA=[PASTE DATA HERE];

%Sampling frequency (samples per second)
Fs=100000;
%Sample time (time increment per sample)
T=1/Fs;
%Length of signal (number of samples)
L=3500;
%Time vector (time range for data)
t=(0:L-1)*T;
%FFT length
n=2^nextpow2(L);
%Discrete Fourier transform
y=fft(DATA,n);
%Frequency range
f=(0:n-1)*(Fs/n);
power=y.*conj(y)/n;

%Rearrange y values
y0=fftshift(y);
%Zero-centered frequency range
f0=(-n/2:n/2-1)*(Fs/n);
%Zero-centered power
power0=y0.*conj(y0)/n;
%Plot zero-centered data
plot(f0,power0),grid on;
set(gca,'FontSize',16);
xlabel ('Frequency (Hz)','fontsize',16);
ylabel('Power','fontsize',16);
```

**Figure 125: Typical fast Fourier transform code in Matlab**